UC Berkeley
UC Berkeley Electronic Theses and Dissertations

Title
Instability of Internal Gravity Waves from Wave-wave/topography Interactions

Permalink
https://escholarship.org/uc/item/0ms2x2f2

Author
Liang, Yong

Publication Date
2018

Peer reviewed|Thesis/dissertation

eScholarship.org Powered by the California Digital Library
University of California

Instability of Internal Gravity Waves from Wave-wave/topography Interactions

by

Yong Liang

A dissertation submitted in partial satisfaction of the

requirements for the degree of

Doctor of Philosophy

in

Applied Science and Technology

in the

Graduate Division

of the

University of California, Berkeley

Committee in charge:

Professor M.-Reza Alam, Chair
Professor Tarek I. Zohdi
Professor Simo Mäkiharju

Fall 2018

Abstract

Instability of Internal Gravity Waves from Wave-wave/topography Interactions

by

Yong Liang

Doctor of Philosophy in Applied Science and Technology

University of California, Berkeley

Professor M.-Reza Alam, Chair

It is well-known that internal wave breaking is the principle cause of ocean mixing. The latter plays a role in shaping global climate and ocean ecology. To understand how internal wave loses instability and possibly breaks, in this thesis I present some new findings on the instability mechanisms of internal gravity waves due to wave-wave/topography interactions.

Parametric Subharmonic Instability (PSI) is one of the most important mechanisms that transfer energy from tidally-generated long internal waves to short steep waves. Breaking of these short waves results in diapycnal mixing through which oceanic abyssal stratification is maintained. It has long been believed that PSI is strongest between a primary internal wave and perturbative waves of half the frequency of the primary wave. Here, I rigorously show that this is not the case. Specifically, I show that neither the initial growth rate nor the maximum long-term amplification occur at the half frequency, and demonstrate that the dominant subharmonic waves have much longer wavelengths than previously thought.

Next I show that there exist internal gravity waves that are inherently unstable, that is, they cannot exist in nature for a long time. The instability mechanism is a one-way (irreversible) harmonic-generation resonance that permanently transfers the energy of an internal wave to its higher harmonics. I show that, in fact, there are a countably infinite number of such unstable waves. For the harmonic-generation resonance to take place, the nonlinear terms in the free surface boundary condition play a pivotal role, and the instability does not occur in a linearly-stratified fluid if a simplified boundary condition such as a rigid lid or a linearized boundary condition is employed. Harmonic-generation resonance presented here provides a mechanism for the transfer of internal wave energy to the higher-frequency part of the spectrum hence affecting, potentially significantly, the evolution of the internal waves spectrum.

Following the work on harmonic generations of internal waves, we show that monochromatic internal gravity waves in a stratified ocean can continuously descend to smaller scales of higher wave numbers after being reflected from no-penetration boundaries, provided their

second harmonics satisfy dispersion relation. The wave with wave number k and frequency ω first generate its second harmonic due to the non-linearity in the momentum equation and the free surface boundary. Then the resonant interaction of the parent wave with its second harmonic gives rise to a $(3k, \omega)$ wave upon reflection, starting from which a series of triad resonances continuously form in the vicinity of the frequency ω or 2ω. The energy of the internal wave is sent to waves with higher and higher wave numbers. The mechanism potentially explains how part of internal wave energy converts from large scales to that of turbulent mixing near reflecting boundaries, such as ocean ridges and steep continental slopes.

Internal waves mainly arise from wind disturbing the upper ocean mixed layer and barotropic tide flowing over topographic features in the ocean. I report a mechanism for conversion of tidal energy to internal gravity waves, through baratropic tidal currents interacting with ambient internal waves. The newly-generated internal waves have the same wave length as the ambient waves and frequencies higher by the tidal frequency. I show that they grow exponentially in time and continuously extract energy from the tidal currents. The mechanism exists in any stratified ocean with smooth density profiles and is only possible if a nonlinear free surface is taken into account. I show that for a typical water depth of 4000 m and density stratification 5% in the Pacific Ocean, the energy flux from baratropic tide to plane internal waves via this mechanism can reach order of $1\mathrm{MWm}^{-1}$. It therefore can be significant enough to account for a fraction of the 1TW total tidal energy loss in the open deep ocean.

Ocean mixing has been seen increased where there is rough bottom topography in the ocean. I show in theory that, in a two dimensional domain, with a free surface taken into account, the interaction between an internal wave and corrugated bottom topography can efficiently generate a series of co-directional internal waves with higher wave numbers. As a result, the internal wave energy can be transferred to smaller scales where internal wave is more prone to breaking and being dissipated.

Contents

Contents i

List of Figures iii

1 Introduction 1

2 Dominant Resonance in Parametric Subharmonic Instability of Internal Waves 4
2.1 Interaction Equations for Parametric Subharmonic Instability 6
2.2 Nonlinear Stability Analysis 11
2.3 Parametric Subharmonic Instability of A Mode-1 M2 Internal Tide 13
2.4 Conclusion 16

3 Inherently Unstable Internal Gravity Waves due to Resonant Harmonic Generation 18
3.1 Governing Equations and Dispersion Relation 18
3.2 Harmonic Generation 21
3.3 Results and Discussions 22
3.4 Conclusion 31
Appendices 31
3.A Derivation of the Interaction Equation 31
3.B Proof of the Sign of α/β 37

4 Energy Cascade of A Monochromatic Internal Gravity Wave from Vertical Reflecting Boundaries 39
4.1 Governing Equations 40
4.2 Roughly Equal-spaced Horizontal Wave Numbers at Fixed Frequencies . . . 41
4.3 Resonance Mechanism 42
4.4 Derivation of Interaction Equation 43
4.5 Results 47
4.6 Conclusion 49

5 Internal Waves Generation from Barotropic Tide Interacting with Ambient Waves 50
5.1 Interaction Equations 51

5.2 Analytical Results 56
5.3 Conclusion 59

6 Cascading of Internal Waves Energy to Large Wavenumbers by Seabed Corrugations 60
6.1 Governing Equations 61
6.2 Perturbation Analysis 63
6.3 Results and Discussions 66
6.4 Conclusion 69

Bibliography 70

List of Figures

2.1 (a) Geometric construction of several of possible triad resonances (c.f. (2.1)) between a primary internal wave of ω=0.8 (red circle) and pairs of lower harmonic waves for ah=0.05. Square and triangles correspond to the higher mode propagating respectively in the same/opposite direction of the primary wave, and diamonds show a special case in which both subharmonic waves travel in the same direction. Six triads are highlighted by color solid lines. Black dashed lines show branches of the dispersion relation $\omega = |k/\sqrt{k^2+m^2}|$. (b) Variation of the normalized exponent (σ/σ_{max}) of linear stability analysis (2.7) as a function of normalized frequency ω/ω_0. Clearly subharmonic waves with frequencies close to $\omega/2$ have the highest exponents (c.f. figure 11b of Bourget et al., 2013). (c) Normalized interaction coefficient $|s_i/s_{max}|$ as a function of normalized frequency ω/ω_0. The maximum initial growth rate occurs at the frequency ω/ω_0=0.83 although σ is maximum at ω/ω_0=0.5. 8

2.2 Evolution of amplitudes of (a) the primary internal wave and (b) the six subharmonic pairs undergoing PSI corresponding to the case represented in figure 2.1. Initial amplitudes of perturbation waves chosen as $A_{i1/i2}|_{t=0}$=0.001 and up to mode 20th (which results in 38 PSI pairs) are considered in the numerical integration of (2.9). All waves undergo a modulation in time, and the maximum growth is obtained for perturbation wave of ω/ω_0=0.76. 10

2.3 Time-evolution of a primary internal wave of frequency $\omega = 0.8$ with two perturbation waves of frequencies $\omega_{1,2}/\omega_0$=0.24,0.76. Direct simulations results of MITgcm (blue solid line) matches well with our analytical results using nonlinear stability theory though numerical integration of (2.9) (red dashed line). For comparison, growth rate prediction by linear stability theory (black dash-dotted line) are also shown. Physical parameters for MITgcm simulations are $a = 5\times10^{-5}\mathrm{m}^{-1}$, $h = 1000$m and initial amplitude is 1m for the primary wave and 0.01m for each of the two subharmonic waves. 12

2.4 Possible subharmonic waves from the parametric subharmonic instability of a mode-1 M2 internal tide (primary wave) for oceans where Brunt-Väisälä frequency $N = 10^{-3}\mathrm{s}^{-1}$. Square and triangles correspond to the higher mode propagating respectively in the same/opposite direction of the primary wave, and diamonds show a case in which both subharmonic waves travel in the same direction. Black dashed lines show branches of the dispersion relation $m^2 = k^2(N^2-\omega^2)/(\omega^2-f^2)$. 15

2.5 Evolution of amplitudes of (a) the mode-1 M2 internal tide and (b) the largest five subharmonic waves. Up to mode 20th are considered in the numerical integration of (2.9). The maximum growth is obtained for the subharmonic wave at ω/ω_0=0.566 and 0.434. 16

3.1 Plot of the dimensionless frequency ω/N as a function of dimensionless wavenumber kh of free internal waves (i.e. $\mathscr{D}(k,\omega)=0$) in a fluid of linearly stratified density $\rho(z)=\rho_0(1-az)$, with $ah = 0.05$. Associated with each wavenumber there is one surface wave and an infinite number of internal wave modes (blue solid-line branches). The frequency of internal waves cannot exceed the Brunt-Väisälä frequency N, and all branches of the dispersion relation curve are capped at ω/N=1. We also plot contours of $\mathscr{D}(2k,2\omega)$=0 (red dash-dotted lines) whose intersections with blue lines (shown by red circles) mark waves whose second harmonics are also solutions to the dispersion relation. These second harmonics are at the intersections of contours of $\mathscr{D}(k/2,\omega/2)$=0 (green dashed lines) and $\mathscr{D}(k,\omega)$=0 and are marked by black squares. The second harmonic of the wave at "a" (mode 2), is the wave "A" (mode 1) and so on. 20

3.2 There are countably infinite number of internal waves that are unstable to their second harmonic. Physically this means that specific incident internal waves of wavenumber and frequency (k,ω) will give up their energy permanently (in a one-way irreversible process, c.f. equation (3.5)) to their second harmonic $(2k,2\omega)$. The necessary condition for this to happen is $\mathscr{D}(k,\omega)=\mathscr{D}(2k,2\omega)$=0. These waves, for the parameters of figure 3.1, are shown here by red squares. Similar story holds for another set of waves that are unstable to their third harmonic (blue circles, necessary condition $\mathscr{D}(k,\omega)=\mathscr{D}(3k,3\omega)$=0), and fourth harmonic (green triangles, $\mathscr{D}(k,\omega)=\mathscr{D}(4k,4\omega)$=0) and so on. 22

3.3 Spatial evolution of the amplitude of the original wave (blue dashed line) and its resonant second harmonic (red solid line) corresponding to the point "a" in figure 3.1 (kh=3.144772, ω/N=0.4472136, aA_{10}/N=0.0023, fig. a), and the point "c" in figure 3.1 (kh=5.132426, ω/N=0.4780914, aA_{10}/N=0.0023, fig. b). In figure (a) energy goes from mode 2 to mode 1, whereas in figure (b) energy goes from mode 3 to mode 1. Figure (c) shows the energy flux of each wave as well as the sum of the energy fluxes (green dash-dotted line) in case (b). As expected from energy conservation, the overall energy flux is unchanged in the domain of interaction. 25

3.4 Comparison of analytical results (3.5) with the direct simulation. The physical parameters used are: density gradient $a = 1 \times 10^{-3}\ m^{-1}$, water depth $h = 100$m, dimensionless wave number kh=3.147946, dimensionless frequency ω/N=0.4472136, the amplitude of vertical velocity of the incident wave A_{10}=0.1 m/s. 26

3.5 Time evolution of the vertical velocities of internal gravity waves that satisfy the conditions of harmonic generation. The physical parameters used here correspond to figure 3.3a. (a) Time evolution of the amplitudes of the two waves. T_0 is the period of the parent wave. (b) Snapshots of the wave field at $t = 0$ (b1), $t = 500T_0$ (b2), and $1500T_0$(b3). The presented mechanism initially results in a modulation of the primary wave, and eventually all the energy goes to the second harmonic. 28

3.6 Dependence of the decay rate $R = \sqrt{-\alpha_t \beta_t}$ on mode numbers n and the horizontal wave numbers. We normalize the quantities by the wave where the largest decay rate is obtained (here it corresponds to point "a" in figure 3.1). Color scale represents R/R_0 where $R_0 = 3.81 \times 10^{-6}\mathrm{m}^{-1}$. The physical parameters used here are the same as in figure 3.1. 29

3.7 Plots of $\mathscr{D}(k,\omega) = 0$, $\mathscr{D}(2k,2\omega) = 0$ and $\mathscr{D}(k/2,\omega/2) = 0$ for parabolic and exponential density profiles (c.f. figure 3.1): (a) for $\rho(z) = \rho_0(1+az^2)$ with $a = 1 \times 10^{-5}\mathrm{m}^{-2}$ and (b) for $\rho(z) = \rho_0[1+\delta-\delta\exp(az)]$ with $a = 0.1\mathrm{m}^{-1}$ and $\delta = 0.1$. On the right-side of each plot, we show the normalized density profile $\rho(z)/\rho_0$ and the Brunt-Väisälä frequency $N(z)^2$ of the two nonlinear density profiles (blue solid lines) overlaid of top of corresponding plots of linear density profile (red dashed lines). Water depth is $h = 100$m. 30

4.1 Difference of two consecutive horizontal wave numbers at a fixed frequency v.s. mode number i for linear, parabolic and exponential density profiles. In the vertical axis $\Delta k_i = k_{i+1} - k_i$. It is normalized by Δk_n which is the difference of the last two wave numbers (since Δk converges to a constant as n increases). The normalized frequency is 0.35 by $\sqrt{ga}$, $\sqrt{2gah}$ and $\sqrt{ga\delta}$ respectively. The linear profile is $\rho(z) = \rho_0(1+az)$ with $a = 5 \times 10^{-4}\mathrm{m}^{-1}$, the parabolic one is $\rho(z) = \rho_0(1+az^2)$ with $a = 1 \times 10^{-5}\mathrm{m}^{-2}$, and the exponential one is $\rho(z) = \rho_0[1+\delta-\delta\exp(az)]$ with $a = 0.1\mathrm{m}^{-1}$ and $\delta = 0.1$. Water depth is $h = 100$ m for all the three cases. The legend is $\rho(z)/\rho_0$. 41

4.1 Representation of energy flow from small wavenumbers to higher ones after the monochromatic internal wave in discussion is reflected. The three waves associated with the arrow lines in the same color form one resonant triad. The second harmonic generation involves two wave (i.e., one arrow line). Here we only show energy flow to internal waves propagating to one direction (towards or away) on account of symmetry. The lighter dash lines show the dispersion relation of internal gravity waves $\mathscr{D}(k,\omega) = 0$. The intersecting heavier blue dash line and the red one are to illustrate how to find a wave that satisfy $\mathscr{D}(k,\omega) = 0$ and $\mathscr{D}(2k,2\omega) = 0$ simultaneously. 43

4.1 Time evolutions of a series of internal waves generated from a single monochromatic internal wave propagating to a vertical no-penetration boundary. The initial amplitudes of the $(2,2,1)$ waves is 1m for both the right-propagating and left-propagating waves, i.e., $A_0(0) = B_0(0) = 1\text{m}$. Totally $N = 53$ waves are taken into account, of which the largest 14 waves are presented. The three numbers associated with each wave in a parenthesis are normalized wave number, frequency and vertical mode number, for example, $(2,2,1)$ stands for a wave of wave number $2k$, frequency 2ω and mode 1, where $k = 0.0314\text{m}^{-1}$, $\omega = 0.0313\text{s}^{-1}$ in this case. $a = 5\times10^{-4}\text{m}^{-1}$,$H = 100\text{m}$. 48

4.2 The wave field at $t = 0$ and at a later time point $t = 2\times10^3 T_0$, represented by the vertical velocity. $T_0 = 2\pi/\omega$, $\lambda_0 = 2\pi/k$, $H = 100\text{m}$. 48

5.1 Wave solutions (k,ω_1) in the first 10 vertical modes that satisfy $\mathscr{D}(k,\omega_1) = 0$ and $\mathscr{D}(k,\omega_1+\sigma) = 0$ (i.e., $\mathscr{D}(k,\omega_2) = 0$) obtained by extracting the intersections of the two curves, considering two latitudes (a): $f = 3.76\times10^{-5}\text{s}^{-1}$ (the latitude is $15°N$); (b): $f = 1.03\times10^{-4}\text{s}^{-1}$ (the latitude is $45°N$). The physical parameters used here are $a = 5\times10^{-6}\text{m}^{-1}$, $h = 4000\text{m}$, $\sigma = 1.45\times10^{-4}\text{s}^{-1}$ (corresponding to the frequency of a M2 tidal current). Note that k here is the modulus of the horizontal wave vector $\mathbf{k}$, so one point in the figure represents a series of waves that satisfy $k_x^2 + k_y^2 = k^2$. 54

5.1 (a), (c): Time evolutions of the ambient wave and the new wave for a selected point (circled) in (b) and (d), from $t = 0$ to $t = 150$. For the ambient wave, $kh = 0.084$, $\omega/N = 0.013$. (b), (d): Wave amplitudes of all admissible waves up to $kh = 0.1$ at $t = 150$, the waves presented here correspond to those in 5.1(a) at latitude $15°N$. Color scale represents the moduli of $A_1(t)$ and $A_2(t)$. $\sigma/f = 7.98$, $ah = 5\times10^{-2}$, $f/N = 0.0016$, $\delta_1 = 0.5$, $\delta_2 = 0$. 57

5.2 Energy flux E_f in (5.5) versus time in days. A M2 barotropic tide is considered with amplitude $D = 0.2\text{ms}^{-1}$. The ambient internal wave has an amplitude $A_1(t = 0) = 0.1\text{ms}^{-1}$, of vertical mode 2, and of frequency $\omega_1 = 1.48\times10^{-4}\text{s}^{-1}$ at the latitude $15°N$. The newly-generated internal wave has a frequency $\omega_2 = 2.94\times10^{-4}\text{s}^{-1}$, of mode 1. Water depth is 4000 m for the average depth of the Pacific Ocean. Stratification is 5% between the densities of water on the free surface and the sea bottom. 58

6.1 Dimensionless frequency versus dimensionless wavenumber of free waves in a fluid of linearly stratified density $\rho(z) = \rho_0(1 - az)$, with $ah = 0.05$ (c.f. (6.10)). Associated with each wavenumber there is a single surface wave (green branch) and an infinite number of internal wave modes (blue branches). Frequency of internal waves cannot exceed the Brunt-Väisälä frequency (dash-dotted line). The figure also shows Bragg resonance condition: if an internal wave of wavenumber k_{in} arrives at the seabed corrugations of wavenumber k_b, a new (resonant) internal wave of wavenumber $k_r = k_{in} + k_b$ is excited. This new wave k_r with the same topography k_b satisfies (nearly) another Bragg condition with another resonant wave $k_{r2} = k_{in} + 2k_b$, and so on. Therefore energy of the initial wave k_{in} is gradually transferred to shorter waves. 64

6.1 (a,b) Time evolution of amplitude of a resonant wave A_1 and initial wave A_2 when different number of wave modes n are taken into account in the governing equation (6.18). For longer time interactions higher number of modes come into the play and hence must be taken into account. (c) Time evolution of amplitudes of the initial wave A_2 and a select of resonant waves $A_{1,3,4,8,12}$. Over time energy flows from lower wave number modes to higher ones. At later times new waves such as A_8 emerge, but they too give up their energy to even higher wave number modes (e.g. A_{12}). A single seabed component via Bragg resonance shifts the initial wave energy, one wave by one wave, to shorter and shorter waves. 67

6.1 Time evolution of the first four mode internal waves engaged in a Bragg resonance as calculated by our multiple-scale analysis (6.18) (legend 'a'), and direct simulation of full Euler's equation via MITgcm (legend 'n'). Both analytical and numerical results show the flow of energy from initial wave A_2 to eventually shorter waves. Chosen parameters are $ah = 0.05$, $\omega/\sqrt{ga} = 0.2$, $f_b/h = 0.02$, $k_b h = 0.64$, $A_{20} = 0.0015$m, $A_{i,0} = 0$ for $i \neq 2$, and n=20. 68

Acknowledgments

Foremost, I would like to express my sincere gratitude to my adviser Professor Mohammad-Reza Alam, for his continuous support of my PhD research, for his patience, encouragement, and immense knowledge. I could not imagine having a better adviser and mentor for my PhD study.

Beside my adviser, I would like to thank my other committee members Prof. Tarek I. Zohdi and Prof. Simo Mäkiharju for their insightful comments that made the thesis better.

My sincere thanks also go to my lab mates Dr. Louis-Alexandre Couston, Dr. Ahmad Zareei and Dr. Qiuchen Guo, Ninh Hai Do and Mehdi Mirzakhanloo. Their kindness and help made the lab a happy place to do research.

Last but not the least, I would like to thank my family, who have kept encouraging me through some hard times in the past few years. Their support keeps me going further in my life.

Chapter 1

Introduction

Internal gravity waves is a ubiquitous phenomenon in a density-stratified ocean. They mainly arise from wind disturbing the upper ocean mixed layer and barotropic tide flowing over topographic features in the ocean. Internal wave breaking increases ocean mixing, which can contribute to the large ocean circulation by lifting cold water from the ocean basin to the surface (Garrett, 2003a) and affects a wide range of ocean life by redistributing nutrients (Boyd, 2007; Harris, 1986). The stratification of abyssal oceans could not have been maintained without ocean mixing (Munk, 1966; Munk and Wunsch, 1998).

Internal gravity waves has been a subject of interest for many decades. Nevertheless, many aspects of their inception and fate is not well understood (e.g. Alford et al., 2015a). Specifically, the precise mechanism that transfers energy from longer waves to small scales, where internal waves are more prone to breaking and being dissipated, is yet a matter of dispute. It is generally believed that internal waves tend to break and get dissipated in small scales through couples of mechanisms, for example, interaction with bottom topography (Bühler and Holmes-Cerfon, 2011) and parametric subharmonic instability (PSI) (Davis and Acrivos, 1967; Hasselmann, 1967).

Resonant wave-wave interactions are known to play an important role in the re-distribution of energy across the oceanic wave spectrum (see e.g. Hammack and Henderson, 1993; Craik, 1986). The theory of wave-wave resonance was first introduced by Phillips(Phillips, 1960) for surface gravity waves. It was readily confirmed by experiments (e.g. Longuet-Higgins and Smith, 1966) and then extended and explored in numerous other wave systems. For instance, triad resonance interactions were found to occur between surface and interfacial waves in a two-layer stratified fluids (e.g. Ball, 1964), between internal waves in continuously stratified fluids (e.g. Thorpe, 1966), between gravity-capillary waves (e.g. Case and Chiu, 1977), and between mesoscale waves (e.g. Newell, 1969). A special type of triad resonance called parametric subharmonic instability that applies to internal waves of any amplitude (Lombard and Riley, 1996; Koudella and Staquet, 2006; Karimi and Akylas, 2014) is capable of transferring the energy of a primary wave to its subharmonics with larger vertical wave

numbers thus smaller scales.

Similar to wave-wave resonance, in finite-depth water where there is seabed topography, its effect enters the resonance equation in a way similar to the waves input, but with zero speed and frequency (like a frozen wave). Therefore, it may be possible that one or more of the propagating waves in a resonance group are replaced by Fourier components of the seabed topography. Inspecting the governing equations shows that this resonance mechanism, known as Bragg resonance, is indeed possible: in its simplest form, two surface waves and one seabed component form a triad resonance through which energy can flow from one surface wave to the other (Davies, 1982). Bragg resonance has received a great deal of attention due to its importance in spectral evolution over the continental shelves, potential applications in shore protection, and the formation of sandbars (e.g. Davies and Heathershaw, 1984; Mei, 1985; Dalrymple and Kirby, 1986; Elandt et al., 2014). Enhanced mixing has been observed close to topographic features in the ocean (Dauxois et al., 2004; Ledwell et al., 2000; Nash et al., 2004), indicating more internal wave breaking in such regions.

To understand how internal wave loses instability and possibly breaks, in this thesis I present some new findings on the instability mechanisms of internal gravity waves due to wave-wave/topography interactions.

In Chapter 2, I present dominant subharmonic waves generated by Parametric Subharmonic Instability (PSI) of internal gravity waves based on nonlinear stability analysis. It is well known that internal gravity waves are generally subject to subharmonic parametric instability, that is, they are unstable to a pair of subharmonic perturbing waves at lower frequencies with which the primary wave can form a resonant triad. It is now generally accepted that the subharmonic waves at half of the frequency of the primary wave have the largest growth rates and are expected to dominate in the wave field undergoing PSI. However, this understanding is not supported by laboratory experiments or numerical simulations to date. In the present study, I consider the nonlinear instability of the interaction equations. In contrast to the linearized instability theory that assumes a constant amplitude of the primary wave, interactions between different pairs of subharmonic waves are taken into account. I then find that it gives a quite different conclusion: the dominant subharmonic waves are not those predicted by linearized instability theory; the dominate waves do not occur at half of the frequency and large wave numbers as previously predicted from the linear stability theory.

In Chapter 3, I show that there exist internal gravity waves that are inherently unstable, that is, they cannot exist in nature for a long time. The instability mechanism is a one-way (irreversible) harmonic-generation resonance that permanently transfers the energy of an internal wave to its higher harmonics. I show that, in fact, there are a countably infinite number of such unstable waves. For the harmonic-generation resonance to take place, the nonlinear terms in the free surface boundary condition play a pivotal role, and the instability does not occur in a linearly-stratified fluid if a simplified boundary condition such as a rigid lid or a

linearized boundary condition is employed. Harmonic-generation resonance presented here provides a mechanism for the transfer of internal wave energy to the higher-frequency part of the spectrum hence affecting, potentially significantly, the evolution of the internal waves spectrum.

In Chapter 4, I show that monochromatic internal gravity waves in a stratified ocean can continuously descend to smaller scales of higher wave numbers after being reflected from no-penetration boundaries, provided their second harmonics satisfy dispersion relation. The wave with wave number k and frequency ω first generate its second harmonic due to the non-linearity in the momentum equation and the free surface boundary (Liang et al., 2017). Then the resonant interaction of the parent wave with its second harmonic gives rise to a $(3k, \omega)$ wave upon reflection, starting from which a series of triad resonances continuously form in the vicinity of the frequency ω or 2ω. The energy of the internal wave is sent to waves with higher and higher wave numbers. The mechanism potentially explains how part of internal wave energy converts from large scales to that of turbulent mixing near reflecting boundaries, such as ocean ridges and steep continental slopes.

In Chapter 5, I report a mechanism for conversion of tidal energy to internal gravity waves, through baratropic tidal currents interacting with ambient internal waves. The newly-generated internal waves have the same wave length as the ambient waves and frequencies higher by the tidal frequency. I show that they grow exponentially in time and continuously extract energy from the tidal currents. The mechanism exists in any stratified ocean with smooth density profiles and is only possible if a nonlinear free surface is taken into account. I show that for a typical water depth of 4000 m and density stratification 5% in the Pacific Ocean, the energy flux from baratropic tide to plane internal waves via this mechanism can reach order of 1MWm^{-1}. It therefore can be significant enough to account for a fraction of the 1TW total tidal energy loss in the open deep ocean.

In Chapter 6, I show in theory that, in a two dimensional domain, with a free surface taken into account, the interaction between an internal wave and corrugated bottom topography can efficiently generate a series of co-directional internal waves with higher wave numbers. As a result, the internal wave energy can be transferred to smaller scales where internal wave is more prone to breaking and being dissipated. This work can be extended to the interaction of internal waves with three dimensional bottom topography to account for more realistic ocean conditions.

Chapter 2

Dominant Resonance in Parametric Subharmonic Instability of Internal Waves

The underlying mechanism(s) that lead to the breaking of internal waves is not yet fully understood despite significant recent progresses made in our understanding of such waves. There is a nearly general consensus that low mode internal waves, such as those generated by tides, need to somehow transfer their energy to shorter waves which are steeper and hence more prone to breaking. Several mechanisms for such transfer of energy from long to short waves have been put forward, among them interaction with topographic features (Lamb, 2014; Sarkar and Scotti, 2017; Zhang and Swinney, 2014) and parametric subharmonic instability (e.g. Hasselmann, 1967; Davis and Acrivos, 1967; Scolan et al., 2013) are the most important ones.

Parametric Subharmonic Instability (PSI) is the instability of a primary internal wave to two lower-frequency internal waves with (initially) infinitesimal amplitudes thus disturbances. This happens if the primary and the two disturbance waves' frequencies and wavenumber vectors (respectively $\omega_{0,1,2}$ and $\mathbf{k}_{0,1,2}$) satisfy the triad resonance condition (e.g. Lombard and Riley, 1996; Karimi and Akylas, 2014; Koudella and Staquet, 2006)

$$\omega_0 = \omega_1 + \omega_2, \quad \mathbf{k}_0 = \mathbf{k}_1 + \mathbf{k}_2. \tag{2.1}$$

Through this instability, energy is transferred from the primary wave to the two disturbance waves. The flow of energy may continue until the amplitudes of the disturbance waves, initially infinitesimal, become of the same order as the amplitude of the primary wave or even higher, and that is why the disturbance waves are said to be resonated. This resonance is not through an explicit external force but instead is caused by what appears to be parameters in the governing equations, hence it is called parametric resonance or instability [1]. Resonated subharmonic waves obtained through PSI usually have smaller vertical and horizontal scales

[1] Some literature (e.g. Dauxois et al., 2018), to be precise, call this resonance a "Parametric Subharmonic instability or PSI" only if the disturbance waves have a frequency half of the frequency of primary wave. If the disturbance waves have a different frequency, then it is called "Triadic Resonant Instability or TRI".

than the primary wave. Thus, PSI constitutes a pathway for energy transfer to steeper waves which are more prone to breaking.

PSI was first studied (in 1960s, e.g. Hasselmann, 1967; Davis and Acrivos, 1967) as a subset of the general wave resonance theory (Phillips, 1981; Jiang and Marcus, 2009), and has since been reported in several field studies (e.g. Alford, 2008; Chinn et al., 2012). The current understanding of PSI is based on a linear stability theory (established in the 1970s, e.g. Martin et al., 1972; McEwan, 1971). Assuming that the amplitude of the primary wave is constant, and that amplitudes of disturbance waves are much smaller than the primary wave, the linear stability theory predicts an exponential growth rate for a pair of perturbing waves that satisfy the resonance conditions (2.1) (see e.g. Martin et al., 1972; Koudella and Staquet, 2006; Bourget et al., 2013).

An internal wave, however, can undergo parametric subharmonic instability simultaneously with a countably infinite pairs of subharmonic waves. In order to accurately determine the role of PSI on the evolution of oceanic internal wave spectrum as well as to answer how efficiently an internal wave can transfer its energy to smaller scales, it is critical to know which specific pair (or pairs) of disturbance waves draw the most energy from the primary internal wave. In other words, it is critical to know which triads are resonated the strongest out of all the different triad resonance possibilities. The classical linear stability theory assumes that these infinite resonance possibilities are independent (or decoupled) and predicts that the pair of subharmonic waves with half of the frequency of the primary wave and large wave numbers has the largest growth rates and thus is expected to dominate in the process of PSI. This understanding is widely-accepted in the community of ocean dynamics and physical oceanography nowadays (e.g., Benielli and Sommeria, 1998; Staquet and Sommeria, 2002; Olbers et al., 2012; Zhang and Duda, 2013; Gayen and Sarkar, 2013; Bourget et al., 2013).

However, laboratory and numerical experiments on PSI do not support the predominance of half frequency resonant waves. For example, in a series of experiments on PSI in a wave tank 21m long, 1.2m deep and filled with linearly stratified fluid, Martin et al. (1972) obtained multiple subharmonic waves generated from PSI of a mode-three internal wave, but none of them were at the half frequency. In another attempt, Joubaud et al. (2012) sends a horizontally propagating mode-one internal wave at frequency $0.95N$ (N: Brunt-Väisälä frequency) but observes two subharmonic waves not at the half frequency but at frequencies $0.38N$ and $0.57N$. Also, direct simulation of internal beams generated by a tidal flow (frequency ω_0) over bottom topography results in strongest subharmonic waves at frequencies $0.4\omega_0$ and $0.6\omega_0$ (Korobov and Lamb, 2008).

To address this discrepancy, here we consider the fully-coupled governing interaction equations that account for all triads satisfying PSI resonance condition (2.1). We solve this governing equation through multiple-scale analysis that obtains a uniformly-valid nonlinear instability solution. Our analysis determines that, contrary to linear stability theory prediction, it is a pair of subharmonic waves with frequencies different from $\omega_0/2$ that grow the largest in the PSI. In fact, in cases pairs of frequency $\omega_0/2$ receive the least amount of energy compared to other pairs in the pool of interactions.

Furthermore, internal waves with frequencies near $\omega_0/2$, as can be derived from equation (2.1), have very large vertical wavenumbers and therefore are very short. In fact, at exactly $\omega_0/2$, the vertical wavenumber is infinite. Strongest resonant waves of PSI, as predicted by the nonlinear stability theory, have frequencies far from ω_0 hence have finite wavenumbers. Therefore, nonlinear stability theory shows that the actual strongest resonant waves of PSI have much larger scales than what linear stability theory predicts.

While it is not unexpected that nonlinear theory results in a long-term growth which is different from the linear theory predictions, it is obvious that both linear and nonlinear theories must give the same initial growth rates. But, to our surprise, our initial growth rate from nonlinear stability theory did not match the prevalent linear growth rate reported in the literature. After some scrutiny we realized that in the classical theory the effect of the second exponential term has been mistakenly neglected, resulting in an incorrect reported initial growth rate. Specifically, in linear stability analysis, amplitude growth in a resonance is usually obtained in the form $A = a\mathrm{e}^{bt} + c\mathrm{e}^{-bt}$, and therefore the growth rate is $(1/A)(\mathrm{d}A/\mathrm{d}t) = b(a\mathrm{e}^{bt} - c\mathrm{e}^{-bt})/(a\mathrm{e}^{bt} + c\mathrm{e}^{-bt})$. While at large times (at which linear stability analysis is usually not valid) the growth rate tends to b, the initial growth rate is $b[1-2c/(a+c)]$, that depends on a, c and can potentially be very much different from b.

While applicable to lab experiments and high-frequency internal waves that are commonly seen in the ocean and stratified lakes (see e.g., Zalkan, 1970; Boegman et al., 2003; Rudnick et al., 2013), our nonlinear stability analysis can be extended to PSI of low-frequency internal waves that account for a large fraction of the total internal wave energy in the ocean, by including the Coriolis effect. In §2.3, we discuss the PSI of a mode-1 M2 internal tide and show that at latitudes other than 28.9°N, PSI in general does not occur half of the primary wave's frequency.

In what follows, we present our nonlinear stability analysis and discuss both initial growth rate and overall long-time growth of each resonance triads. We validate our analytical solution with direct numerical simulation results obtained from non-hydrostatic Navier-Stokes solver MITgcm.

2.1 Interaction Equations for Parametric Subharmonic Instability

Consider an inviscid, incompressible and stably-stratified fluid bounded by a top rigid lid and a flat seafloor at the bottom. In a Cartesian coordinates system with x, y-axes on the rigid lid and z-axis positive upward, the governing equations read

$$\rho_0 \mathscr{D}\mathbf{u}/\mathscr{D}t = -\nabla p - \rho g \nabla z, \quad -h < z < 0, \tag{2.2a}$$

$$\mathscr{D}\rho/\mathscr{D}t = 0, \quad -h < z < 0, \tag{2.2b}$$

$$\nabla \cdot \mathbf{u} = 0, \quad -h < z < 0, \tag{2.2c}$$

$$w = 0, \quad z = 0, \tag{2.2d}$$

$$w = 0, \quad z = -h, \tag{2.2e}$$

where $\mathbf{u} = \{u, v, w\}$ is the velocity vector, ρ is the density, p is the pressure, and g is the gravitational acceleration. A linear density profile is considered such that the background density is given by $\bar{\rho}(z)/\rho_0 = 1 - az$, with $\rho_0 = \bar{\rho}(z)|_{z=0}$. Equation (2.2a) is the momentum equation, (2.2b) represents conservation of salt (assuming that the density only depends on salinity in the equation of state and diffusion of salt is negligible), (2.2c) is conservation of mass, and equations (2.2d),(2.2e) are kinematic boundary conditions on the rigid lid and the sea bottom respectively.

System of equations (2.2) admits, among other solutions, a propagating internal-wave solution. Considering that a primary internal wave $(\mathbf{k}_0, \omega_0)$ with a finite initial amplitude co-exists with two perturbation waves $(\mathbf{k}_1, \omega_1)$ and $(\mathbf{k}_2, \omega_2)$ the vertical velocity to the leading order can be written in the form

$$w = \sum_{j=0,1,2} A_j \sin m_j(z+h) e^{i(k_j x - \omega_j t)} + \text{c.c.} \tag{2.3}$$

where $\mathbf{k}_j = k_j \hat{i} + m_j \hat{z}$, and c.c. denotes the complex conjugates. If triad resonance condition (2.1) is satisfied between the three waves, then amplitudes A_j will slowly change with time. Mathematically this is expressed by $A_j = A_j(\varepsilon t)$, that is, amplitudes are functions of slow time (ε is a small parameter and a measure of the waves' steepness).

Let's first define the following dimensionless variables

$$A_j^* = \frac{A_j}{A_{00}}, \quad t^* = \frac{t}{T_0} \cdot \frac{A_{00} T_0}{h}, \quad \omega_j^* = \frac{\omega_j}{N}, \quad k_j^* = k_j h, \quad m_j^* = m_j h.$$

where $A_{00} = A_0(t)|_{t=0}$. Through multiple-scale perturbation analysis, the differential equation that governs the evolution of a wave triad can be obtained, dropping all asterisks, as

$$\mathrm{d}A_0(t)/\mathrm{d}t = s_0 A_1(t) A_2(t) \tag{2.4a}$$

$$\mathrm{d}A_1(t)/\mathrm{d}t = s_1 A_0(t) \bar{A}_2(t) \tag{2.4b}$$

$$\mathrm{d}A_2(t)/\mathrm{d}t = s_2 A_0(t) \bar{A}_1(t) \tag{2.4c}$$

where $\bar{A}_{1,2}(t)$ are complex conjugates of $A_{1,2}(t)$, and $s_0 = \omega_0^3 S$, $s_1 = -\omega_1^3 S$, $s_2 = -\omega_2^3 S$ in which [2]

$$S = \frac{(k_1 m_2 - k_2 m_1)}{4 k_0 k_1 k_2 \omega_0 \omega_1 \omega_2} (k_1 \omega_2 - k_2 \omega_1) \left(\frac{k_0}{\omega_0} + \frac{k_1}{\omega_1} + \frac{k_2}{\omega_2} \right). \tag{2.5}$$

The interaction coefficients for the two perturbing waves s_1 and s_2 can be obtained by simply swapping the physical parameters in the expression for s_0 in (2.5) (c.f. e.g. Mcewan et al., 1972; Bourget et al., 2013).

[2] Our equation (2.5) is in fact the same as (3.26) presented in Bourget et al. (2013) except for the prefactor 1/4 which is due to Bourget et al. (2013) considering a vertically unbounded domain whereas in our study we have vertical wall boundaries. Therefore, in our case, unlike Bourget et al. (2013), we must have standing waves in the vertical direction and also can only have discrete vertical wavenumbers m.

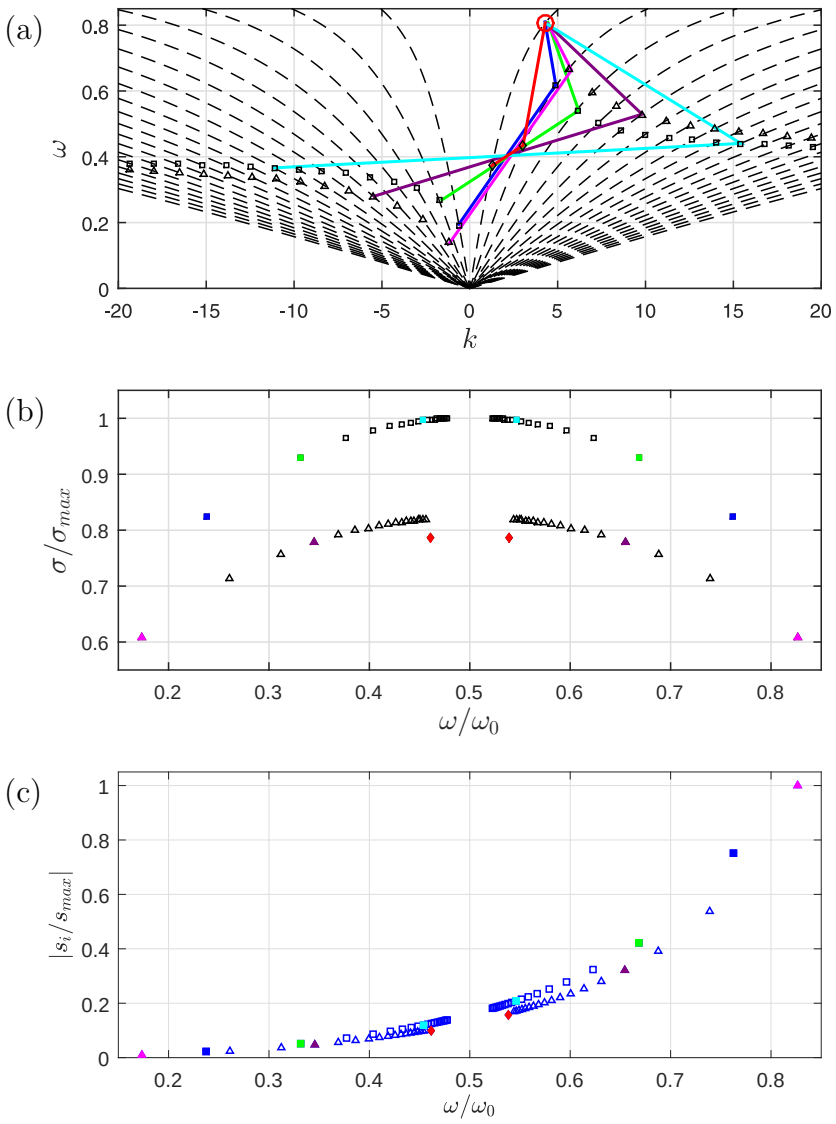


Figure 2.1: (a) Geometric construction of several of possible triad resonances (c.f. (2.1)) between a primary internal wave of ω=0.8 (red circle) and pairs of lower harmonic waves for ah=0.05. Square and triangles correspond to the higher mode propagating respectively in the same/opposite direction of the primary wave, and diamonds show a special case in which both subharmonic waves travel in the same direction. Six triads are highlighted by color solid lines. Black dashed lines show branches of the dispersion relation $\omega = |k/\sqrt{k^2+m^2}|$. (b) Variation of the normalized exponent (σ/σ_{max}) of linear stability analysis (2.7) as a function of normalized frequency ω/ω_0. Clearly subharmonic waves with frequencies close to $\omega/2$ have the highest exponents (c.f. figure 11b of Bourget et al., 2013). (c) Normalized interaction coefficient $|s_i/s_{max}|$ as a function of normalized frequency ω/ω_0. The maximum initial growth rate occurs at the frequency ω/ω_0=0.83 although σ is maximum at ω/ω_0=0.5.

The subharmonic waves generated in the process of PSI must satisfy the resonant condition (2.1) and the dispersion relation $\omega = |k/\sqrt{k^2+m^2}|$. As an example of the wave triads satisfying the resonance conditions, for the choice of $ah = 5\times10^{-2}$ and $\omega_0 = 0.8$, we present in figure 2.1a several of possible subharmonic wave triads that can be excited by PSI of the primary wave (red circle). The total number of triad possibilities is (countably) infinite. Note that there are two distinct branches of triads in figure 2.1a, marked by triangles and squares. Clearly, as the wavenumber of perturbation waves involved in the triad increases the frequency of perturbation waves asymptotically tend to half the frequency of the primary wave ($\omega_0/2$). In other words, perturbation waves with frequencies near $\omega_0/2$ have large horizontal and vertical wavenumbers, i.e., $|k_1,m_1| \approx |k_2,m_2| \gg |k_0,m_0|$ (c.f. e.g. Staquet and Sommeria, 2002).

Based on the linearized instability theory, i.e. assuming that the amplitude of the primary wave is constant (of course this only applies for the very initial period of the resonance), then (2.4) becomes,

$$dA_1(t)/dt = s_1 A_0 \bar{A}_2(t), \tag{2.6a}$$

$$dA_2(t)/dt = s_2 A_0 \bar{A}_1(t), \tag{2.6b}$$

where A_0 is a constant. If the initial amplitudes of the two perturbing waves are respectively $A_1|_{t=0} = \delta_1$ and $A_2|_{t=0} = \delta_2$, the solution to $A_1(t)$ is,

$$\begin{aligned} A_1(t) =& 1/2\left(\frac{s_1 A_0 \bar{\delta}_2}{\sigma} + \delta_1\right)\exp(\sigma t) \\ & - 1/2\left(\frac{s_1 A_0 \bar{\delta}_2}{\sigma} - \delta_1\right)\exp(-\sigma t) \end{aligned} \tag{2.7}$$

where $\sigma = \sqrt{s_1 s_2}|A_0|$. A similar expression is obtained for $A_2(t)$ with subscripts 1,2 in (2.7) swapped.

In classical theory of PSI, σ has been considered as the measure of growth of perturbation waves. We show in figure 2.1b the plot of σ/σ_{max} (i.e. σ normalized by the maximum σ found from all possible PSI triads) as a function of ω/ω_0, where ω refers to the frequency of perturbation waves. Colors of markers in figure 2.1b are associated with the colors of triads depicted geometrically in figure 2.1a. In each resonance, two perturbation waves are involved that are shown with a pair of same-color markers. For instance, triad of green color occurs between perturbation waves of frequencies $\omega_{1,2}/\omega_0$= 0.34, 0.66, and results in σ/σ_{max}=0.93. The two arc-shaped branches formed in this plot correspond to the two branches of triad possibilities in figure 2.1a (triangles and squares, as discussed before). Behavior of σ presented in figure 2.1b matches exactly figure 11b of Bourget et al. (2013) except that in our case because of two horizontal top and bottom boundaries we get discrete modes only.

Clearly figure 2.1b suggests that the maximum of σ is at ω/ω_0=0.5. But it is to be noted that this does not imply that the initial growth rate nor the long-time growth is highest at ω/ω_0=0.5. Specifically, at large t, it is in fact expected that the exponential term dominates

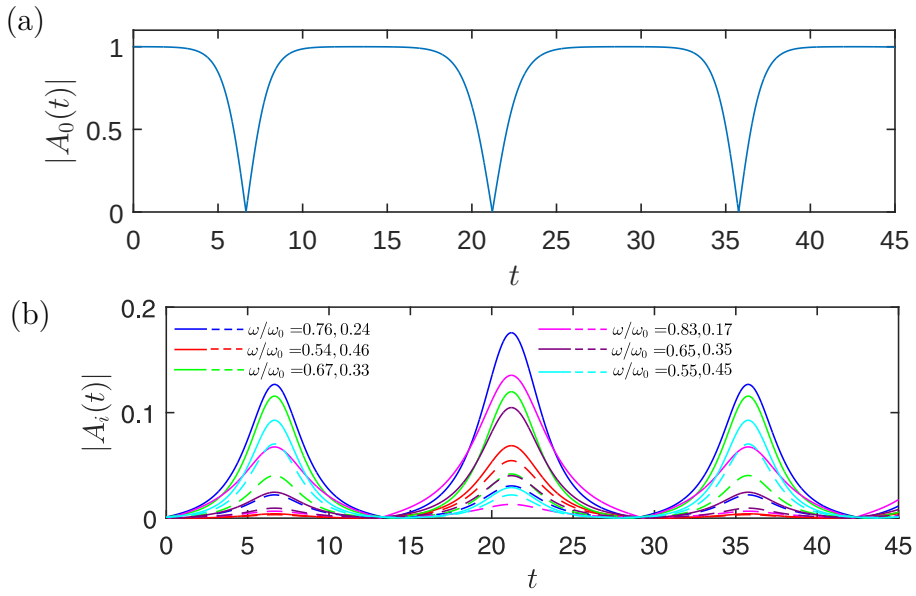


Figure 2.2: Evolution of amplitudes of (a) the primary internal wave and (b) the six subharmonic pairs undergoing PSI corresponding to the case represented in figure 2.1. Initial amplitudes of perturbation waves chosen as $A_{i1/i2}|_{t=0}$=0.001 and up to mode 20th (which results in 38 PSI pairs) are considered in the numerical integration of (2.9). All waves undergo a modulation in time, and the maximum growth is obtained for perturbation wave of ω/ω_0=0.76.

the behavior. However, the linear stability analysis is not valid for large t, and a nonlinear analysis must be called. The linear theory is only applicable at initial times, and the initial growth rate is given by

$$\left.\frac{dA_{1,2}(t)}{\mathrm{d}t}\right|_{t=0} = s_{1,2}A_0\bar{\delta}_{2,1}. \tag{2.8}$$

Effect of σ in the exponent, as can be seen from (2.7), is canceled by the coefficients in front, and therefore, the initial growth rate (2.8), is determined by $s_{1,2}$, and not σ. Behavior of normalized correct initial growth rate s_i/s_{max} plotted against ω/ω_0 (figure 2.1c) shows almost an opposite behavior when compared with that of σ. Most importantly, the highest value of correct initial growth rate s_{max}, does not occur at ω/ω_0=0.5, but at ω/ω_0=0.85. In fact, perturbation waves with frequencies near ω/ω_0=0.5 have almost the smallest initial growth rates[3].

[3]We would like to note that s_i for some of the perturbation waves is negative and therefore the amplitude will first decrease. Usually in such cases, since the amplitude of perturbation waves are initially small, the amplitude quickly decreases to zero and then starts to grow on the negative side. The negative amplitude means that the wave gains a π-radian phase difference.

2.2 Nonlinear Stability Analysis

To determine the long term growth of waves involved in PSI, nonlinear stability analysis must be conducted. Since all pairs of perturbation waves (that satisfy resonance condition) simultaneously interact with the primary wave, a correct from of (2.4) that takes into account the coupling between waves read

$$\mathrm{d}A_0(t)/\mathrm{d}t = \sum_{i=1}^{N} s_{i0}A_{i1}(t)A_{i2}(t) \tag{2.9a}$$

$$\mathrm{d}A_{i1}(t)/\mathrm{d}t = s_{i1}A_0(t)\bar{A}_{i2}(t) \tag{2.9b}$$

$$\mathrm{d}A_{i2}(t)/\mathrm{d}t = s_{i2}A_0(t)\bar{A}_{i1}(t) \tag{2.9c}$$

where subscript i denotes the ith subharmonic wave pair. From (2.9), it can be rigorously shown that

$$\frac{\mathrm{d}}{\mathrm{d}t}\left\{\frac{|A_0|^2}{\omega_0^2} + \sum_{i=1}^{N}\left[\frac{|A_{i1}|^2}{\omega_{i1}^2} + \frac{|A_{i2}|^2}{\omega_{i2}^2}\right]\right\} = 0, \tag{2.10}$$

which shows that our governing equation (2.9) conserves energy. In other words, although energy is exchanged between a large number of waves, the total energy of the system is conserved and does not change with the time.

As a case study, consider a primary internal wave of $\omega_0 = 0.8$ in a stratified water of $ah = 5\times10^{-2}$ which is correspond to figure 2.1. If we consider wave modes up to the mode 20th, that is 20 branches of the dispersion relation plot (dashed lines) in figure 2.1a, then 38 pair of perturbation waves can be found to form resonance with our primary wave (6 of them are shown in figure 2.1a). We assume all these perturbation waves have the same initial amplitude A_i=1×10^{-3}, which corresponds to a white-noise-like distribution of perturbation waves in the environment. Results of long time evolution of the primary wave, as well as few important perturbation waves, are shown in figure 2.2a,b: at the stage t <6.8, amplitudes of some of perturbation waves increase, in cases substantially and even by orders of magnitudes, at the expense of a decrease in the energy of primary wave. Once the entire energy of the primary wave is depleted, then the process reverses and now energy flows back from (initially) perturbation waves to the primary wave. This modulation continues with a period of $T_i \sim$ 15 for primary wave and with the period of $T_p \sim 2T_i$ for perturbation waves.

The most important feature of long-time evolution plots (figure 2.2b) is the fact that the largest growth is observed at frequency ω/ω_0 =0.76 (A_i =0.18 at t=21.7). The second and third largest growth are respectively at frequency ω/ω_0 =0.83 (A_i =0.13 at t=21.7) and ω/ω_0 =0.67 (A_i =0.12 at t=21.7); none at the frequency ω/ω_0 =0.5. The perturbation wave associated with ω/ω_0 =0.55 (which is closest to 0.5 in our database) gains a maximum value of $A_i = 0.093$ which is barely 50% of the highest growth. We test a variety of cases with different sets of physical parameters and background disturbances, the time evolutions of the primary wave and the subharmonic waves are qualitatively similar to the curves in figure

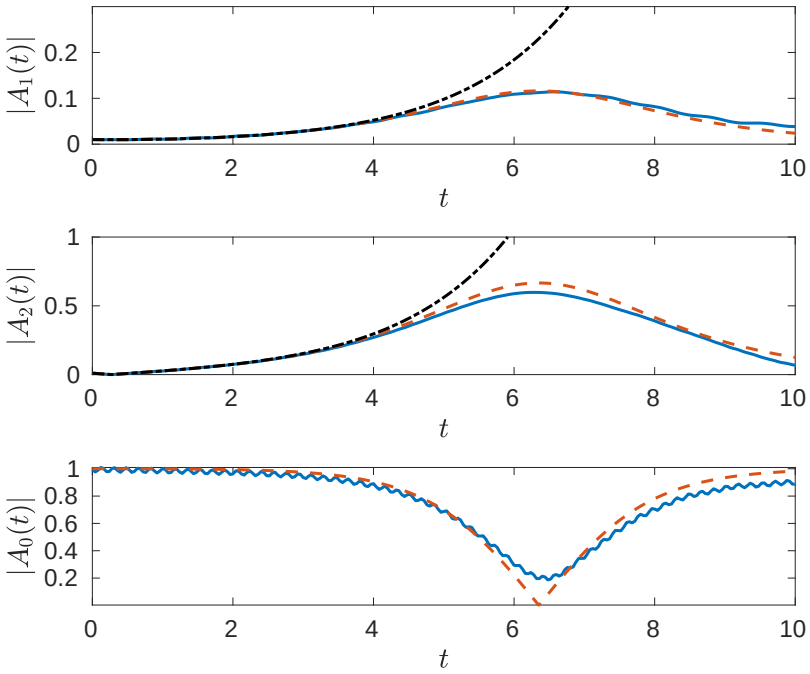


Figure 2.3: Time-evolution of a primary internal wave of frequency $\omega = 0.8$ with two perturbation waves of frequencies $\omega_{1,2}/\omega_0$=0.24,0.76. Direct simulations results of MITgcm (blue solid line) matches well with our analytical results using nonlinear stability theory though numerical integration of (2.9) (red dashed line). For comparison, growth rate prediction by linear stability theory (black dash-dotted line) are also shown. Physical parameters for MITgcm simulations are $a = 5 \times 10^{-5}\mathrm{m}^{-1}$, $h = 1000\mathrm{m}$ and initial amplitude is 1m for the primary wave and 0.01m for each of the two subharmonic waves.

2.2: The primary wave loses all its energy to the subharmonic waves at some points; the dominant subharmonic waves are not found at $\omega_0/2$ and their wavelengths are much longer than is predicted from the linear stability theory.

We validate our analytical predictions with direct simulation run by MITgcm (Marshall et al., 1997). MITgcm is a finite-volume based open-source non-hydrostatic Navier-Stokes solver that is widely used for modeling stratified mediums (e.g. Engqvist and Hogg, 2004; Klymak et al., 2010; Lim et al., 2010; Churaev et al., 2015; Alford et al., 2015b). We consider a rectangular domain with a periodic boundary condition on both ends in the x-direction, a free-slip wall at the bottom, and a free-slip rigid lid at the top. We use physical parameters $a = 5 \times 10^{-5}\mathrm{m}^{-1}$, $h = 1000\mathrm{m}$ and consider a primary wave of mode one with $\omega_0 = 0.806$, $A_0|_{t=0}$=1m, that resonates two subharmonic waves of frequencies $\omega_{1,2}/\omega_0$ =0.24, 0.76, $A_{1,2}|_{t=0}$=0.01m [4]. The evolution of amplitude of the three waves over time obtained

[4]This specific pair of subharmonics are intentionally chosen since their wavenumber are $k_{1,2}/k_0$=-1/7,8/7 allowing us to use a periodic domain in the x-direction.

from the direct simulation of MITgcm (blue solid lines in figure 2.3) compares well with our analytical results obtained from (2.9) (red dashed curves). For comparison, we also show the results of linear stability analysis (black dash-dotted lines) on top of the other two curves. Clearly, at the initial stage of resonance and as long as the change in the amplitude of A_0 is small, linear stability analysis estimates the growth of perturbations with a satisfactory tolerance. But for later stages, linear theory over-predicts the growth.

2.3 Parametric Subharmonic Instability of A Mode-1 M2 Internal Tide

While applicable to lab experiments and high-frequency internal waves that are commonly seen in the ocean and stratified lakes (see e.g., Zalkan, 1970; Boegman et al., 2003; Rudnick et al., 2013), our nonlinear stability analysis can be extended to PSI of low-frequency internal waves that account for a large fraction of the total internal wave energy in the ocean, by including the Coriolis effect. In this section, we discuss the PSI of a mode-1 M2 internal tide and show that at latitudes other than 28.9°N, PSI in general does not occur half of the primary wave's frequency.

To see how our theory applies to oceanography, here we consider the parametric subharmonic instability of low-frequency internal waves in the ocean. (2.2) including Coriolis forces becomes

$$\rho_0 \mathscr{D}\mathbf{u}/\mathscr{D}t + \mathbf{f}\times\mathbf{u} = -\nabla p - \rho g \nabla z, \quad -h < z < 0, \tag{2.11a}$$
$$\mathscr{D}\rho/\mathscr{D}t = 0, \quad -h < z < 0, \tag{2.11b}$$
$$\nabla\cdot\mathbf{u} = 0, \quad -h < z < 0, \tag{2.11c}$$
$$w = 0, \quad z = 0, \tag{2.11d}$$
$$w = 0, \quad z = -h, \tag{2.11e}$$

where $\mathbf{f} = \{0, 0, f\}$ is the planetary vorticity and $f = 2\Omega\sin\phi$ where ϕ is the latitude.

The differential equation that governs the evolution of a wave triad remains the same as (2.9) except the interaction coefficient s_0 becomes

$$s_0 = \frac{(k_1+k_2)(k_1m_2-k_2m_1)}{4k_1k_2(\omega_1+\omega_2)(k_0^2+m_0^2)}\left\{\omega_0(k_1^2+m_1^2-k_2^2-m_2^2)+N^2k_0(\frac{k_1}{\omega_1}-\frac{k_2}{\omega_2})+f^2m_0(\frac{m_1}{\omega_1}-\frac{m_2}{\omega_2})\right\} \tag{2.12}$$

where the Coriolis effect has been included. Setting $f = 0$ in (2.12) gives (2.5).

Possible Subharmonic Waves

We consider a most relevant case in oceanography: a mode-1 M2 internal tide, with vertical wave number $m_0 = \pi/h$ where h is water depth. For PSI to occur, (2.1) needs to be satisfied. Given the frequency ω_0 and horizontal wave number k_0 of the M2 internal tide, the subharmonic waves should satisfy

$$\omega_1 + \omega_2 = \omega_0, \tag{2.13a}$$
$$k_1 + k_2 = k_0, \tag{2.13b}$$
$$m_1 + m_2 = m_0, \tag{2.13c}$$

Applying the dispersion relation $m^2 = k^2(N^2 - \omega^2)/(\omega^2 - f^2)$ and substituting the value of m_0, (2.13) can be shown to be equivalent to

$$s_1 n_1 \sqrt{\frac{\omega_1^2 - f^2}{N^2 - \omega_1^2}} + s_2 n_2 \sqrt{\frac{(\omega_0 - \omega_1)^2 - f^2}{N^2 - (\omega_0 - \omega_1)^2}} = \sqrt{\frac{\omega_0^2 - f^2}{N^2 - \omega_0^2}} \tag{2.14}$$

where n_1 and n_2 are positive integers representing the mode numbers of the subharmonic waves. Since the M2 internal tide in consideration is of mode 1, $|n_1 - n_2| = 1$. s_1 and s_2 are sign functions : if the subharmonic waves propagate in the same direction as the M2 internal tide, they take $+1$, otherwise -1.

Solving (2.14) obtains the possible subharmonic waves to appear when PSI occurs. At the critical latitude 28.9°N, the frequency of M2 tide is twice as large as the Coriolis frequency, i.e., $\omega_0 = 2f$. The only solution to (2.13) is $\omega_1 = \omega_2 = \omega_0/2$ and k_1, k_2, m_1, m_2 approach infinity. For this reason, the subharmonic waves excited from PSI at this latitude are expected to be at frequency $\omega_0/2$.

PSI of mode-1 M2 Tide at Latitudes other than 28.9°N

However, only modest dissipation of internal tide due to PSI is seen near the critical latitude (e.g., MacKinnon et al., 2013; Richet et al., 2017). Field observations Xie et al. (2011); Richet et al. (2017); Sun and Pinkel (2012), as well as numerical simulations Korobov and Lamb (2008); Chalamalla and Sarkar (2016) reveal that effective parametric subharmonic instability occurs latitudes other than 28.9°N, and PSI at these latitudes does not occur at half of the primary wave's frequency.

In this section, we will show from our theory, that the PSI of a mode-1 M2 tide in general does not occur at half of the primary wave's frequency, i.e., $\omega_0/2$, at latitudes other than 28.9°N.

Korobov and Lamb (2008) numerically simulated low-mode M2 internal tides subject to PSI and generation of higher harmonics, and showed at latitudes other than 28.9°N, PSI does not occur at half of the M2 tidal frequency. Our analytical analysis agrees with this

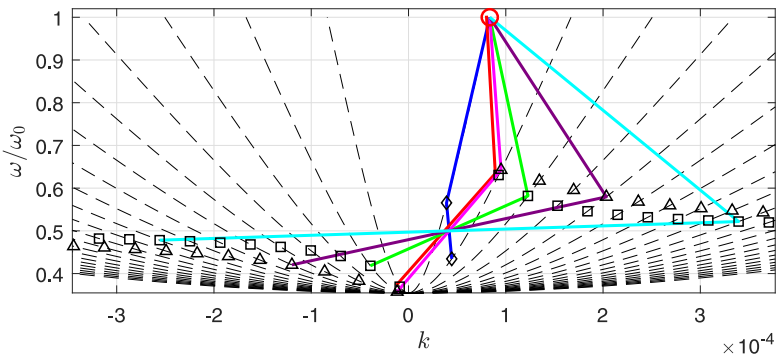


Figure 2.4: Possible subharmonic waves from the parametric subharmonic instability of a mode-1 M2 internal tide (primary wave) for oceans where Brunt-Väisälä frequency $N = 10^{-3}\mathrm{s}^{-1}$. Square and triangles correspond to the higher mode propagating respectively in the same/opposite direction of the primary wave, and diamonds show a case in which both subharmonic waves travel in the same direction. Black dashed lines show branches of the dispersion relation $m^2 = k^2(N^2 - \omega^2)/(\omega^2 - f^2)$.

result. For comparison, we consider a mode-1 M2 internal tide at the latitude 20°N where the Brunt-Väisälä frequency $N = 10^{-3}\mathrm{s}^{-1}$. These parameters are used in the third case in Korobov and Lamb (2008) .

In figure 2.4, we present the possible subharmonic waves from the parametric subharmonic instability of a mode-1 M2 internal tide for oceans with Brunt-Väisälä frequency $N = 10^{-3}\mathrm{s}^{-1}$. As wave number increases, the frequencies of subharmonic waves continuously approach $\omega_0/2$. The pair of subharmonic waves that propagate in the same direction as the primary wave has frequency $0.434\omega_0$ and $0.566\omega_0$.

We again consider a white-noise background disturbances where the amplitudes of the subharmonic waves are $1 \times 10^{-10}\mathrm{ms}^{-1}$, and the amplitude of the primary wave's vertical velocity is $0.05\mathrm{ms}^{-1}$. According to our dimensional analysis, with other parameters fixed, the ratio of the two amplitudes determines the magnitudes of the subharmonics in the resulting spectrum from PSI.

We can see from figure 2.5 that the dominant subharmonic waves are shown to occur at $0.566\omega_0$ and $0.434\omega_0$, which matches the numerical simulation of Korobov and Lamb (2008) in predicting the frequency of dominant resonance.

According to a variety test cases we run at other latitudes, we find that primarily low-mode subharmonic waves are excited in the precess of PSI. They are in general not at frequency $\omega_0/2$ and have much longer wave lengths than is previously predicted from linear stability theory.

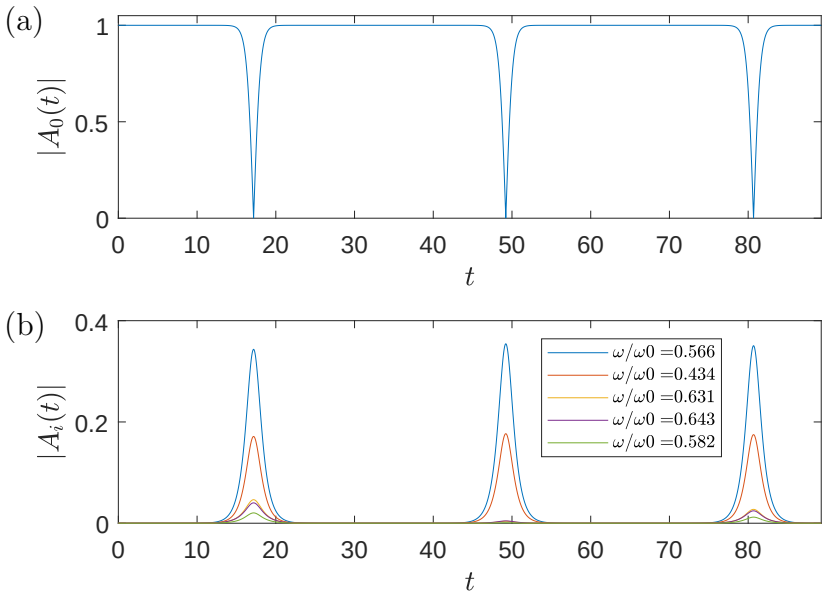


Figure 2.5: Evolution of amplitudes of (a) the mode-1 M2 internal tide and (b) the largest five subharmonic waves. Up to mode 20th are considered in the numerical integration of (2.9). The maximum growth is obtained for the subharmonic wave at ω/ω_0=0.566 and 0.434.

2.4 Conclusion

In summary, we showed, contrary to widely-accepted results drawn from linearized instability theory, that Parametric Subharmonic Instability (PSI) is strongest among a primary internal waves and perturbation waves at frequencies different from half the frequency of internal wave. Specifically, we proved that both the initial growth rate and the maximum amplitude reached by the (initially) perturbation waves are highest for subharmonic waves of low vertical modes with frequencies higher than $\omega_0/2$. It is straightforward to show that similar conclusion holds also in the spatial (or boundary value) problem, i.e. as waves propagate away from a source (e.g. a wavemaker) and interaction develops over the distance (c.f. e.g. Alam et al., 2009a). Our finding suggests that the efficiency of converting internal wave energy from large scales to small scales through PSI may have been overestimated by previous studies, and dominant resonant waves may have been missed if sought at the half frequency. The effect of our nonlinear stability analysis on a continuous internal wave spectrum can be derived: since for any discrete waves, PSI in general does not occur at $\omega_0/2$ and very large wave numbers as is predicted from linear stability theory, given a continuous internal wave spectrum, the resulting spectrum from PSI are not expected to have half frequency band of

the original one, and large wave numbers should not be highlighted. [5]

[5]see a similar comment on transition of wave resonance of discrete waves to continuous spectrum in (McComas and Bretherton, 1977).

Chapter 3

Inherently Unstable Internal Gravity Waves due to Resonant Harmonic Generation

All discovered destabilizing mechanisms for an internal wave , have one thing in common that they require some type of perturbations in order to get initiated. These perturbations can come from, for instance, the seabed corrugations or the presence of other waves forming resonance triads.
Here, we show that there are internal gravity waves in the ocean that are inherently unstable, that is, they simply cannot sustain their form. Through the mechanism studied here, specific internal waves naturally (without requiring any perturbation) give up their energy permanently to their higher harmonics through a one-way irreversible harmonic-generation resonance mechanism.

3.1 Governing Equations and Dispersion Relation

Consider the propagation of internal waves in an inviscid, incompressible, adiabatic and stably stratified fluid of density $\rho(x,y,z,t)$, bounded by a free surface on the top and a rigid seafloor at the depth h. Let's define a Cartesian coordinate system with x,y-axes on the mean free surface and z-axis positive upward. Newton's second law, conservation of mass, and conservation of salt provide five equations for the evolution of the components of the velocity vector $\mathbf{u} = \{u,v,w\}$, density ρ, and the pressure p. These governing equations under Boussinesq approximation together with three boundary conditions (two kinematic boundary conditions on the free surface and the seabed, and one dynamic boundary condition on the free surface) uniquely determine the five unknowns and the surface elevation $\eta(x,y,t)$ (e.g. Thorpe, 1966).
We assume internal waves are small perturbations to a stable background state at equilibrium. Therefore, density can be written as $\rho(x,y,z,t) = \bar{\rho}(z) + \rho'(x,y,z,t)$ where $\bar{\rho}(z)$ is the background (unperturbed) density. Similarly, we define a pressure perturbation p' via $p = \bar{p}(z) + p'(x,y,z,t)$ such that $d\bar{p}(z)/dz = -\bar{\rho}(z)g$. With some standard manipulation, the

governing equations can be written in terms of either of the five variables involved in this problem. We choose to write the equation, as is customary, in terms of the vertical component of the velocity, w. These equations then read (see e.g. Thorpe, 1966, or Appendix)

$$\frac{\partial^2}{\partial t^2}\nabla^2 w + N^2\nabla_H^2 w = \mathscr{E}(\mathrm{u},\rho'), \qquad -h < z < \eta, \tag{3.1a}$$

$$\frac{\partial^3 w}{\partial z \partial t^2} - g\nabla_H^2 w = \mathscr{F}(\mathrm{u}, p', \eta), \qquad z = 0, \tag{3.1b}$$

$$w = 0, \qquad z = -h. \tag{3.1c}$$

where $\nabla_H^2 = \partial^2/\partial x^2 + \partial^2/\partial y^2$ is the horizontal Laplacian, $N^2 = -g/\rho_0 \, \mathrm{d}\bar{\rho}(z)/\mathrm{d}z$ is the Brunt-Väisälä frequency in which $\rho_0 = \bar{\rho}(z=0)$ is the density on the free surface, and $\mathscr{E}, \mathscr{F}$ are nonlinear functions of their arguments.

To perform a perturbation analysis, we assume that the solution to (3.1) can be expressed in terms of a convergent series, i.e.

$$w(\mathrm{x},t) = \varepsilon w^{(1)}(\mathrm{x},t) + \varepsilon^2 w^{(2)}(\mathrm{x},t) + \mathscr{O}(\varepsilon^3), \tag{3.2}$$

where $\varepsilon \ll 1$ is a measure of steepness of the waves involved and $w^{(i)} \sim \mathscr{O}(1)$. Similar expressions hold for u, v, ρ' and p'. Substituting (3.2) into (3.1) and collecting terms of the same magnitude, then at the leading order $\mathscr{O}(\varepsilon)$ the linearized equations are obtained.

We focus our attention here on the two-dimensional problem with a linear mean density profile, i.e. $\bar{\rho}(z) = \rho_0(1 - az)$ which gives a constant Brunt-Väisälä frequency $N = \sqrt{ga}$ (c.f. e.g. Martin et al., 1972). Looking for a progressive wave solution of the leading order (linearized) equation in the form $w^{(1)} = W(z)\sin(\mathbf{k}\cdot\mathbf{x} - \omega t)$ the following dispersion relations result:

$$\mathscr{D}(k,\omega) = \begin{cases} \omega^2 - \frac{gk}{\sqrt{1-N^2/\omega^2}} \tanh\left(kh\sqrt{1-N^2/\omega^2}\right) = 0, & \omega > N \\ \omega^2 - \frac{gk}{\sqrt{N^2/\omega^2-1}} \tan\left(kh\sqrt{N^2/\omega^2-1}\right) = 0, & \omega < N \end{cases} \tag{3.3}$$

Solutions to the above dispersion relation identify permissible frequency and wavenumber of free propagating waves. Contours of $\mathscr{D}(k,\omega) = 0$ are shown in figure 3.1 in which we plot the dimensionless frequency ω/N as a function of dimensionless wavenumber kh (blue solid curves). For $\omega > N$ only one solution exists in the first quadrant (with its mirror in the other quadrants). This solution corresponds to a wave whose associated fluid particle motion is maximum near the free surface and decreases as the depth increases. Therefore this is basically a classical surface wave which is perturbed slightly because of stratification. For $\omega < N$ there is an infinite number of solutions to (3.3). The first member of this set, is the continuation of the surface wave branch (the left-most branch in figure 3.1), but the rest identify waves with associated fluid particles' vertical velocities w that are zero at the

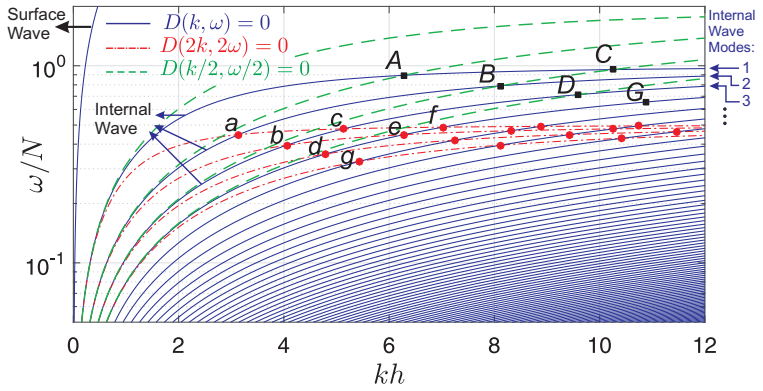


Figure 3.1: Plot of the dimensionless frequency ω/N as a function of dimensionless wavenumber kh of free internal waves (i.e. $\mathscr{D}(k,\omega)=0$) in a fluid of linearly stratified density $\rho(z)=\rho_0(1-az)$, with $ah=0.05$. Associated with each wavenumber there is one surface wave and an infinite number of internal wave modes (blue solid-line branches). The frequency of internal waves cannot exceed the Brunt-Väisälä frequency N, and all branches of the dispersion relation curve are capped at ω/N=1. We also plot contours of $\mathscr{D}(2k,2\omega)$=0 (red dash-dotted lines) whose intersections with blue lines (shown by red circles) mark waves whose second harmonics are also solutions to the dispersion relation. These second harmonics are at the intersections of contours of $\mathscr{D}(k/2,\omega/2)$=0 (green dashed lines) and $\mathscr{D}(k,\omega)$=0 and are marked by black squares. The second harmonic of the wave at "a" (mode 2), is the wave "A" (mode 1) and so on.

seabed and close to zero near the free surface, but gain one (or more) maximum/maxima somewhere inside the fluid domain. Therefore these branches show internal waves. The number of maxima in the amplitude of the vertical velocity w along the vertical water line determines the mode number of the branch (the first three are marked on the right-side of figure 3.1 with arrows). A cut-off frequency ω/N=1 sets an upper frequency limit for internal waves. We would like to emphasize that the free surface boundary condition, in comparison with the rigid lid case, leads to a drastically different expressions for mode structures and the dispersion relation. Nevertheless, the curves of the dispersion relation (3.2) are very close to the one under rigid lid assumption $\omega=N/\sqrt{1+(n\pi/kh)^2}$.

It can be seen from figure 3.1 that second harmonic waves are at least one mode lower than the original waves. Therefore, clearly a mode one internal wave can never generate a second harmonic, since its second harmonic must be a mode zero which is non-existent. But mode two internal waves can go unstable and resonate mode one waves. Therefore, in an internal wave spectrum, there might be mode one waves whose origin is different from the origin of the rest of the incident mode-one internal waves; that is, they are results of instability of mode two (and other higher modes) internal waves.

We would like to comment that the dominant energy in the baroclinic tide, which is the most relevant case for the ocean, is in the vertical mode one. However, most of the prevalent

low-mode internal waves (including mode one) are eventually dissipated through their energy being transferred to waves with higher vertical wave numbers (see e.g. Garrett, 2003b). This happens through a number of mechanisms including, for instance, parametric subharmonic instability (aka PSI, e.g. Davis and Acrivos, 1967) and interaction with the bottom topography (e.g. Bühler and Holmes-Cerfon, 2011; Karimpour et al., 2017; Couston et al., 2017). Resonant harmonic generation studied here may interfere, potentially substantially, in this process of energy exchange between different modes. In other words, the mechanism studied here can influence the internal wave spectral evolution by opening up a new avenue for the energy exchange between different modes.

3.2 Harmonic Generation

With the linear solution to (3.1) and its properties at hand, we move to the second order equation by collecting $\mathscr{O}(\varepsilon^2)$ terms obtained from the substitution of (3.2) into (3.1). The second order equation has the exact same form as of the leading order equation on its left-hand side, but with nonlinear terms, arising from nonlinear functions $\mathscr{E},\mathscr{F}$, on its right-hand side. These nonlinear terms are multiplication of the linear solution (and its derivatives) and, it turns out that, they constitute forcing terms with wavenumber and frequency $(2k,2\omega)$. Now if $\mathscr{D}(2k,2\omega)$=0, then it means that these forcing terms have a harmonic which is the same as the natural harmonic of the linear system. This is a resonance scenario through which a new second order solution may emerge and may grow large enough to the extent that it becomes comparable to the leading order solution. We would like to note a subtle point here that at the second order the right-side of (3.1a) is identically zero (see e.g. Tabaei et al., 2005). Therefore a potential harmonic-generation resonance is only possible through the nonlinear terms in the free surface boundary condition (3.1b). If a rigid-lid assumption or a linearized form of the free surface boundary condition is employed (which is usually the case in the investigation of internal waves) the resonance harmonic generation will simply not obtain unless a non-uniform stratification or Boussinesq terms are considered.

To see whether it is possible to satisfy the resonance condition required for the second harmonic of an internal wave to exist as a free propagating wave, we also plot in figure 3.1 the contours of $\mathscr{D}(2k,2\omega)$=0 (red dash-dotted curves) for first four internal wave modes. Intersections of these contours with the contours of $\mathscr{D}(k,\omega)$=0 (solid blue curves) identify waves whose second harmonics are also solutions to the dispersion relation. Some of these intersections are marked in figure 3.1 by red circles and are identified by lowercase characters. It is easy to find the corresponding second harmonic by multiplying a designated (red circle) frequency and wavenumber by a factor of two, or alternatively by finding intersections of contours of $\mathscr{D}(k/2,\omega/2)$=0 (green dashed curves) and $\mathscr{D}(k,\omega)$ (denoted by black squares and uppercase characters). Specifically, "A" is the second harmonic of "a", "B" is the second harmonic of "b" and so on. It is to be noted that the second harmonic of an internal wave always belongs to a lower mode than the mode of the original wave. For example, second harmonic of wave "a" (mode 2) is the wave "A" (mode 1), and second harmonic of wave "c"

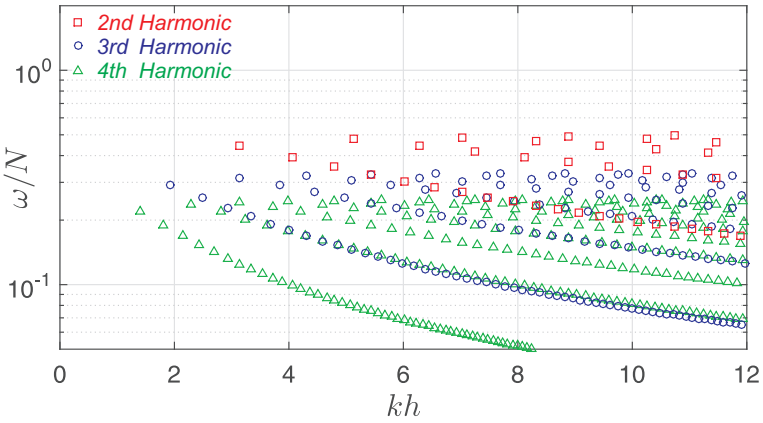


Figure 3.2: There are countably infinite number of internal waves that are unstable to their second harmonic. Physically this means that specific incident internal waves of wavenumber and frequency (k, ω) will give up their energy permanently (in a one-way irreversible process, c.f. equation (3.5)) to their second harmonic $(2k, 2\omega)$. The necessary condition for this to happen is $\mathscr{D}(k, \omega) = \mathscr{D}(2k, 2\omega)$=0. These waves, for the parameters of figure 3.1, are shown here by red squares. Similar story holds for another set of waves that are unstable to their third harmonic (blue circles, necessary condition $\mathscr{D}(k, \omega) = \mathscr{D}(3k, 3\omega)$=0), and fourth harmonic (green triangles, $\mathscr{D}(k, \omega) = \mathscr{D}(4k, 4\omega)$=0) and so on.

(mode 3) is the wave "C" (mode 1).

A comprehensive collection of all internal waves (for kh <12) whose second harmonics are also free propagating waves is shown in figure 3.2. We are basically plotting in this figure all intersections points of contours of $\mathscr{D}(k, \omega) = 0$ and contours of $\mathscr{D}(2k, 2\omega) = 0$. Clearly there will be an infinite (but countable) number of such solutions. Through the approach described above, a similar exercise can be performed for waves with their third harmonic being free waves. These solutions are marked by blue circles in figure 3.2, and waves with their fourth harmonics lying on the dispersion relation curves are shown by green triangles, and this search can continue indefinitely. In a weakly nonlinear wave propagation problem, instabilities to higher harmonics (e.g. third, fourth, etc) are much weaker compared with the instability to the second harmonic. This is because the expression for the amplitude growth of higher harmonics contains higher order perturbation terms. Specifically, if ε is a measure of a wave steepness, then the amplitude growth rate of its second harmonic wave is of $\mathscr{O}(\varepsilon^2)$, but if its third harmonic is excited then the growth rate is of $\mathscr{O}(\varepsilon^3)$ (c.f. the difference between Class I and Class II/III Bragg resonance, e.g. Alam et al., 2009b).

3.3 Results and Discussions

To determine the strength of the resonance (i.e. the rate of growth of the resonant wave), and the dynamics of the energy interplay between a wave and its second harmonic, here we

perform a multiple scale perturbation analysis. The basic assumption is that the original wave and its second harmonic are both functions of spatial variables and time (i.e. x,t), as well as a slow spatial variable in the direction of propagation $x_1 = \varepsilon x$. Physically speaking, we allow the amplitude of both waves to slowly vary as waves propagate. Mathematically speaking this is written as

$$w(x,x_1,z,t) = \varepsilon w_1(x,x_1,z,t) + \varepsilon^2 w_2(x,x_1,z,t) + \mathscr{O}(\varepsilon^3) \tag{3.4}$$

where $w_i \sim \mathscr{O}(1)$. Expressions of the same form are assumed to hold for other variables u, ρ', p' and η. Similar to regular perturbation methodology, described earlier in the paper to gain insight into the problem, we substitute (3.4) into the governing equation (3.1) and collect terms of the same order in ε. We assume the original wave with wavenumber and frequency k, ω has the amplitude $\mathscr{A}_1(x_1)$ and the amplitude of resonant second harmonic wave with wavenumber and frequency $2k, 2\omega$ is $\mathscr{B}_2(x_1)$. At the second order, applying a compatibility condition (to avoid unbounded solutions) the following two equations governing spatial evolution of $\mathscr{A}_1(x_1)$ and $\mathscr{B}_2(x_1)$ emerge (see Appendix for details of derivation)

$$\frac{\mathrm{d}\mathscr{B}_2(x_1)}{\mathrm{d}x} = \alpha \mathscr{A}_1^2(x_1), \tag{3.5a}$$

$$\frac{\mathrm{d}\mathscr{A}_1(x_1)}{\mathrm{d}x} = \beta \mathscr{A}_1(x_1)\mathscr{B}_2(x_1), \tag{3.5b}$$

where

$$\alpha = -\frac{6m_1^2\omega\cos m_2 h}{gk(2m_2h + \sin 2m_2h)},$$

$$\beta = -\frac{k[\sin m_2h(4m_1\cos^2 m_1h - 3m_1) - 2m_2\cos m_2h \sin 2m_1h]}{2\omega(2m_1h + \sin 2m_1h)},$$

in which $m_1 = k\sqrt{N^2-\omega^2}/\omega$ and $m_2 = k\sqrt{N^2-4\omega^2}/\omega$.
Spatial evolution of the normalized amplitude of the original wave $\mathscr{A}_1/\mathscr{A}_{10}$ (where $\mathscr{A}_{10} = \mathscr{A}_1(x=0)$) and its second harmonic $\mathscr{B}_2/\mathscr{A}_{10}$ as a function of spatial distance of propagation x/λ_i (where $\lambda_i = 2\pi/k$= wavelength of the original wave) is shown in figure 3.3 respectively by blue-dashed line and solid-red line. In accordance with the case presented in figure 3.1, we choose ah=0.05 and we consider that waves are propagating in a water of depth h=1 km, then N=0.02 rad/s. For this case, figure 3.3a corresponds to the point "a" (kh=3.144772,ω/N=0.4472136) with its second harmonic at "A" in figure 3.1, and figure 3.3b corresponds to point "c" (kh=5.132426,ω/N=0.4780914) with its second harmonic at "C". In the former case the interaction is (spatially) faster by a factor of about two, while in the latter case the relative amplitude of the resonant wave is higher. The most striking aspect of the solution is that the interaction is one-way. This can be seen from (3.5a) in which, because $\mathscr{A}_1^2$ is always positive, then $\mathrm{d}\mathscr{B}_2/dx_1$ can never change sign. As a result the magnitude of $\mathscr{B}_2$ can only increase (the sign of α only contributes to 0 or π radian

phase shift to the wave), and that's why the direction of energy can never change. This is in contrast to typical triad resonance interactions (e.g. McComas and Bretherton, 1977; Alam et al., 2010; Alam, 2012a) and harmonic generation in shallow water waves (e.g. Alam and Mei, 2007) where energy initially flows from original waves to resonant waves, but then when the amplitude of resonant waves is large enough the flow of energy reverses. Here, energy only goes from the original wave to the second harmonic and stays there permanently. The original wave will be gone forever.

Our multiple scales results conserve energy, as expected. In figure 3.3c (which corresponds to the case presented in figure 3.3b) we plot the energy flux ($E_f = E \times C_g$ where E is the energy per unit horizontal area and C_g is the group velocity) normalized by the energy flux of the original wave at the beginning ($E_{f,\mathscr{A}_{10}}$). Plotted are the normalized energy flux of the original wave $E_{f,\mathscr{A}_1}$ (blue-dashed line), the second harmonic $E_{f,\mathscr{B}_2}$, and the summation of the fluxes $E_{f,total} = E_{f,\mathscr{A}_1} + E_{f,\mathscr{B}_2}$. As expected from the conservation of energy the latter is constant and equal to unity.

To cross validate our results with direct simulation, we use the adaptive Navier-Stokes solver code SUNTANS (Stanford Unstructured Nonhydrostatic Terrain-following Adaptive Navier-Stokes Simulator (Fringer et al., 2006)). As a nonhydrostatic parallel ocean model with the capability to implement a nonlinear free surface, SUNTANS has been validated and widely used in studying internal waves (and associated turbulence and mixing) in stratified waters (Zhang et al., 2011; Kang and Fringer, 2010; Wang et al., 2011; Kang and Fringer, 2012; Walter et al., 2012; Zhang et al., 2011; Wang et al., 2011).

Here we consider propagation of waves in a stratified water of density gradient $a = 1 \times 10^{-3}$ m^{-1} (i.e., $N = 0.1$ rad/s), depth 100m and in a domain of horizontal extent 20km. We choose 5×10^3 grid points in the x direction and 100 layers in the z direction. We specify the velocity of fluid particles at the left boundary to match that of desired incoming wave. Therefore the left boundary that serves as the incoming wave boundary (wave maker). The right boundary is closed and a slip-free boundary condition is applied. We consider the case of an incident internal wave of mode 2 (kh=3.147946, ω/N=0.4472136, vertical velocity amplitude w=0.1m/s) with its second harmonic being a mode 1 wave. The time step $\delta t/T$=1/35000 where T is the period of the incident wave. We run the simulation until the incident wave arrives at the wall, at which point the amplitude of both waves (incident and its second harmonics) have reached a steady state in the domain of interest $0 < x/\lambda_i < 20$. As is seen from figure 3.4, the curve of $\mathscr{B}_2/\mathscr{A}_{10}$ vs x/λ_1 gives an initial slope of 0.0107 which is the same as our theoretical prediction (3.5).

To see how fast this instability evolves temporally, we present in figure 3.5 results of the temporal evolution of the parent wave and its second harmonic, with the same physical parameters as in the case in figure 3.3a. The governing equation takes a similar form to (3.5) except the derivatives that are with respect to the time t and clearly expressions for α and β are different. The qualitative trend is as the spatial case, and the figure suggests that we need time $\sim \mathscr{O}(1000)$ times the period of the initial wave to see the majority of the energy transmitted to the second harmonic. With the chosen Brunt-Väisälä frequency of $N = 0.022\mathrm{s}^{-1}$ (correspondingly, the wave number is $k = 3.14 \times 10^{-3}\mathrm{m}^{-1}$, the frequency is

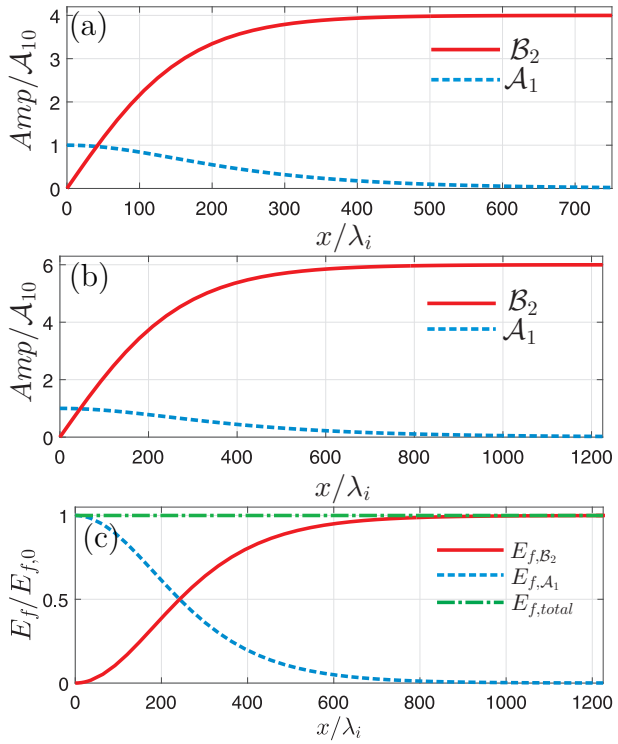


Figure 3.3: Spatial evolution of the amplitude of the original wave (blue dashed line) and its resonant second harmonic (red solid line) corresponding to the point "a" in figure 3.1 (kh=3.144772, ω/N=0.4472136, aA_{10}/N=0.0023, fig. a), and the point "c" in figure 3.1 (kh=5.132426, ω/N=0.4780914, aA_{10}/N=0.0023, fig. b). In figure (a) energy goes from mode 2 to mode 1, whereas in figure (b) energy goes from mode 3 to mode 1. Figure (c) shows the energy flux of each wave as well as the sum of the energy fluxes (green dash-dotted line) in case (b). As expected from energy conservation, the overall energy flux is unchanged in the domain of interaction.

$9.90\times10^{-3}\mathrm{s}^{-1}$, the wave amplitude is 1m, the water depth is 1000m and $a=5\times10^{-5}\mathrm{m}^{-1}$), the time scale is about 10 days, which is of the same order as that of parametric subharmonic instability of the M2 internal tide ($\sim$ 2-5 days) (c.f. e.g. Gerkema et al., 2006; MacKinnon and Winters, 2005). This is somewhat expected as both mechanisms are second-order resonance instabilities. Similar to the spacial case, the governing equation is,

$$\frac{\mathrm{d}\mathscr{B}_2(t_1)}{\mathrm{d}t} = \alpha_t \mathscr{A}_1^2(t_1), \tag{3.6a}$$

$$\frac{\mathrm{d}\mathscr{A}_1(t_1)}{\mathrm{d}t} = \beta_t \mathscr{A}_1(t_1)\mathscr{B}_2(t_1), \tag{3.6b}$$

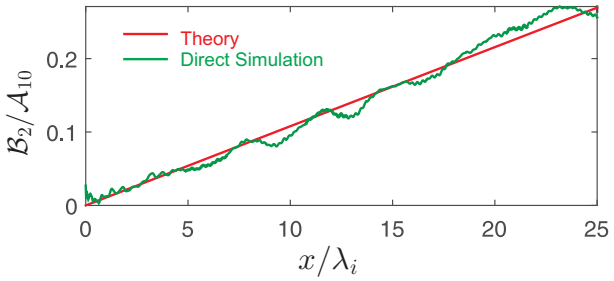


Figure 3.4: Comparison of analytical results (3.5) with the direct simulation. The physical parameters used are: density gradient $a = 1 \times 10^{-3}\ m^{-1}$, water depth $h = 100$m, dimensionless wave number kh=3.147946, dimensionless frequency ω/N=0.4472136, the amplitude of vertical velocity of the incident wave A_{10}=0.1 m/s.

where,

$$\alpha_t = -\frac{3\omega^2 m_1^2 m_2^2 \cos m_2 h}{gk^2[m_2^3 h + 4m_2 hk^2 + (m_2^2 - 4k^2)\sin m_2 h \cos m_2 h]},$$

$$\beta_t = -\frac{m_1 \sin m_2 h[(3m_1^2 + m_2^2 + 3k^2)\cos^2 m_1 h - 2m_1 m_2 \cot m_2 h \sin 2m_1 h - (2m_1^2 + m_2^2 + 3k^2)]}{2[2m_1^3 h + 2m_1 hk^2 + (m_1^2 - k^2)\sin 2m_1 h]}.$$

The analytical solutions to (3.6) read,

$$\mathscr{A}_1 = A_{10}\ \mathrm{sech}(A_{10}\sqrt{-\alpha_t\beta_t}\,t), \tag{3.7a}$$

$$\mathscr{B}_2 = -\frac{A_{10}\sqrt{-\alpha_t\beta_t}\tanh(A_{10}\sqrt{-\alpha_t\beta_t}\,t)}{\beta_t}, \tag{3.7b}$$

where $A_{10} = \mathscr{A}_1(t=0)$. For instance, the time it takes for $\mathscr{A}_1$ to lose 95% of the original amplitude is $\frac{3.69}{A_{10}\sqrt{-\alpha_t\beta_t}}$ seconds. That is, the time scale for $\mathscr{A}_1$ to decay is inversely proportional to the initial wave amplitude. Given an initial wave amplitude, in figure 3.6 we plot the dependence of the decay rate $R = \sqrt{-\alpha_t\beta_t}$ (although physically $A_{10}\sqrt{-\alpha_t\beta_t}$ represents the actual decay rate) on mode numbers n and the horizontal wave numbers. It can be seen that starting from the reference point (where the largest decay rate is obtained) the decay rate decreases as mode number and horizontal wave numbers increase.

We would like to comment here that Parametric Subharmonic Instability is dependent upon perturbation waves in the domain in order to get started (Davis and Acrivos, 1967; Muller, 1986). For a monochromatic standing wave that is not an exact solution to the fully nonlinear governing equation, for PSI to occur, perturbations are still required since otherwise no subharmonic waves would be excited (see e.g. page 436 McEwan, 1971). In direct simulations, this is achieved by adding random noise to the simulation domain. In experimental studies the required noise already exists in the domain due to unavoidable imperfections. Hence, usually in experiments Parametric Subharmonic Instability is automatically obtained

(similar to inevitable Benjamin-Feir instability) and destabilizes "single" internal waves to a number of other subharmonic waves (e.g. Martin et al., 1972). We would like to emphasize that the underlying mechanism of resonant harmonic generation studied here is different than that of Parametric Subharmonic Instability in that the former mechanism, among other characteristics, is an "inherent" instability that does not require ambient perturbations to get started.

Three snapshots of the overall vertical velocity w are shown in figure 3.5b that highlights the horizontal and vertical structures of the wave field at different times. Energy goes from the original internal wave (b1) slowly to its higher harmonics, first leading to modulation of the original wave (b2), but eventually the entire energy is at the second harmonic (b3) whose frequency and horizontal wavenumber are double the horizontal frequency and wavenumber of the initial wave. The interaction is only between the initial wave and its second harmonic, and no cascading to different waves is ensued.

We would like to note that the harmonic generation mechanism proposed here occurs for non-uniformly stratified ocean as well. As pointed out previously, a necessary condition for this to occur is that for a given wave of frequency ω and wavenumber k, the two conditions $\mathscr{D}(k,\omega)=0$ and $\mathscr{D}(2k,2\omega)=0$ are satisfied. We present two examples in figure 3.7 for two different density profiles: parabolic $\rho(z)=\rho_0(1+az^2)$, where $a=1\times10^{-5}\mathrm{m}^{-2}$ (figure 3.7a), and exponential $\rho(z)=\rho_0[1+\delta-\delta\exp(az)]$, where $a=0.1\mathrm{m}^{-1},\delta=0.1$ (figure 3.7b). The water depth is 100 m for both. The Brunt-Väisälä frequencies increase with depth in one case and decrease in the other. It can been seen from figure 3.7 that there are, as well, infinitely countable intersections (i.e., solutions) between the two sets of curves. In these cases, contrary to the constant N case, the linear wave solution does not satisfy the nonlinear Boussinesq-Euler equation and hence inclusion of the nonlinear free surface condition is not necessary for the harmonic generation to appear. The analysis for these two cases can be carried out by following the same logic presented in the appendix, although mathematically more involved and closed-form explicit solutions will be tedious, if not impossible, to obtain.

As discussed above, when density profile is not uniform and hence N is not constant, two sources contribute to the harmonic generation: 1- nonlinearities in the free surface boundary condition, i.e. right-hand side of equation (3.20b), and 2- nonlinear terms in the momentum equation, i.e. right-hand side of equation (3.20a). As presented before, for a constant N case the latter source is absent. For nonuniform stratifications, it is of interest to evaluate the relative importance of these two contributors. The motivation is to see whether the classical rigid-lid assumption would be a good approximation in estimating energy exchange due to harmonic generation when the density profile is non-uniform.

We comment on this question briefly by considering the exponential density profile as it is representative of actual pycnoclines. For such a density profile, the vertical structure of an internal wave $W(z)$ is obtained as

$$W(z)=-\frac{J_\nu(\mu)Y_\nu(p)-Y_\nu(\mu)J_\nu(p)}{Y_\nu(\mu)} \tag{3.8}$$

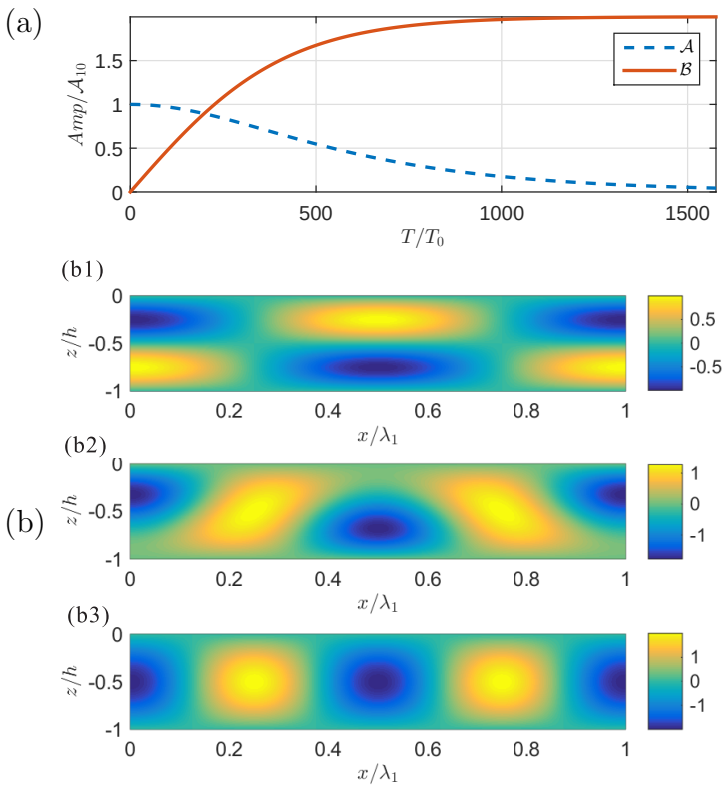


Figure 3.5: Time evolution of the vertical velocities of internal gravity waves that satisfy the conditions of harmonic generation. The physical parameters used here correspond to figure 3.3a. (a) Time evolution of the amplitudes of the two waves. T_0 is the period of the parent wave. (b) Snapshots of the wave field at $t = 0$ (b1), $t = 500T_0$ (b2), and $1500T_0$(b3). The presented mechanism initially results in a modulation of the primary wave, and eventually all the energy goes to the second harmonic.

where, J and Y are Bessel function of the first and the second kind respectively, and

$$\nu = \frac{2k}{a}, \quad \mu = \frac{2k\sqrt{g\delta}e^{-1/2ah}}{\omega\sqrt{a}}, \quad p = \frac{2k\sqrt{g\delta}e^{1/2az}}{\omega\sqrt{a}}. \tag{3.9}$$

By substituting this equation into the right-hand side of equations (3.20a) and (3.20b) the relative importance of the right-hand side of the two equations are obtained.
We consider a wave with the wave number and frequency $kh = 14.14$ and $\omega/N_{\max} = 0.30$ corresponding to the point highlighted by the character "A" in figure 3.7(b). Averaged over the z direction, the relative magnitude of nonlinear terms on the right-hand side of the Boussinesq-Euler equation to those of free surface boundary condition (i.e. (3.20a) to (3.20b)) is only about 5%. This stresses that even in the case of a nonlinear density stratification, the contribution of nonlinear free surface terms is still much higher (here more than an order of

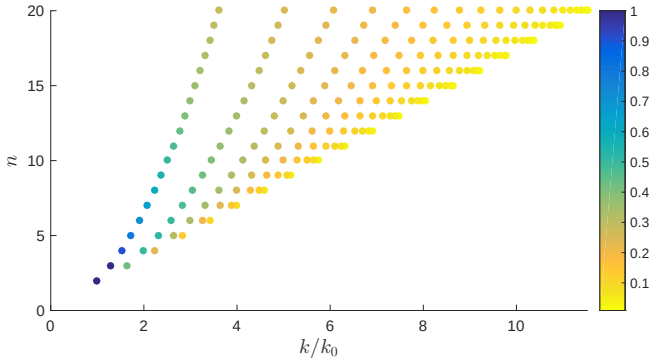


Figure 3.6: Dependence of the decay rate $R = \sqrt{-\alpha_t \beta_t}$ on mode numbers n and the horizontal wave numbers. We normalize the quantities by the wave where the largest decay rate is obtained (here it corresponds to point "a" in figure 3.1). Color scale represents R/R_0 where $R_0 = 3.81 \times 10^{-6}\mathrm{m}^{-1}$. The physical parameters used here are the same as in figure 3.1.

magnitude) than those arising from the nonlinearity of the density profile. It is to be noted that in the nonlinear cases studied in figure 3.7, Brunt-Väisälä frequencies are significantly different from the linear case. Specifically, in both nonlinear cases, N reaches zero whereas in the linear case N is constant. Clearly the effect of a nonlinear density profile is increased as the profile departs further from a linear one.

We also would like to emphasize that the resonant harmonic generation studied here is different from non-resonant harmonic generation that occurs in non-uniform stratifications (e.g. Sutherland, 2016). The former occurs for specific internal waves, transfers the entire energy to the second harmonic and is a one-way process, whereas the latter obtains for all internal waves but since it is non-resonant only transfers a portion of energy from the initial wave to the superharmonics.

We also would like to note that non-Boussinesq effects (and corresponding terms in the governing equation) can also lead to the generation of resonant super harmonics. In other words, harmonic generation can be obtained in uniform stratification with the rigid lid, if non-Boussinesq terms are not neglected. However, as will be shown shortly, the relative importance of such routing of energy is orders of magnitude less than that of nonlinear free surface avenue: Following the same procedure for getting (3.14), except not making Boussinesq approximation, we obtain,

$$\begin{aligned}
&\rho \frac{\partial}{\partial t}\nabla^2 w + \rho \nabla_H^2(\vec{\mathbf{u}}\cdot\nabla w) - \rho \frac{\partial^2}{\partial x \partial z}(\vec{\mathbf{u}}\cdot\nabla u) - \rho \frac{\partial^2}{\partial y \partial z}(\vec{\mathbf{u}}\cdot\nabla v) + g\nabla_H^2 \rho \\
&+ 2\nabla\rho\cdot\nabla\frac{\partial w}{\partial t} + \frac{\partial w}{\partial t}\nabla^2\rho + 2\nabla\rho\cdot\nabla(\vec{\mathbf{u}}\cdot\nabla w) + \nabla^2\rho\cdot(\vec{\mathbf{u}}\cdot\nabla w) - \frac{\partial}{\partial z}(\frac{\partial \vec{\mathbf{u}}}{\partial t}\cdot\nabla\rho) \\
&- \frac{\partial}{\partial z}[\nabla\rho\cdot(\vec{\mathbf{u}}\cdot\nabla\vec{\mathbf{u}})] - \frac{\partial}{\partial z}(\frac{\partial \vec{\mathbf{u}}}{\partial t}\cdot\nabla\rho) = 0. \qquad (3.10)
\end{aligned}$$

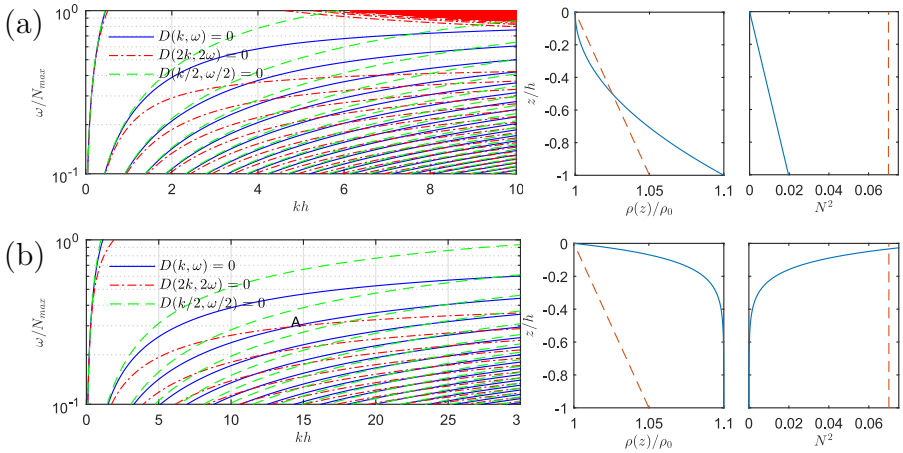


Figure 3.7: Plots of $\mathscr{D}(k,\omega)=0$, $\mathscr{D}(2k,2\omega)=0$ and $\mathscr{D}(k/2,\omega/2)=0$ for parabolic and exponential density profiles (c.f. figure 3.1): (a) for $\rho(z)=\rho_0(1+az^2)$ with $a=1\times10^{-5}\mathrm{m}^{-2}$ and (b) for $\rho(z)=\rho_0[1+\delta-\delta\exp(az)]$ with $a=0.1\mathrm{m}^{-1}$ and $\delta=0.1$. On the right-side of each plot, we show the normalized density profile $\rho(z)/\rho_0$ and the Brunt-Väisälä frequency $N(z)^2$ of the two nonlinear density profiles (blue solid lines) overlaid of top of corresponding plots of linear density profile (red dashed lines). Water depth is $h=100\mathrm{m}$.

Comparing the Boussinesq terms in the above equation and the quadratic terms on the free surface boundary condition, i.e., (3.19), we find that their ratio is order of a/k. For the two cases presented above, the ratios are less than 1.6%.

The harmonic generation through a nonlinear free surface involves two energy transfer processes simultaneously, in one process (k,ω) wave loses energy to $(2k,2\omega)$ wave and generates the second harmonic; in the other the $(2k,2\omega)$ wave forms a triad resonance with (k,ω) wave and sends energy back in an opposite way. The triad resonance condition is clearly satisfied since $2\omega-\omega=\omega$ and $2k-k=k$. If at the initial moment we only have (k,ω) wave (i.e. no second harmonic in the domain) then harmonic generation triumphs over triad resonance in transferring energy, resulting in the combined effect that energy only goes in one direction. But it can be shown that there are initial conditions under which the energy at first goes from $(2k,2\omega)$ wave to the (k,ω) wave, but even in that case eventually the entire energy is transferred to the $(2k,2\omega)$ wave. This can be shown rigorously through Lyapunov stability theorem. Basically, the objective is to prove that $\mathscr{A}_1=0$ and $\mathscr{B}_2$ reaching its maximum is the asymptotically stable solution of the dynamical system described by equation (3.5).
To prove this, we first note that (3.5) can be put in the following form

$$\frac{\mathrm{d}}{\mathrm{d}x}\left(\mathscr{B}_2^2-\frac{\alpha}{\beta}\mathscr{A}_1^2\right)=0. \tag{3.11}$$

Therefore, since $\frac{\alpha}{\beta}$ can be shown to be always negative(see Appendix B), we have

$$\mathscr{B}_2^2 - \frac{\alpha}{\beta}\mathscr{A}_1^2 = \mathscr{G}^2, \tag{3.12}$$

where $\mathscr{G}$ is a constant that is determined by the initial conditions. Equation (3.12) shows that $(\mathscr{A}_1, \mathscr{B}_2)$ are always moving on an ellipse. If we define a Lyapunov function $V(\mathscr{A}_1) = \mathscr{G} - \alpha/|\alpha|[\int_0^x \alpha \mathscr{A}_1(x)^2 dx + \mathscr{B}_2(0)]$, we find that $V(\mathscr{A}_1) \geqslant 0$ and $dV/dx < 0$. According to Lyapunov asymptotic stability theorem, the solution of the system converges to $\mathscr{A}_1 = 0$ from any starting points as x goes to ∞.

3.4 Conclusion

Here we reported that certain internal gravity waves are inherently unstable and are not able to sustain their form. This new instability mechanism, a result of resonant harmonic-generation, draws the energy of an internal wave and hands it over to its second (or generally higher) harmonic. This resonance is distinguished from the classical triad resonance (and associated subharmonic instability) in that 1- a single wave may undergo the instability without requiring any external perturbation, and 2- the transfer of energy is irreversible and the original wave permanently loses its energy to its second harmonic. Extension of the results presented here to the third and higher harmonic generation is straightforward, but the strength of energy exchange in higher harmonics is much weaker.

Appendix

3.A Derivation of the Interaction Equation

Consider the propagation of waves in an inviscid, incompressible, adiabatic and stably stratified fluid of density $\rho(x,y,z,t)$, bounded by a free surface on the top and a rigid seafloor with a depth h at the bottom. We consider a Cartesian coordinate system with x,y-axes on the mean free surface and z-axis positive upward. Equations governing the evolution of the velocity vector $\mathbf{u} = \{u,v,w\}$, density ρ, pressure p and surface elevation η under Boussinesq

approximation read

$$\rho_0 \frac{D\mathbf{u}}{Dt} = -\nabla p - \rho g \nabla z, \quad -h < z < \eta \tag{3.13a}$$

$$\frac{D\rho}{Dt} = 0, \quad -h < z < \eta \tag{3.13b}$$

$$\nabla \cdot \mathbf{u} = 0, \quad -h < z < \eta \tag{3.13c}$$

$$\eta_t = \mathbf{u} \cdot \nabla (z - \eta), \quad z = \eta \tag{3.13d}$$

$$\frac{Dp}{Dt} = 0, \quad z = \eta \tag{3.13e}$$

$$w = 0, \quad z = -h, \tag{3.13f}$$

where g is the gravitational acceleration, and $\rho_0 = \bar{\rho}(z=0)$ is the mean density on the free surface with $\bar{\rho}(z)$ the background (unperturbed) density such that $\rho = \bar{\rho}(z) + \rho'(x,y,z,t)$. Equation (3.13a) is the momentum equation, (3.13b) comes from conservation of salt in the absence of diffusion, mixing, sources and sinks, and (3.13c) is continuity equation that together form five equations for five unknown variables of the problem (three components of velocity $\mathbf{u}$, pressure p and density ρ). Equations (3.13d)-(3.13f) are boundary conditions on the free surface and the bottom.

Similar to the density perturbation ρ', we define a pressure perturbation p' via $p = \bar{p}(z) + p'(x,y,z,t)$ such that $d\bar{p}(z)/dz = -\bar{\rho}(z)g$. For the linear terms of the governing equation (3.13a) to be only in terms of w we calculate $\partial/\partial z[\nabla \cdot (3.13a)] - \nabla^2 (3.13a)_3$, where $(3.13a)_3$ denotes the z component of (3.13a)(likewise, 1,2 for x,y will be used later). We obtain

$$\frac{\partial}{\partial t}\nabla^2 w - \frac{\partial^2}{\partial x \partial z}\mathbf{u} \cdot \nabla u - \frac{\partial^2}{\partial y \partial z}\mathbf{u} \cdot \nabla v + \nabla_H^2 (\mathbf{u} \cdot \nabla w) + \frac{g}{\rho_0}\nabla_H^2 \ \rho' = 0, \tag{3.14}$$

where $\nabla_H^2 = \partial^2/\partial x^2 + \partial^2/\partial y^2$ is the horizontal Laplacian. Taking the time derivative of (3.14) and substituting ρ' from the expansion of (3.13b), i.e.,

$$\frac{\partial \rho'}{\partial t} + \mathbf{u} \cdot \nabla \rho' + w \frac{d\bar{\rho}(z)}{dz} = 0. \tag{3.15}$$

and denoting $N^2 = -g/\rho_0 \mathrm{d}\bar{\rho}(z)/\mathrm{d}z$ as the Brunt-Väisälä frequency, we obtain

$$\frac{\partial^2}{\partial t^2}\nabla^2 w + N^2 \nabla_H^2 w = \frac{\partial^3}{\partial x \partial z \partial t}\mathbf{u} \cdot \nabla u + \frac{\partial^3}{\partial y \partial z \partial t}\mathbf{u} \cdot \nabla v - \nabla_H^2 \frac{\partial}{\partial t}(\mathbf{u} \cdot \nabla w) + \frac{g}{\rho_0}\nabla_H^2 (\mathbf{u} \cdot \nabla \rho'). \tag{3.16}$$

Expanding the surface dynamic boundary condition (3.13e) and keeping terms up to the second order we obtain

$$\frac{\partial p'}{\partial t} = w\rho_0 g - \mathbf{u} \cdot \nabla p' - \frac{\partial^2 p'}{\partial z \partial t}\eta + \rho_0 g \eta \frac{\partial w}{\partial z} + g\eta w \frac{\mathrm{d}\bar{\rho}}{\mathrm{d}z}, \quad z = 0. \tag{3.17}$$

where the last term can be equivalently written as $-N^2\bar{\rho}_0\eta w$. Here p' can be substituted from an expression obtained from taking the x derivative of $(3.13a)_1$ added to the y derivative of $(3.13a)_2$ and taking the time derivative:

$$-\frac{\partial^3 w}{\partial z\partial t^2}+\frac{1}{\rho_0}\nabla_H^2\frac{\partial p'}{\partial t}+\frac{\partial^2}{\partial x\partial t}\mathbf{u}\cdot\nabla u+\frac{\partial^2}{\partial y\partial t}\mathbf{u}\cdot\nabla v=0. \tag{3.18}$$

Substituting $\partial p'/\partial t$ from (3.18) in (3.17) we obtain

$$\begin{aligned}\frac{\partial^3 w}{\partial z\partial t^2}-g\nabla_H^2 w=&\frac{\partial^2}{\partial x\partial t}\mathbf{u}\cdot\nabla u+\frac{\partial^2}{\partial y\partial t}\mathbf{u}\cdot\nabla v\\&+\nabla_H^2\left(g\frac{dw}{dz}\eta+N^2w\eta\right)-\frac{1}{\rho_0}\nabla_H^2\left(\mathbf{u}\cdot\nabla p'+\frac{\partial^2 p'}{\partial z\partial t}\eta\right).\end{aligned} \tag{3.19}$$

Therefore the governing equation and boundary conditions correct to $\mathscr{O}(\varepsilon^2)$ where ε is a measure of the wave steepness, reduce to (3.16), (3.19) and (3.13f). For the ease of reference, we rewrite these equations here:

$$\begin{aligned}\frac{\partial^2}{\partial t^2}\nabla^2 w+N^2\nabla_H^2 w=&\frac{\partial^3}{\partial x\partial z\partial t}\mathbf{u}\cdot\nabla u+\frac{\partial^3}{\partial y\partial z\partial t}\mathbf{u}\cdot\nabla v-\frac{\partial^3}{\partial x^2\partial t}\mathbf{u}\cdot\nabla w\\&-\frac{\partial^3}{\partial y^2\partial t}\mathbf{u}\cdot\nabla w+\frac{g}{\rho_0}\nabla_H^2\left(\mathbf{u}\cdot\nabla\rho'\right)\qquad -h<z<0,\end{aligned} \tag{3.20a}$$

$$\begin{aligned}\frac{\partial^3 w}{\partial z\partial t^2}-g\nabla_H^2 w=&\frac{\partial^2}{\partial x\partial t}\mathbf{u}\cdot\nabla u+\frac{\partial^2}{\partial y\partial t}\mathbf{u}\cdot\nabla v+\nabla_H^2\left(g\frac{dw}{dz}\eta+N^2w\eta\right)\\&-\frac{1}{\rho_0}\nabla_H^2\left(\mathbf{u}\cdot\nabla p'+\frac{\partial^2 p'}{\partial z\partial t}\eta\right)\qquad z=0,\end{aligned} \tag{3.20b}$$

$$w=0,\quad z=-h. \tag{3.20c}$$

Equations (3.20a) and (3.20b) are equivalent to equations (A2) and (A7) of Thorpe (1966)[1]. To perform a weakly nonlinear analysis, we assume that internal waves in the system described above are small perturbations from the mean state of water at rest, i.e. $\mathbf{u},\rho',p'\sim\mathscr{O}(\varepsilon)$. Considering the two-dimensional problem and assuming that the solution to this problem can be expressed in terms of a convergent series we define

$$w(x,x_1,z,t)=\varepsilon w_1(x,x_1,z,t)+\varepsilon^2 w_2(x,x_1,z,t)+\mathscr{O}(\varepsilon^3) \tag{3.21}$$

where $x_1=\varepsilon x$ is the slow spatial variable and $\varepsilon\ll 1$ is a measure of steepness of the waves and $w_i\sim\mathscr{O}(1)$. Similar expressions exist for other variables, i.e. $u=\varepsilon u_1+\varepsilon^2 u_2+\mathscr{O}(\varepsilon^3)$,

[1]except that we found three typos there: (1) for $S1$ in (A2), the sign of the last term with g should be positive; (2) for $S3$ in (A7), the first term should be $\boldsymbol{\omega}\cdot\nabla w$; and (3) the term $g\nabla_1^2\frac{\partial}{\partial x}(\eta w_z)$ is missing. These are clearly typos as they do not appear in later expressions of Thorpe (1966).

$\rho' = \varepsilon\rho_1' + \varepsilon^2\rho_2' + \mathscr{O}(\varepsilon^3)$, $p' = \varepsilon p_1' + \varepsilon^2 p_2' + \mathscr{O}(\varepsilon^3)$ and $\eta = \varepsilon\eta_1 + \varepsilon^2\eta_2 + \mathscr{O}(\varepsilon^3)$ with $u_i, \rho_i', p_i' \sim \mathscr{O}(1)$ being functions of x, x_1, z, t, and $\eta_i \sim \mathscr{O}(1)$ being functions of x, x_1 and t.
Upon substitution into the governing equation, at the leading order $\mathscr{O}(\varepsilon)$ we obtain

$$\frac{\partial^2}{\partial t^2}\nabla^2 w_1 + N^2\nabla_H^2 w_1 = 0 \qquad -h < z < 0, \tag{3.22a}$$

$$\frac{\partial^3 w_1}{\partial z \partial t^2} - g\nabla_H^2 w_1 = 0 \qquad z = 0, \tag{3.22b}$$

$$w_1 = 0, \qquad z = -h. \tag{3.22c}$$

At the second order $\mathscr{O}(\varepsilon^2)$ we have

$$\begin{aligned}\frac{\partial^2}{\partial t^2}\nabla^2 w_2 + N^2\nabla_H^2 w_2 =& -2\left(\frac{\partial^2}{\partial t^2} + N^2\right)\frac{\partial^2}{\partial x \partial x_1} w_1 + \frac{\partial^3}{\partial x \partial z \partial t}\mathbf{u}_1 \cdot \nabla u_1 \\ &+ \frac{\partial^3}{\partial y \partial z \partial t}\mathbf{u}_1 \cdot \nabla v_1 - \frac{\partial^3}{\partial x^2 \partial t}\mathbf{u}_1 \cdot \nabla w_1 - \frac{\partial^3}{\partial y^2 \partial t}\mathbf{u}_1 \cdot \nabla w_1 \\ &+ \frac{g}{\rho_0}\nabla_H^2(\mathbf{u}_1 \cdot \nabla \rho_1'), \qquad -h \le z \le 0.\end{aligned} \tag{3.23a}$$

$$\begin{aligned}\frac{\partial^3 w_2}{\partial z \partial t^2} - g\nabla_H^2 w_2 =& 2g\frac{\partial^2 w_1}{\partial x \partial x 1} + \frac{\partial^2}{\partial x \partial t}\mathbf{u}_1 \cdot \nabla u_1 + \frac{\partial^2}{\partial y \partial t}\mathbf{u}_1 \cdot \nabla v_1 \\ &+ \nabla_H^2\left(g\frac{dw_1}{dz}\eta_1 + N^2 w_1 \eta_1\right) \\ &- \frac{1}{\rho_0}\nabla_H^2\left(\mathbf{u}_1 \cdot \nabla p_1' + \frac{\partial^2 p_1'}{\partial z \partial t}\eta_1\right), \qquad z = 0.\end{aligned} \tag{3.23b}$$

$$w_2 = 0, \qquad z = -h. \tag{3.23c}$$

We now assume that waves with wavenumber and frequency (k, ω) and $(2k, 2\omega)$ satisfy the internal waves dispersion relation (which is obtained from the linear equation (3.22))

$$\mathscr{D}(k, \omega) = \omega^2 - \frac{gk}{\sqrt{ga/\omega^2 - 1}}\tan\left(kh\sqrt{ga/\omega^2 - 1}\right), \tag{3.24}$$

i.e. $\mathscr{D}(k, \omega) = 0$ and $\mathscr{D}(2k, 2\omega) = 0$, and that they both exist in our domain of interest, though potentially with different amplitudes. The propagating wave solution to the linear equation (3.22) then obtains as

$$\begin{aligned}w_1(x, x_1, z, t) =& A_1(x_1)\sin m_1(z+h)\sin(kx - \omega t) + B_1(x_1)\sin m_1(z+h)\cos(kx - \omega t) \\ &+ A_2(x_1)\sin m_2(z+h)\sin(2kx - 2\omega t) + B_2(x_1)\sin m_2(z+h)\cos(2kx - 2\omega t)\end{aligned} \tag{3.25a}$$

in which A_1, A_2, B_1, B_2 are amplitudes of each wave, $m_1^2 = k^2(N^2 - \omega^2)/\omega^2$ and $m_2^2 = k^2(N^2 - 4\omega^2)/\omega^2$. Other variables u, ρ', p' and η can be found respectively via continuity equation

(3.13c), energy equation (3.13b), kinematic surface boundary condition (3.13d) and the dynamic free surface boundary condition (3.13f).

The left-hand side of the second order equation (3.23) is identical in the form to the first order equation (3.22), but the right hand side of (3.23) is clearly non-zero and is a nonlinear function of the leading order solution $u_1, \rho_1', p_1', \eta_1$. It turns out, after substitution, that the right hand side contains terms with harmonics which are the same as the harmonics of the leading order equation (secular terms). A compatibility condition then must be enforced to make sure that the solution does not go unbounded, which is clearly unphysical. This compatibility condition determines the spatial behavior of the coefficients A_i, B_i.

While the formulation presented here is general, our primary interest is when an initial wave with wavenumber and frequency (k, ω) resonates with its second harmonic $(2k, 2\omega)$ whose initial amplitude is zero. Therefore in the following we use the adjectives original and resonant waves to refer to (k, ω) and $(2k, 2\omega)$ waves respectively. We would like to emphasize that the formulation is general and works for any initial condition of the two waves. We will also comment that the presented approach can be easily extended to third and higher-harmonic generation.

Without loss of generality we assume that $B_1 = 0$, which only has to do with our choice of coordinate system. But we keep A_2 and B_2, since they determine the phase of the resonant wave $(2k, 2\omega)$ with respect to the original wave (k, ω). The general solution to the second order problem takes the form

$$\begin{aligned} w_2(x, x_1, z, t) =& C_{11}(x_1, z)\sin(kx - \omega t) \quad + C_{12}(x_1, z)\cos(kx - \omega t) && \text{(3.26a)} \\ &+ C_{21}(x_1, z)\sin(2kx - 2\omega t) + C_{22}(x_1, z)\cos(2kx - 2\omega t) && \text{(3.26b)} \end{aligned}$$

where $C_{ij}(x_1, z)$'s are to be determined from (3.23). Substituting (3.26) and (3.25) into (3.23), and collecting same sine and cosine terms we obtain four ordinary differential equations for C_{ij} $(i, j$=1,2):

$$\begin{aligned} -\omega^2 C_{1i,zz} - m_1^2 \omega^2 C_{1i} &= E_{1i}, & -h < z < 0, && \text{(3.27a)} \\ -\omega^2 C_{1i,z} + gk^2 C_{1i} &= F_{1i}, & z = 0, && \text{(3.27b)} \\ C_{1i} &= 0, & z = -h, && \text{(3.27c)} \end{aligned}$$

$$\begin{aligned} -4\omega^2 C_{2i,zz} - 4m_2^2 \omega^2 C_{2i} &= E_{2i}, & -h < z < 0, && \text{(3.28a)} \\ -4\omega^2 C_{2i,z} + 4gk^2 C_{2i} &= F_{2i}, & z = 0, && \text{(3.28b)} \\ C_{2i} &= 0, & z = -h, && \text{(3.28c)} \end{aligned}$$

where E_{i1}, F_{i1} are the coefficients of $\sin(ikx - i\omega t)$, and E_{i2}, F_{i2} are the coefficients of $\cos(ikx - i\omega t)$ in the right-hand side of (3.23a) and (3.23b) respectively. Let's first consider the equation for C_{22}, we obtain

$$E_{22} = -\frac{4\omega^2 m_2^2}{k}\sin m_2(z+h)\frac{\mathrm{d}A_2(x_1)}{\mathrm{d}x_1}, \qquad F_{22} = 4gk\sin m_2 h\frac{\mathrm{d}A_2(x_1)}{\mathrm{d}x_1}, \tag{3.29}$$

for which the solution to (3.28a) that satisfies the boundary condition (3.28c) is

$$C_{22}(x_1,z) = -\frac{m_2}{2k}(z+h)\cos m_2(z+h)\frac{\mathrm{d}A_2(x_1)}{\mathrm{d}x_1}. \tag{3.30}$$

Upon substitution into (3.28b) we obtain

$$gk\left(\frac{2m_2h+\sin 2m_2h}{\cos m_2h}\right)\frac{\mathrm{d}A_2(x_1)}{\mathrm{d}x_1} = 0, \tag{3.31}$$

therefore, since the coefficient is nonzero then $\mathrm{d}A_2/\mathrm{d}x_1 \equiv 0$. Physically speaking, this expression says that the amplitude A_2 does not change as waves propagate, or in other words, A_2 does not take part in the energy exchange. We, therefore, set A_2 equal to zero for the rest of the derivation. Physically, this means that the second harmonic must have a $\pi/2$ radian phase difference relative to the original wave.
We use the same approach as above for C_{21}. We have

$$E_{21} = \frac{4\omega^2m_2^2}{k}\sin m_2(z+h)\frac{\mathrm{d}B_2(x_1)}{\mathrm{d}x_1}, \tag{3.32a}$$

$$F_{21} = -4gk\sin m_2h\frac{\mathrm{d}B_2}{\mathrm{d}x_1} - 2\left(3\omega m^2 + \frac{N^2k^2}{\omega}\sin^2 m_1h\right)A_1^2(x_1), \tag{3.32b}$$

for which

$$C_{21}(x_1,z) = \frac{m_2}{2k}(z+h)\cos m_2(z+h)\frac{\mathrm{d}B_2(x_1)}{\mathrm{d}x_1}, \tag{3.33}$$

and upon substitution into (3.28b) we obtain

$$\frac{\mathrm{d}B_2(x_1)}{\mathrm{d}x_1} = \alpha A_1^2(x_1), \tag{3.34}$$

where

$$\alpha = -\frac{6m_1^2\omega\cos m_2h}{gk(2m_2h+\sin 2m_2h)}. \tag{3.35}$$

For $C_{11}(x_1,z)$, we obtain $E_{11} = F_{11} = 0$ and therefore the equation for $C_{11}(x_1,z)$ does not provide any extra information on $A_1(x_1)$ and $B_2(x_1)$. For C_{12} we obtain

$$\begin{aligned} E_{21} =& \frac{2m^2\omega^2}{k}\sin m_1(z+h)\frac{\mathrm{d}A_1(x_1)}{\mathrm{d}x_1} \\ &+ \left\{I^+\sin[(m_1+m_2)(z+h)] + I^-\sin[(m_1-m_2)(z+h)]\right\}A_1(x_1)B_2(x_1), \end{aligned} \tag{3.36}$$

$$F_{21} = 2gk\sin m_1(z+h)\frac{\mathrm{d}A_1(x_1)}{\mathrm{d}x_1} + JA_1(x_1)B_2(x_1), \tag{3.37}$$

where

$$I^+ = \frac{1}{8}\omega(m_2+2m_1)(m_2^2+3k^2-m_1^2) \tag{3.38a}$$

$$I^- = \frac{1}{8}\omega(2m_1-m_2)(m_1^2-3k^2-m_2^2) \tag{3.38b}$$

$$J = \frac{1}{4}\frac{gk^2\left(4m_1\cos^2 m_1h\ \sin m_2h - 2m_2\cos m_2h\ \sin 2m_1h - 3m_1\sin m_2h\right)}{\omega\cos m_1h}. \tag{3.38c}$$

We obtain

$$\begin{aligned} C_{12}(x_1,z) = &-\frac{m_1}{k}(z+h)\cos m_1(z+h)\frac{\mathrm{d}A_1(x_1)}{\mathrm{d}x_1} \\ &+\left\{\frac{I^+\sin[(m_1+m_2)(z+h)]}{\omega^2[m_1^2-(m_1+m_2)^2]}+\frac{I^-\sin[(m_1-m_2)(z+h)]}{\omega^2[m_1^2-(m_1-m_2)^2]}\right\}A_1(x_1)B_2(x_1). \end{aligned} \tag{3.39}$$

Substituting into (3.28b), we obtain

$$\frac{\mathrm{d}A_1(x_1)}{\mathrm{d}x_1} = \beta A_1(x_1)B_2(x_1), \tag{3.40}$$

where

$$\beta = -\frac{k[\sin m_2h(4m_1\cos^2 m_1h-3m_1)-2m_2\cos m_2h\sin 2m_1h]}{2\omega(2m_1h+\sin 2m_1h)}. \tag{3.41}$$

If we define the actual amplitudes $\mathscr{A}_1 = \varepsilon A_1$ and $\mathscr{B}_2 = \varepsilon B_2$ (note that $w = \varepsilon w_1 + \mathscr{O}(\varepsilon^2)$) then

$$\frac{\mathrm{d}\mathscr{B}_2}{\mathrm{d}x} = \alpha\mathscr{A}_1^2 \tag{3.42a}$$

$$\frac{\mathrm{d}\mathscr{A}_1}{\mathrm{d}x} = \beta\mathscr{A}_1\mathscr{B}_2, \tag{3.42b}$$

with the same α,β repeated here:

$$\alpha = -\frac{6m_1^2\omega\cos m_2h}{gk(2m_2h+\sin 2m_2h)},$$

$$\beta = -\frac{k[\sin m_2h(4m_1\cos^2 m_1h-3m_1)-2m_2\cos m_2h\sin 2m_1h]}{2\omega(2m_1h+\sin 2m_1h)}.$$

3.B Proof of the Sign of α/β

For the sign of α/β, we have

$$\mathrm{sign}(\frac{\alpha}{\beta}) = \mathrm{sign}\Big[\frac{\cos m_2h}{\sin m_2h(4m_1\cos^2 m_1h-3m_1)-2m_2\cos m_2h\sin 2m_1h}\Big]. \tag{3.44}$$

It is equivalent to the sign of

$$\tan m_2 h(4m_1 \cos^2 m_1 h - 3m_1) - 2m_2 \sin 2m_1 h. \tag{3.45}$$

Rearranging terms of the above expression gives,

$$\cos^2 m_1 h(4m_1 \tan m_2 h - 4m_2 \tan m_1 h) - 3m_1 \tan m_2 h, \tag{3.46}$$

After substitution of the dispersion relation,

$$\omega^2 = \frac{gk^2}{m_1} \tan m_1 h$$

and

$$\omega^2 = \frac{gk^2}{m_2} \tan m_2 h.$$

(3.46) can be simplified to

$$-3m_1 \tan m_2 h = -3m_1 m_2 \frac{\omega^2}{gk^2},$$

which is always less than zero.

Chapter 4

Energy Cascade of A Monochromatic Internal Gravity Wave from Vertical Reflecting Boundaries

In Chapter 3, we show that by taking into account a nonlinear free surface, there exists countably infinite number of internal waves that can lose their instability by harmonic generations (Liang et al., 2017). For such waves, at least one of their high harmonics satisfies dispersion relation. The energy of the parent internal wave is found to transfer to its high harmonic completely in an irreversible way. Although different in physics, this mechanism is governed by the same form of mathematical equations for harmonic generation of electromagnetic waves discovered more than half a century ago (Franken et al., 1961).

In the present study, we consider internal gravity waves with wave number k and fequency ω propagating to vertical reflecting boundaries, whose second harmonics satisfies the dispersion relation, i.e., $\mathscr{D}(2k, 2w) = 0$, where $\mathscr{D}(k, w) = 0$ is the dispersion relation. In comparison with the flow of an infinite domain presented in (Liang et al., 2017), here we consider a vertical wall boundary in the direction of wave propagation, to model the existence of steep continental slopes and ocean ridges. The parent internal wave (k, ω) will generate its second harmonic $(2k, 2\omega)$ due to the non-linearity in the momentum equation and the free surface boundary(Liang et al., 2017). Given the fact that at a fixed frequency the sequence of horizontal numbers of internal waves are approximately equal-spaced (see section II), upon wave reflections, the wave along with its second harmonic induces a $(3k, \omega)$ wave through the triad resonance mechanism, starting from which a series of triad resonances continuously form in the vicinity of frequencies ω or 2ω. In such a way the internal wave energy is continuously transferred to a series of waves with higher wave numbers. This phenomenon is predicted to occur in any stratified oceans. We perform an exact analytical analysis for a Boussinesq fluid, with a linearly-stratified density profile, for which a close-form solution can be obtained. Detuning effect is also taken into account for the near-resonance cases. For example, a $(3k, \omega)$ wave does not perfectly satisfy the dispersion relation and thus it will be slightly detuned to the "right" frequency determined by the dispersion relation. The

study proposes a mechanism that explains how a fraction of internal waves in the ocean are converted from large scales to that of turbulent mixing near reflecting boundaries, such as ocean ridges and steep continental slopes.

4.1 Governing Equations

We consider the propagation of internal waves in a stably-stratified fluid bounded by a free surface and a flat seafloor in the vertical direction. The flow is assumed inviscid, incompressible. We set up a Cartesian coordinate frame with x,y-axes on the mean free surface and z-axis positive upward. Under Boussinesq approximation the governing equation reads

$$\frac{D\mathbf{u}}{Dt} = -\frac{1}{\rho_0}(\nabla p + \rho g \nabla z), \quad -h < z < \eta \tag{4.1a}$$

$$\nabla \cdot \mathbf{u} = 0, \quad \frac{D\rho}{Dt} = 0, \quad -h < z < \eta \tag{4.1b}$$

$$\eta_t = \mathbf{u} \cdot \nabla(z - \eta), \quad \frac{Dp}{Dt} = 0, \quad z = \eta \tag{4.1c}$$

$$w = 0, \quad z = -h, \tag{4.1d}$$

where $\mathbf{u} = \{u, v, w\}$ is the velocity vector, ρ is the density and $\rho_0 = \bar{\rho}(z)|_{z=0}$ is the density on the mean free surface, $\bar{\rho}(z)$ is the background density, p is the pressure, η is the free surface elevation, g is the gravitational acceleration. Equation (4.1a) is the momentum equation, (4.1b) represents respectively continuity equation and conservation of salt (assuming that in the equation of state density only depends on salinity and diffusion of salt is neglected) . Equations (4.1c)-(4.1d) are the vertical boundary conditions on the free surface and the sea bottom.

Writing (4.1) primarily in the vertical velocity w and performing Taylor expansion on the free surface (correct up to the η terms) we obtain (see Thorpe, 1966; Liang et al., 2017, for details),

$$\frac{\partial^2}{\partial t^2}\nabla^2 w + N^2 \nabla_H^2 w = \frac{\partial^3}{\partial x \partial z \partial t}\mathbf{u} \cdot \nabla u + \frac{\partial^3}{\partial y \partial z \partial t}\mathbf{u} \cdot \nabla v - \frac{\partial}{\partial t}\nabla_H^2(\mathbf{u} \cdot \nabla w) + \frac{g}{\rho_0}\nabla_H^2\left(\mathbf{u} \cdot \nabla \rho'\right), \quad -h < z < 0, \tag{4.2a}$$

$$\frac{\partial^3 w}{\partial z \partial t^2} - g\nabla_H^2 w = \frac{\partial^2}{\partial x \partial t}\mathbf{u} \cdot \nabla u + \frac{\partial^2}{\partial y \partial t}\mathbf{u} \cdot \nabla v + g\nabla_H^2\left(\frac{dw}{dz}\eta\right) - \frac{1}{\rho_0}\nabla_H^2\left(\mathbf{u} \cdot \nabla p' + \frac{\partial^2 p'}{\partial z \partial t}\eta\right), \quad z = 0, \tag{4.2b}$$

$$w = 0, \quad z = -h. \tag{4.2c}$$

where we define the density perturbation ρ' such that $\rho = \bar{\rho}(z) + \rho'(x,y,z,t)$ and the pressure perturbation p' via $p = \bar{p}(z) + p'(x,y,z,t)$ such that $d\bar{p}(z)/dz = -\bar{\rho}(z)g$; $N^2 = -g/\rho_0 \mathrm{d}\bar{\rho}(z)/\mathrm{d}z$ is the Brunt-Väisälä frequency.

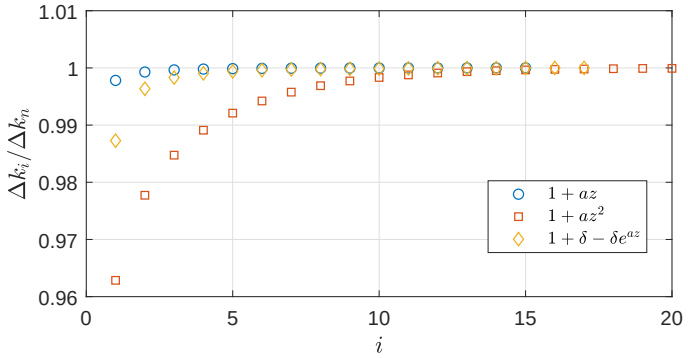


Figure 4.1: Difference of two consecutive horizontal wave numbers at a fixed frequency v.s. mode number i for linear, parabolic and exponential density profiles. In the vertical axis $\Delta k_i = k_{i+1} - k_i$. It is normalized by Δk_n which is the difference of the last two wave numbers (since Δk converges to a constant as n increases). The normalized frequency is 0.35 by $\sqrt{ga}$, $\sqrt{2gah}$ and $\sqrt{ga\delta}$ respectively. The linear profile is $\rho(z) = \rho_0(1+az)$ with $a = 5\times10^{-4}\mathrm{m}^{-1}$, the parabolic one is $\rho(z) = \rho_0(1+az^2)$ with $a = 1\times10^{-5}\mathrm{m}^{-2}$, and the exponential one is $\rho(z) = \rho_0[1+\delta-\delta\exp(az)]$ with $a = 0.1\mathrm{m}^{-1}$ and $\delta = 0.1$. Water depth is $h = 100$ m for all the three cases. The legend is $\rho(z)/\rho_0$.

Substitution of the linear wave solution $w = W(z)e^{i(kx-\omega t)}$ into the linearized form of (4.2) obtains the governing equation for $W(z)$,

$$\frac{d^2W(z)}{dz^2} + \frac{N^2(z)-\omega^2}{\omega^2}k^2W(z) = 0, \tag{4.3a}$$

$$\frac{dW(z)}{dz} - \frac{gk^2}{\omega^2}W(z) = 0, \quad z = 0, \tag{4.3b}$$

$$W(z) = 0, \quad z = -h. \tag{4.3c}$$

Equation (4.3) is Sturm-Louisville eigenvalue problem. Depending on the form $N(z)$ it can be solved analytically in terms of elementary (e.g. trigonometric, hyperbolic) or special functions (e.g. Airy, Bessel), or numerically as a general boundary value problem.

4.2 Roughly Equal-spaced Horizontal Wave Numbers at Fixed Frequencies

In this section we examine a property of internal gravity waves arising from its dispersion relation that states at a fixed frequency the horizontal wave numbers of internal gravity waves are approximately equal-spaced. Continuous triad resonance forms due to this property in the scenario we consider. It is obvious that the horizontal wave numbers are rigorously

equal-spaced under rigid-approximation when one recalls $k = n\pi/h\sqrt{\omega^2/(N^2-\omega^2)}$ where n is an integer that denotes the mode number. However, with consideration of a free surface, they are only approximately equal-spaced, for which reason we include detuning effect in the following analysis.
For a linear density profile, $\bar{\rho}(z) = \rho_0(1-az)$, with Brunt-Väisälä frequency $N = \sqrt{ga}$, the dispersion relation reads (see, Liang et al., 2017)

$$\mathscr{D}(k,\omega) = \omega^2 - \frac{gk^2}{m}\tan mh, \tag{4.4}$$

where m is the vertical wave number and

$$m = k\sqrt{\frac{N^2-\omega^2}{\omega^2}}. \tag{4.5}$$

Due to the free surface effect, it appears more complicated but actually differ very little from the classical one under rigid-lid approximation which is $\omega = N\cos\theta$ where θ is the angle of the wave number vector with the horizontal. In (Liang et al., 2017) we have shown that there exists a countably infinite number of internal waves that satisfy both $\mathscr{D}(k,\omega) = 0$ and $\mathscr{D}(2k,2\omega) = 0$ in a stratified fluid. Here by solving (4.3) numerically we present in figure 4.1 that the horizontal wave numbers of internal gravity waves are approximately equal-spaced at a fixed frequency in fluids with different stratification profiles. Δk_i is the difference of two consecutive wave numbers . As the mode number increases, Δk_i converges to a constant.

4.3 Resonance Mechanism

The scenario we consider is a monochromatic internal wave that satisfies $\mathscr{D}(k,\omega) = 0$ and $\mathscr{D}(2k,2\omega) = 0$ propagating towards a vertical wall boundary from an open ocean. The propagating wave first generate its second harmonic along its way $(2k,2\omega)$. They then together induce a new wave $(3k,\omega)$ upon reflection through triad resonance. This is not unexpected since the new wave $(3k,\omega)$ satisfies the dispersion relation given the property presented in section II that the horizontal wave numbers are approximately equal-spaced. Similarly this analysis also applies to a $(4k,2\omega)$ wave that can be generated from the (k,ω) and $(3k,\omega)$ waves. A series of triad resonances then continuously form approximately at the frequencies ω and 2ω respectively. Each triad involves waves propagating in both directions. Note that without the reflection mechanism only the second harmonic will form as shown in (Liang et al., 2017). The wave numbers are $(2I-1)k$ at frequency ω and $2Ik$ at frequency 2ω where $I = 1,2,3\ldots$. A schematic representation of this mechanism is shown in figure 4.1 (waves of wave numbers up to $6k$ are shown). It can be seen that the internal wave energy is transferred to the higher and higher wave numbers in smaller scales. In the following analysis, we take into the detuning effect that accounts for the fact that, for instance, the $(3k,\omega)$ wave only approximately satisfy the dispersion relation.

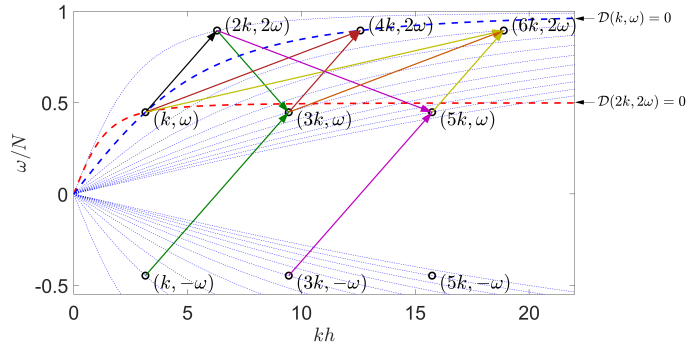


Figure 4.1: Representation of energy flow from small wavenumbers to higher ones after the monochromatic internal wave in discussion is reflected. The three waves associated with the arrow lines in the same color form one resonant triad. The second harmonic generation involves two wave (i.e., one arrow line). Here we only show energy flow to internal waves propagating to one direction (towards or away) on account of symmetry. The lighter dash lines show the dispersion relation of internal gravity waves $\mathscr{D}(k,\omega) = 0$. The intersecting heavier blue dash line and the red one are to illustrate how to find a wave that satisfy $\mathscr{D}(k,\omega) = 0$ and $\mathscr{D}(2k,2\omega) = 0$ simultaneously.

4.4 Derivation of Interaction Equation

Our analytical analysis focuses on linear density profiles, $\bar{\rho}(z) = \rho_0(1 - az)$, for which a closed-form solution can be easily found.

The linear solution of a right-propagating (for simplicity we consider the direction of propagating towards the boundary as right, away as left) monochromatic internal gravity wave for a linearly stratified fluid in a two dimensional domain reads

$$w = A \sin m(z+h) e^{i(kx-\omega t)} + \text{c.c.}, \tag{4.6a}$$

$$u = i\frac{Am}{k} \cos m(z+h) e^{i(kx-\omega t)} + \text{c.c.}, \tag{4.6b}$$

$$\rho' = i\frac{A\rho_0 a}{\omega} \sin m(z+h) e^{i(kx-\omega t)} + \text{c.c.}, \tag{4.6c}$$

$$p' = i\frac{Am\omega\rho_0}{k^2} \cos m(z+h) e^{i(kx-\omega t)} + \text{c.c.}, \tag{4.6d}$$

$$\eta = i\frac{A}{\omega} \sin mh e^{i(kx-\omega t)} + \text{c.c.}, \tag{4.6e}$$

where A is the amplitude of the vertical velocity; m and k are the vertical and horizontal wave numbers that satisfy $m = k\sqrt{N^2/\omega^2 - 1}$; $\sin m(z+h)$ is the vertical mode structure of internal gravity waves for the vertical velocity, solved from (4.3); "c.c." represents complex

conjugates and will be dropped hereafter for simplicity. It has been noticed that the above solution is exact to the fully nonlinear Boussinesq-Euler equation (i.e., (4.2a)) Tabaei et al. (2005). It then follows that if the upper boundary is approximated as a rigid lid, the high harmonics does not arise from a single plane wave since the nonlinear terms in the momentum equation vanish(Liang et al., 2017).

As we described previously, due to the reflecting boundaries, the wave field consists of a series of right-propagating and left-propagating waves. It can be expressed as, in the vertical velocity,

$$w = \sum_{n=1}^{N} \sin m_n(z+h)\Big\{A_n \exp i(k_n x - \omega_n t) + B_n \exp i(k_n x + \omega_n t)\Big\} \tag{4.7}$$

where A_n and B_n are the amplitudes of the nth right/left-propagating waves. N is the number of pairs of waves we consider.

Due to weakly nonlinear wave interactions, the wave amplitudes vary slowly in time but much less than the carrier wave Bretherton (2018). We define a slow temporal variable $t_1 = \varepsilon t$ where ε is a measure of wave steepness. The vertical velocity is then expressed as a convergence perturbation series

$$w(x,z,t,t_1) = \varepsilon w_1(x,z,t,t_1) + \varepsilon^2 w_2(x,z,t,t_1) + \mathscr{O}(\varepsilon^3) \tag{4.8}$$

where $w_i \sim \mathscr{O}(1)$. u, ρ', p' can be expressed in the similar way.

Substituting of the perturbation series into the governing equation(4.2) and collecting terms according to the order of ε, we obtain, at the leading order $\mathscr{O}(\varepsilon)$

$$\frac{\partial^2}{\partial t^2}\nabla^2 w_1 + N^2 \nabla_H^2 w_1 = 0, \quad -h < z < 0, \tag{4.9a}$$

$$\frac{\partial^3 w_1}{\partial z \partial t^2} - g\nabla_H^2 w_1 = 0, \quad z = 0, \tag{4.9b}$$

$$w_1 = 0, \quad z = -h. \tag{4.9c}$$

and at the second order $\mathscr{O}(\varepsilon^2)$

$$\frac{\partial^2}{\partial t^2}\nabla^2 w_2 + N^2 \nabla_H^2 w_2 + 2\frac{\partial^2}{\partial t \partial t_1}\nabla^2 w_1 = \frac{\partial^3}{\partial x \partial z \partial t}\mathbf{u}_1 \cdot \nabla u_1 - \frac{\partial^3}{\partial x^2 \partial t}\mathbf{u}_1 \cdot \nabla w_1 + \frac{g}{\rho_0}\nabla_H^2(\mathbf{u}_1 \cdot \nabla \rho_1'), \quad -h \le z \le 0. \tag{4.10a}$$

$$\frac{\partial^3 w_2}{\partial z \partial t^2} - g\nabla_H^2 w_2 + \frac{\partial^3 w_1}{\partial z \partial t \partial t_1} = \frac{\partial^2}{\partial x \partial t}\mathbf{u}_1 \cdot \nabla u_1 + \nabla_H^2\left(g\frac{dw_1}{dz}\eta_1 + N^2 w_1 \eta_1\right) - \frac{1}{\rho_0}\nabla_H^2\left(\mathbf{u}_1 \cdot \nabla p_1' + \frac{\partial^2 p_1'}{\partial z \partial t}\eta_1\right), \quad z = 0 \tag{4.10b}$$

$$w_2 = 0, \quad z = -h. \tag{4.10c}$$

To get the interaction equation, we now consider three right-propagating monochromatic wave trains of infinite length indexed by $0,1,2$ and roughly satisfy the triad resonance condition $k_0 = k_1 + k_2$ and $\omega_0 \simeq \omega_1 + \omega_2$. The 0th wave will be modulated due to the triad resonance. To take into the detuning effect, we define $\sigma = \omega_0 - (\omega_1 + \omega_2)$, representing the difference of the real frequency of the 0 wave and that of the resonating force from the 1st and 2nd waves.

Substitution of (4.7) that only consists of the three waves for w_1 and other corresponding components into (4.10) gives the general inhomogeneous resonance equation for the 0th wave

$$\frac{\partial^2}{\partial t^2}\nabla^2 w_{20} + N^2\nabla_H^2 w_{20} + 2\frac{\partial^2}{\partial t \partial t_1}\nabla^2 w_{10} = \mathscr{E} A_1 A_2 e^{i(k_0 x - \omega_0 t)} e^{i\sigma t}, \quad -h \le z \le 0, \tag{4.11a}$$

$$\frac{\partial^3 w_{20}}{\partial z \partial t^2} - g\nabla_H^2 w_{20} + \frac{\partial^3 w_{10}}{\partial z \partial t \partial t_1} = \mathscr{F} A_1 A_2 e^{i(k_0 x - \omega_0 t)} e^{i\sigma t}, \quad z = 0, \tag{4.11b}$$

$$w_{20} = 0, \quad z = -h. \tag{4.11c}$$

where

$$\mathscr{F} = f_1 \sin[(m_1 + m_2)(z+h)] + f_2 \sin[(m_1 - m_2)(z+h)], \tag{4.12a}$$

$$\mathscr{E} = f_3 \sin(m_1 + m_2)h + f_4 \cos(m_1 + m_2)h + f_5 \sin(m_1 - m_2)h + f_6 \cos(m_1 - m_2)h \tag{4.12b}$$

in which

$$f_1 = -i\frac{k_1 + k_2}{2}[(\omega_1 + \omega_2)(m_1^2 + k_1^2 - m_2^2 - k_2^2) + ga(k_1 + k_2)(\frac{k_1}{\omega_1} - \frac{k_2}{\omega_2})](\frac{m_1}{k_1} - \frac{m_2}{k_2}), \tag{4.13a}$$

$$f_2 = i\frac{k_1 + k_2}{2}[(\omega_1 + \omega_2)(m_1^2 + k_1^2 - m_2^2 - k_2^2) + ga(k_1 + k_2)(\frac{k_1}{\omega_1} - \frac{k_2}{\omega_2})](\frac{m_1}{k_1} + \frac{m_2}{k_2}), \tag{4.13b}$$

$$f_3 = -i\frac{g(k_1 + k_2)^2}{2}(\frac{m_1}{\omega_2} + \frac{m_2}{\omega_1}), \tag{4.13c}$$

$$f_4 = i\frac{(k_1 + k_2)(\omega_1 + \omega_2)}{2}[(\frac{k_1}{\omega_1} + \frac{k_2}{\omega_2})(\frac{m_1^2}{k_1^2}\omega_1 + \frac{m_2^2}{k_2^2}\omega_2) + (\frac{m_1^2\omega_1}{k_1\omega_2} + \frac{m_2^2\omega_2}{k_2\omega_1}) - 2m_1m_2(\frac{1}{k_1} + \frac{1}{k_2})], \tag{4.13d}$$

$$f_5 = i\frac{g(k_1 + k_2)^2}{2}(\frac{m_1}{\omega_2} - \frac{m_2}{\omega_1}), \tag{4.13e}$$

$$f_6 = -i\frac{(k_1 + k_2)(\omega_1 + \omega_2)}{2}[(\frac{k_1}{\omega_1} + \frac{k_2}{\omega_2})(\frac{m_1^2}{k_1^2}\omega_1 + \frac{m_2^2}{k_2^2}\omega_2) + (\frac{m_1^2\omega_1}{k_1\omega_2} + \frac{m_2^2\omega_2}{k_2\omega_1}) + 2m_1m_2(\frac{1}{k_1} + \frac{1}{k_2})]. \tag{4.13f}$$

$\mathscr{E}$ and $\mathscr{F}$ come from the nonlinear quadratic terms that resonate with the 0th wave. Note that the first index in w indicates its order in terms of ε and the second index here refers to

the 0th wave.

The generation of second harmonics can be considered together with the above form except that the expressions of $\mathscr{E}$ and $\mathscr{F}$ are different. Specifically, $\mathscr{E}=0$. Assume it satisfies that $k_0=2k_j, \omega_0=2\omega_j$, then to consider (4.11) for the 0th wave, $\mathscr{F}$ is

$$\mathscr{F}=-i\frac{12A_j^2 m_j g k_j^2 \sin m_j h}{\omega_j \cos m_j h}. \tag{4.14}$$

It is clear that nonlinear free surface boundary condition is essential here since otherwise $\mathscr{E}=0, \mathscr{F}=0$ and (4.11) becomes a homogenous equation. No second harmonics will be generated.

To solve (4.11), we assume the solution of w_{20} takes the following form,

$$w_{20}=G_2(t_1,z)e^{i(k_0x-\omega_0 t)}+G_1(t_1,z)e^{i(k_0x+\omega_0 t)}. \tag{4.15}$$

Substitution of (4.15) into (4.11) gives the governing equation of $G_2(t_1,z)$,

$$\frac{\partial^2 G_2}{\partial z^2}+m_0^2 G_2-2i\frac{dA_0}{dt}\frac{(k_0^2+m_0^2)\sin m_0(z+h)}{\omega_0}+\frac{\mathscr{E}}{\omega_0^2}e^{i\sigma t}=0, \quad -h<z<0, \tag{4.16a}$$

$$\frac{\partial G_2}{\partial z}-\frac{gk_0^2}{\omega_0^2}G_2+2i\frac{dA_0}{dt}\frac{m_0\cos m_0(z+h)}{\omega_0}+\frac{\mathscr{F}}{\omega_0^2}e^{i\sigma t}=0, \quad z=0, \tag{4.16b}$$

$$G_2=0, \quad z=-h. \tag{4.16c}$$

$G_1(t_1,z)$ is found to satisfy (4.3) and represent the vertical mode structures of internal gravity waves. It takes the form of $\sin m_0(z+h)$ in the case of linearly-stratified fluid.

Solving (4.16) gives the interaction equation that modulates the 0th wave

$$M_0\frac{dA_0}{dt}=\alpha A_1 A_2 e^{i\sigma t} \tag{4.17}$$

where

$$M_0=-i\frac{gk_0^2[m_0h(k_0^2+m_0^2)+(m_0^2-k_0^2)\sin m_0h\cos m_0h]}{m_0^2\omega_0\cos m_0h} \tag{4.18}$$

and

$$\alpha=c_1\cos(m_1-m_2)h+c_2\cos(m_1+m_2)h+c_3\sin(m_1-m_2)h+c_4\sin(m_1+m_2)h, \tag{4.19}$$

in which

$$c_1 = -f_6 - \frac{f_2(m_1 - m_2)}{(m_1 - m_2)^2 - m_0^2}, \tag{4.20a}$$

$$c_2 = -f_4 - \frac{f_1(m_1 + m_2)}{(m_1 + m_2)^2 - m_0^2}, \tag{4.20b}$$

$$c_3 = -f_5 + \frac{f_2 g k_0^2}{\omega_0^2[(m_1 - m_2)^2 - m_0^2]}, \tag{4.20c}$$

$$c_4 = -f_3 + \frac{f_1 g k_0^2}{\omega_0^2[(m_1 + m_2)^2 - m_0^2]}. \tag{4.20d}$$

The governing equations that modulate the 1st and 2nd waves can be obtained by simply changing the indices of the wave numbers and frequencies in (4.20) with proper signs.

Taking into all the triads that exchanging energy with the 0th wave (since there can be different pairs of waves that satisfy the triad resonance condition with the 0th wave), we obtain

$$M_0 \frac{dA_0}{dt} = \sum_{p,q} \alpha_{p,q} A_p A_q e^{i\sigma_{p,q}t} + \beta_j A_j^2, \tag{4.21}$$

where for the pth and qth waves it is satisfied that $k_0 = k_p + k_q$ and $k_p \neq k_q$; $\alpha_{p,q}$ can be obtained from (4.19); $\sigma_{p,q} = \omega_0 - \omega_p - \omega_q$. The second term takes into account the second harmonic case $k_j = k_0/2, \omega_j = \omega_0/2$ $(j \in Z)$ and

$$\beta_j = \frac{3 g m_j k_j^2 \sin m_j h}{\omega_j^2 \cos m_j h} \tag{4.22}$$

Note that $\alpha(j,j) \neq \beta(j)$. The equations that modulate the pth and qth waves can be obtained in a similar way to (4.21).

4.5 Results

The resonant interactions start from a low-mode internal wave and subsequently propagate to higher ones. So we keep increasing the number of waves in consideration until a convergence is reached for for a fixed time window. The energy cascade of a monochromatic internal gravity to high wave numbers is presented in figure 4.1. Initially there exist a right-propagating wave and a left-propagating one with the same physical parameters in the wave field, corresponding to the case of perfect reflection from vertical no-penetration boundaries.

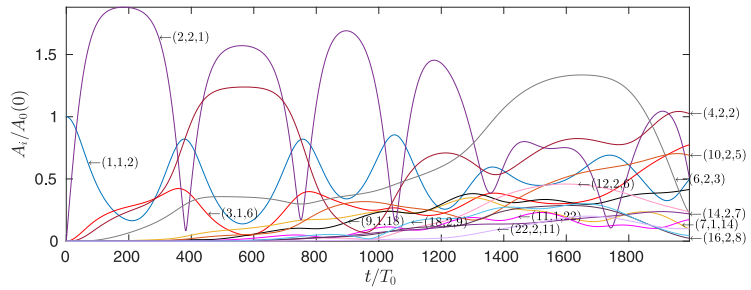


Figure 4.1: Time evolutions of a series of internal waves generated from a single monochromatic internal wave propagating to a vertical no-penetration boundary. The initial amplitudes of the $(2,2,1)$ waves is 1m for both the right-propagating and left-propagating waves, i.e., $A_0(0) = B_0(0) = 1$m. Totally $N = 53$ waves are taken into account, of which the largest 14 waves are presented. The three numbers associated with each wave in a parenthesis are normalized wave number, frequency and vertical mode number, for example, $(2,2,1)$ stands for a wave of wave number $2k$, frequency 2ω and mode 1, where $k = 0.0314\text{m}^{-1}$, $\omega = 0.0313\text{s}^{-1}$ in this case. $a = 5\times10^{-4}\text{m}^{-1}$,$H = 100$m.

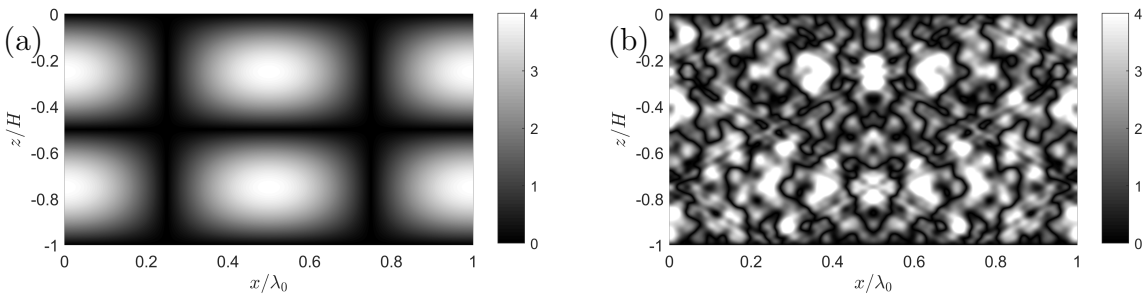


Figure 4.2: The wave field at $t = 0$ and at a later time point $t = 2\times10^3 T_0$, represented by the vertical velocity. $T_0 = 2\pi/\omega$, $\lambda_0 = 2\pi/k$, $H = 100$m.

As stated before, the mechanism requires the internal waves to satisfy the harmonic generation condition, i.e., $\mathscr{D}(2k, 2\omega) = 0$. It can be seen that the energy of the initial internal wave transfers to higher and higher wave numbers as time passes. In figure 4.2 we show the wave fields represented by the vertical velocity at $t = 0$ and $t = 2\times10^3 T_0$ where $T_0 = 2\pi/\omega$. The wave field gets steepened and converts to smaller scales. This trend will continue until wave breaking occurs. Note that since at some spacial and temporal point, the wave field might break, we do not take into account wave breaking in our analysis.

4.6 Conclusion

We show that there exists monochromatic internal gravity waves with wave number k and frequency ω, are capable of transferring energy to the higher wave numbers near vertical reflecting boundaries, on the condition that its 2nd harmonics satisfies the dispersion relation $\mathscr{D}(2k, 2\omega) = 0$. The wave field is more destabilized and prone to wave breaking as time passes. The result presented can be extended to the nth harmonics cases but supposedly with weaker effect, manifested by the perturbation analysis. The mechanism proposed here may partially explain internal wave spectrum formation and internal wave breaking near the continental slopes, mid-ocean ridges and so on, where reflecting boundaries prevail.

Chapter 5

Internal Waves Generation from Barotropic Tide Interacting with Ambient Waves

How and where the ocean tide on the earth loses its energy has been a problem of interest for geophysicists and oceanographers for over a century (Lambeck, 1980). It is now generally believed that the major loss of the tidal energy occurs due to the friction of bottom boundary layer in shallow marginal seas and generation of internal gravity waves from barotropic tides flowing over sea bottom topography in the deep ocean (Munk and Wunsch, 1998; Egbert and Ray, 2001).

It is estimated that totally about 1TW tidal energy is lost in the deep ocean by calculating the global barotropic tides from Topex-Poseidon altimetry data (Egbert and Ray, 2000, 2001). Inferred from the spatial pattern of the tidal energy loss in the open ocean (Egbert and Ray, 2000), most of the 1TW tidal energy loss is attributed to generation of internal tides from barotropic flowing over sea bottom topography (e.g., Sarkar and Scotti, 2017).

In the present study we report a mechanism for converting tidal energy to internal waves from the resonant interactions between barotropic tides and ambient internal waves. Internal gravity waves is a common phenomenon in density-stratified oceans. The most energetic part of internal waves predominantly have frequencies close to the tidal frequencies or the inertia frequency (Alford, 2003; Lamb, 2014). Roughly fifty percent of its total energy comes from baratropic tides flowing over bottom topography, referred to as internal tides, and the other half is from winds disturbing the mixed layer in the upper ocean.

Where there exists an uneven sea bottom, known as an established theory, internal tides can be generated by the resonating forces from a tidal current interacting with the sea bottom topography(Garrett and Kunze, 2007). Here we show that, in the case of a flat sea bottom, a barotropic tidal current interacting with ambient internal waves in the momentum equation and the free surface boundary, can generate new internal waves whose frequencies are shifted up by the tidal frequency.

The proposed mechanism can be approached from the point of view of a general triad-wave resonance theory : $(\mathbf{k}, \boldsymbol{\omega}) + (0, \boldsymbol{\sigma}) = (\mathbf{k}, \boldsymbol{\omega} + \boldsymbol{\sigma})$, where $\mathbf{k}, \boldsymbol{\omega}$ is the frequency and the wave number vector of an ambient internal wave, $\boldsymbol{\sigma}$ is the tidal frequency, $(\mathbf{k}, \boldsymbol{\omega} + \boldsymbol{\sigma})$ stands for a

new internal wave whose frequency and wave number comply the dispersion relation. Since barotropic tidal currents do not contribute to wave numbers, the two internal waves share the horizontal wave number vector but differ in frequency by a tidal frequency. We show in theory that the new internal wave can extract energy continuously from the baratropic tide, and this process is predicted to occur in any stratified oceans. While for general density profiles a closed form of analytical solutions may be limited, we present their exponential growth analytically in a linearly-stratified ocean for a quantitative study. To see the importance of the mechanism in the real ocean scenario, we consider a typical case in the Pacific Ocean and estimate the energy flux from baratropic tide to plane internal waves via this mechanism can reach order of $1\mathrm{MWm}^{-1}$ in weeks. It potentially accounts for an important part of the total loss of barotropic tides in the open ocean. The mechanism proposed here provides a new pathway for converting tidal energy and generating internal waves of low frequencies.

5.1 Interaction Equations

Consider an inviscid, incompressible flow in a stably stratified fluid, with a periodic tidal current in the background, bounded by a free surface and a flat seafloor in the vertical direction. We set up a Cartesian coordinate frame with x,y-axes on the mean free surface and z-axis positive upward. Under Boussinesq approximation the governing equation reads

$$\frac{D\mathbf{u}}{Dt}+\mathbf{f}\times\mathbf{u}=-\frac{1}{\rho_0}(\nabla p+\rho g\nabla z),\quad -h<z<\eta, \tag{5.1a}$$

$$\nabla\cdot\mathbf{u}=0,\quad -h<z<\eta, \tag{5.1b}$$

$$\frac{D\rho}{Dt}=0,\quad -h<z<\eta, \tag{5.1c}$$

$$\eta_t=\mathbf{u}\cdot\nabla(z-\eta),\quad z=\eta, \tag{5.1d}$$

$$\frac{Dp}{Dt}=0,\quad z=\eta, \tag{5.1e}$$

$$w=0,\quad z=-h, \tag{5.1f}$$

where $\mathbf{u}=\{u,v,w\}$ is the velocity vector, ρ is the density of the fluid and $\rho_0=\bar{\rho}(z)|_{z=0}$ is the density on the mean free surface in which $\bar{\rho}(z)$ is the background density, $\mathbf{f}=\{0,0,f\}$ is the planetary vorticity that depends on latitude, p is the pressure, η is the free surface elevation and g is the gravitational acceleration. Equation (5.1a) is the momentum equation, (5.1b) and (5.1c) represent respectively continuity equation and conservation of salt (assuming that in the equation of state density only depends on salinity and diffusion of salt is neglected (Kundu, 1990)) . Equations (5.1d)-(5.1f) are the vertical boundary conditions on the free surface and the sea bottom.

We rewrite (5.1) primarily in the vertical velocity w (Thorpe, 1966; Liang et al., 2017, see, e.g.,), perform Taylor expansion on the free surface (accurate up to the η terms) and obtain

$$\frac{\partial^2}{\partial t^2}\nabla^2 w + f^2\frac{\partial^2 w}{\partial z^2} + N^2\nabla_H^2 w = (\frac{\partial^3}{\partial x\partial z\partial t} - f\frac{\partial^2}{\partial y\partial z})\mathbf{u}\cdot\nabla u$$
$$+(\frac{\partial^3}{\partial y\partial z\partial t} + f\frac{\partial^2}{\partial x\partial z})\mathbf{u}\cdot\nabla v - \frac{\partial}{\partial t}\nabla_H^2(\mathbf{u}\cdot\nabla w) + \frac{g}{\rho_0}\nabla_H^2\left(\mathbf{u}\cdot\nabla\rho'\right), \quad -h < z < 0, \tag{5.2a}$$
$$\frac{\partial^3 w}{\partial z\partial t^2} + f^2\frac{\partial w}{\partial z} - g\nabla_H^2 w = (\frac{\partial^2}{\partial x\partial t} - f\frac{\partial}{\partial y})\mathbf{u}\cdot\nabla u$$
$$+(\frac{\partial^2}{\partial y\partial t} + f\frac{\partial}{\partial x})\mathbf{u}\cdot\nabla v + g\nabla_H^2\left(\frac{dw}{dz}\eta\right) - \frac{1}{\rho_0}\nabla_H^2\left(\mathbf{u}\cdot\nabla p' + \frac{\partial^2 p'}{\partial z\partial t}\eta\right), \quad z = 0, \tag{5.2b}$$
$$w = 0, \quad z = -h. \tag{5.2c}$$

where we define the density perturbation ρ' such that $\rho = \bar{\rho}(z) + \rho'(x,y,z,t)$ and the pressure perturbation p' via $p = \bar{p}(z) + p'(x,y,z,t)$ such that $d\bar{p}(z)/dz = -\bar{\rho}(z)g$ and $N^2 = -g/\rho_0 \mathrm{d}\bar{\rho}(z)/\mathrm{d}z$ is the Brunt-Väisälä frequency.
We first present an ambient plane internal gravity wave in the form (indexed by subscript "1") $w = A_1 W(z)\exp[i(\mathbf{k}\cdot\mathbf{x} - \omega_1 t] + \text{c.c.}$ where $\mathbf{k} = \{k_x, k_y\}$ is the horizontal wave number vector, ω_1 is the frequency, A_1 is the amplitude and $W(z)$ represents the vertical structure of the existing ambient internal wave. The horizontal velocity of the background tidal current is $U = D\exp(-i\sigma t) + \text{c.c.}$ in which D is the tidal amplitude, σ is the tidal frequency. "c.c." stands for the complex conjugate and will be dropped hereafter for simplicity. It is easy to show that the linear wave solutions to the system (5.1) can be written as

$$w = A_1 W(z)\exp[i(\mathbf{k}\cdot\mathbf{x} - \omega_1 t)], \tag{5.3a}$$
$$v = -\frac{iA_1 W'(z)(ifk_x - k_y\omega_1)}{\omega_1 k^2}\exp[i(\mathbf{k}\cdot\mathbf{x} - \omega_1 t)], \tag{5.3b}$$
$$u = \frac{iA_1 W'(z)(ifk_y + k_x\omega_1)}{\omega_1 k^2}\exp[i(\mathbf{k}\cdot\mathbf{x} - \omega_1 t)] + D\exp(-i\sigma t), \tag{5.3c}$$
$$\rho' = -\frac{iA_1 W(z)\bar{\rho}'(z)}{\omega_1}\exp[i(\mathbf{k}\cdot\mathbf{x} - \omega_1 t)], \tag{5.3d}$$
$$p' = -\frac{iA_1\rho_0 W'(z)(f^2 - \omega_1^2)}{\omega_1 k^2}\exp[i(\mathbf{k}\cdot\mathbf{x} - \omega_1 t)] + i\rho_0 D\sigma\exp(-i\sigma t)x - \rho_0 Df\exp(-i\sigma t)y, \tag{5.3e}$$
$$\eta = \frac{iA_1 W(z)}{\omega_1}\exp[i(\mathbf{k}\cdot\mathbf{x} - \omega_1 t)], \tag{5.3f}$$

where $W'(z) = dW(z)/dz$, $\bar{\rho}'(z) = d\bar{\rho}(z)/dz$ and k is the modulus of the wave number vector $\mathbf{k}$.

Substitution of w into the linearized form of (5.2) obtains the governing equation for $W(z)$,

$$\frac{d^2W(z)}{dz^2}+k^2\frac{N^2-\omega_1^2}{\omega_1^2-f^2}W(z)=0, \quad -h<z<0, \tag{5.4a}$$

$$\frac{dW(z)}{dz}-\frac{gk^2}{\omega_1^2-f^2}W(z)=0, \quad z=0, \tag{5.4b}$$

$$W(z)=0, \quad z=-h. \tag{5.4c}$$

Equation (5.4) is a Sturm-Louisville eigenvalue problem. Depending on the form of $N(z)$, $W(z)$ and the dispersion relation can be solved analytically in terms of elementary (e.g. trigonometric, hyperbolic) or special functions (e.g. Airy, Bessel), or numerically as a general boundary value problem. For (5.4) to admit internal wave solutions, the frequency ω satisfies $f<\omega<N$ or $N<\omega<f$.

The substution of all the linear solutions (5.3) into the quadratic terms of (5.2) obtains nonzero harmonic terms with a frequency $\omega_2=\omega_1+\sigma$ and wave number $\mathbf{k}$. If the frequency and wave number satisfy the dispersion relation (e.g., (5.7) for a linearly-stratified fluid) of internal gravity waves, following wave resonance theory Phillips (1981), a new internal wave of frequency ω_2 and wave number $\mathbf{k}$ can be excited (The subscript "2" is for the new wave). After substitution, the quadratic terms (i.e., R.H.S) of (5.2a) give,

$$R_1=-\exp[i(\mathbf{k}\cdot\mathbf{x}-\omega_2 t)]\frac{A_1Dk_x}{\omega_1} \left\{-W(z)k^2\omega_1\omega_2-N^2W(z)k^2+(\omega_1\omega_2+f^2)\frac{d^2W(z)}{dz^2}\right\}, \tag{5.5}$$

and those of (5.2b) give,

$$R_2=-\exp[i(\mathbf{k}\cdot\mathbf{x}-\omega_2 t)] \left\{\frac{A_1D(2k_x\omega_1\omega_2+k_xf^2+ik_yf\omega_2)}{\omega_1}\frac{dW(z)}{dz}\Big|_{z=0}\right\}. \tag{5.6}$$

Since for internal gravity waves R_1 and R_2 are generally not zeros inside the fluid domain or on the free surface for any density profiles, these resonant force terms are expected to excite a new internal wave that follows the form $\exp[i(\mathbf{k}\cdot\mathbf{x}-\omega_2 t)]$ in any stratified oceans.

For a quantitive study, we consider a linearly-stratified fluid for which a closed-form solution to (5.4) is available. The density profile considered here is $\bar{\rho}(z)=\rho_0(1-az)$ with Brunt-Väisälä frequency $N=\sqrt{ga}$.

Solving (5.4) obtains $W(z)=\sin m_1(z+h)$ which describes the vertical structure of internal waves and the dispersion relation

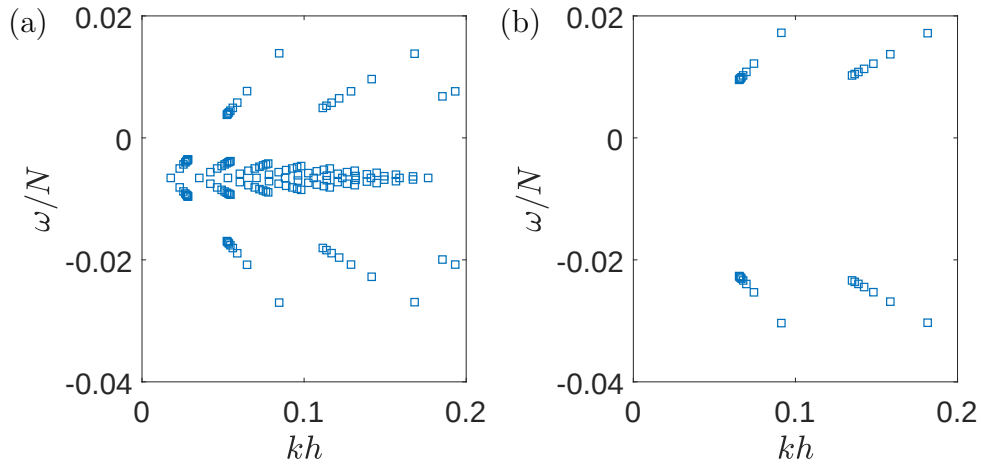


Figure 5.1: Wave solutions (k, ω_1) in the first 10 vertical modes that satisfy $\mathscr{D}(k, \omega_1) = 0$ and $\mathscr{D}(k, \omega_1 + \sigma) = 0$ (i.e., $\mathscr{D}(k, \omega_2) = 0$) obtained by extracting the intersections of the two curves, considering two latitudes (a): $f = 3.76 \times 10^{-5}\mathrm{s}^{-1}$ (the latitude is $15°N$); (b): $f = 1.03 \times 10^{-4}\mathrm{s}^{-1}$ (the latitude is $45°N$). The physical parameters used here are $a = 5 \times 10^{-6}\mathrm{m}^{-1}$, $h = 4000\mathrm{m}$, $\sigma = 1.45 \times 10^{-4}\mathrm{s}^{-1}$ (corresponding to the frequency of a M2 tidal current). Note that k here is the modulus of the horizontal wave vector $\mathbf{k}$, so one point in the figure represents a series of waves that satisfy $k_x^2 + k_y^2 = k^2$.

$$\omega_1^2 = \frac{gk^2}{m_1} \tan m_1 h + f^2, \tag{5.7}$$

where

$$m_1 = k\sqrt{\frac{N^2 - \omega_1^2}{\omega_1^2 - f^2}}, \tag{5.8}$$

is the vertical wave number.

Although complicated in its form, neglecting planetary vorticity f, (5.7) is in fact very close to the well-known dispersion relation of internal gravity waves in a linearly-stratified fluid: $\omega = N|\cos\theta|$ where θ is the angle of the wave number vector to the horizontal direction. Since a rigid-assumption approximation is not used, the vertical velocity does not vanish on the free surface due to $\sin mh \neq 0$. More discussion on the dispersion relation with effects of a free surface can be found in (Liang et al., 2017).

As stated before, a necessary condition for this mechanism to occur is that the wave numbers and frequencies of both internal waves satisfy dispersion relation, i.e., $\mathscr{D}(k, \omega_1) = 0$ and $\mathscr{D}(k, \omega_2) = 0$ where $\mathscr{D}$ is the dispersion relation (5.7). In figure 5.1, we solve for the admissible

waves in the first 10 modes numerically for a M2 tidal current at two latitudes. As wave number and frequency increase, the solutions become more and more sparse. In other words, the mechanism proposed here apply primarily to low-frequency internal waves.
It then follows that R_1 and R_2 in the scenario of a linear density profile become,

$$R_1 = \frac{A_1 D k_x \sin m_1(z+h)[m_1^2(\omega_1\omega_2+f^2)+k^2(\omega_1\omega_2+N^2)]}{\omega_1}\exp[i(\mathbf{k}\cdot\mathbf{x}-\omega_2 t)],$$

$$R_2 = -\frac{A_1 D m_1 \cos(m_1 h)(2k_x\omega_1\omega_2+f^2k_x+ifk_y\omega_2)}{\omega_1}\exp[i(\mathbf{k}\cdot\mathbf{x}-\omega_2 t)].$$

Due to the resonant forces R_1 and R_2, the excited new internal wave is expected to follow the form,

$$w = A_2(t)g_1(z)\exp[i(\mathbf{k}\cdot\mathbf{x}-\omega_2 t)] + g_2(z)\exp[i(\mathbf{k}\cdot\mathbf{x}-\omega_2 t)]. \tag{5.9}$$

Upon substitution of (5.9) into (5.2a) and (5.2c), we find

$$g_1(z) = \sin m_2(z+h) \tag{5.10a}$$

$$g_2(z) = \frac{1}{\omega_1 m_2(\omega_2^2-f^2)(m_2^2-m_1^2)}\Big\{-iA_2\omega_1\omega_2(m_2^2+k^2)(m_2^2-m_1^2)(z+h)\cos m_2(z+h) \tag{5.10b}$$

$$-A_1 D k_x m_2[(m_1^2+k^2)\omega_1\omega_2+N^2k^2+m_1^2f^2]\sin m_1(z+h)\Big\}$$

We non-dementionlize A_1, A_2, t in the following way,

$$A_1^* = \frac{A_1}{|D|},\quad A_2^* = \frac{A_2}{|D|},\quad t^* = \frac{t|D|}{h} \tag{5.11}$$

The problem can then be shown to depend on five dimensionless groups ah, kh, f/N, ω_1/N, σ/f, besides the initial amplitudes $A_1^*(t=0)$ and $A_2^*(t=0)$. For notational simplicity, we drop the asterisks in the following discussions in (5.11).
Solving (5.2b) obtains

$$\frac{dA_2}{dt} = \beta A_1 \frac{D}{|D|} \tag{5.12}$$

where

$$\beta = -\frac{im_2 h}{s_4 \omega_1 \omega_2} \tag{5.13}$$
$$\left\{ \frac{-gk^2 k_x [m_1^2 s_1 + k^2 s_2] \sin m_1 h - m_1 s_3 [(s_5 - s_4) k_x \omega_1 \omega_2 + (m_2^2 f^2 + k^2 N^2) k_x - i f k_y \omega_2 s_4] \cos m_1 h}{s_3 s_5 m_2 h \sin m_2 h + (-ghk^2 s_5 + s_3 s_6) \cos m_2 h} \right\}$$

where

$$s_1 = f^2 + \omega_1 \omega_2,\ s_2 = N^2 + \omega_1 \omega_2,$$
$$s_3 = f^2 - \omega_2^2,\ s_4 = m_1^2 - m_2^2,$$
$$s_5 = m_2^2 + k^2,\ s_6 = m_2^2 - k^2.$$

In a similar way, the presence of the new internal wave $(\mathbf{k}, \omega_2)$ and the barotropic tidal current in return modulates the original ambient $(\mathbf{k}, \omega_1)$ wave. Following the same procedures to derive (5.2b) we obtain

$$\frac{dA_1}{dt} = \alpha A_2 \frac{\bar{D}}{|D|} \tag{5.15}$$

where α can be formulated from the expression of β by replacing m_2 with m_1, ω_2 with ω_1. Here $\bar{D}$ is the complex conjugate of D. It should be noted that, under rigid-lid approximation, since α and β become zeros, the mechanism proposed here ceases to exist.

5.2 Analytical Results

Considering the amplitude of a barotropic tide D constant, we combine (5.12) and (5.15) and get

$$\frac{d^2 A_1}{dt^2} - \alpha\beta A_1 = 0, \tag{5.16a}$$
$$\frac{d^2 A_2}{dt^2} - \alpha\beta A_2 = 0, \tag{5.16b}$$

and furthermore,

$$A_{1,2}(t) = c_{1,2} \exp(\sqrt{\alpha\beta}t) + d_{1,2} \exp(-\sqrt{\alpha\beta}t) \tag{5.17}$$

where $c_{1,2}$ and $d_{1,2}$ are determined by the initial conditions of the two internal waves.
Here we consider a most relevant case in real application where initially there exists only one internal wave in the flow field (the so-called ambient wave in the analysis), i.e., $A_1(t=0) = \delta_1$

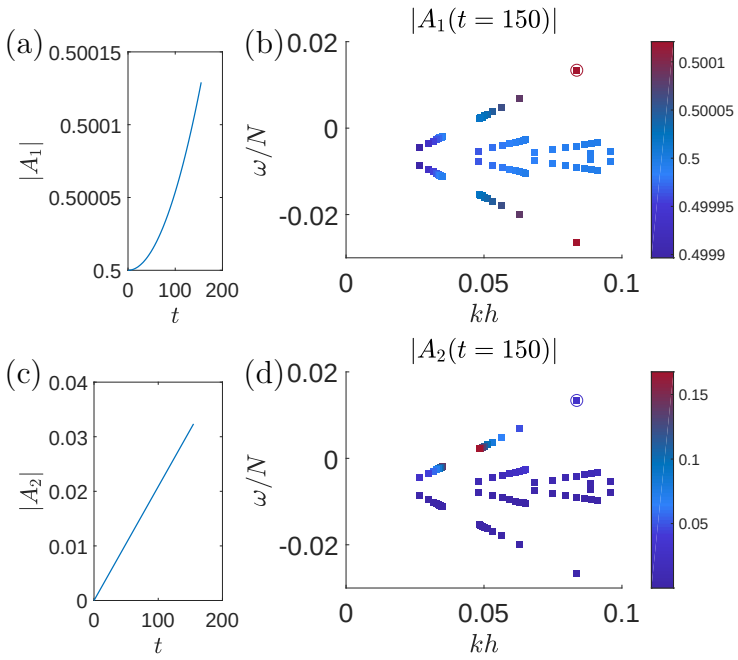


Figure 5.1: (a), (c): Time evolutions of the ambient wave and the new wave for a selected point (circled) in (b) and (d), from $t = 0$ to $t = 150$. For the ambient wave, $kh = 0.084$, $\omega/N = 0.013$. (b), (d): Wave amplitudes of all admissible waves up to $kh = 0.1$ at $t = 150$, the waves presented here correspond to those in 5.1(a) at latitude $15°N$. Color scale represents the moduli of $A_1(t)$ and $A_2(t)$. $\sigma/f = 7.98$, $ah = 5 \times 10^{-2}$, $f/N = 0.0016$, $\delta_1 = 0.5$, $\delta_2 = 0$.

and $A_2(t = 0) = 0$, with a baratropic tide in the background. The two coefficients for $A_1(t)$ can be found as

$$c_1 = \frac{\delta_1}{2} \tag{5.18a}$$

$$d_1 = \frac{\delta_1}{2}. \tag{5.18b}$$

and those for $A_2(t)$ are

$$c_2 = \frac{\beta}{2\sqrt{\alpha\beta}}\delta_1 \tag{5.19a}$$

$$d_2 = -\frac{\beta}{2\sqrt{\alpha\beta}}\delta_1. \tag{5.19b}$$

According to (5.17), (5.18) and (5.19), the two waves grow exponentially in time, whose amplitudes are determined by $\sqrt{\alpha\beta}$ and $\sqrt{\beta/\alpha}$.

In figure 5.1 we plot $A_1(t)$ and $A_2(t)$ according to (5.17), considering a case that the ambient wave propagate in the same direction parallel to the tidal current, such that $k_x = k$ and $k_y = 0$. The parameters used here are the same as in figure 5.1(a), but in dimentionless form. Figure 5.1 (a), (c) show the evolution of $|A_1|$ and $|A_2|$ as a function of time t for a given wave circled in (b) and (d). One can see that the amplitude of the ambient wave barely changes. For the new wave, since the exponent $\sqrt{\alpha\beta}$ in (5.17) is generally small, the exponential function appears linear. Figure 5.1 (b), (d) show the the amplitudes of the two waves at $t = 150$ for all admissible waves up to $kh = 0.1$. The color scale in figure 5.1 (b) and (d) represents the the moduli of $A_1(t)$ and $A_2(t)$.
We observe that the points in figure 5.1 (b) are symmetric in the vertical direction while (d) is not. A further examination shows that for the points in the upper half of the points in (d), the new waves have larger absolute frequency than their corresponding ambient waves, leading to an understanding that the new waves with increased frequency amplitude tend to grow faster while the ambient waves are not subject to this rule.

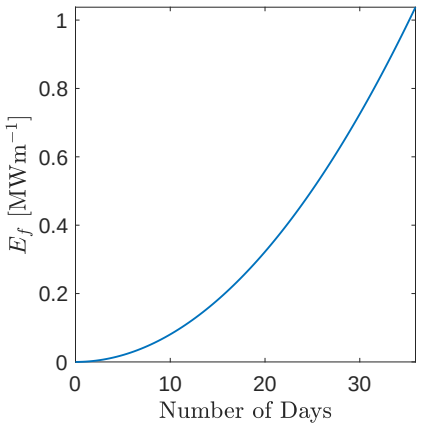


Figure 5.2: Energy flux E_f in (5.5) versus time in days. A M2 barotropic tide is considered with amplitude $D = 0.2\text{ms}^{-1}$. The ambient internal wave has an amplitude $A_1(t = 0) = 0.1\text{ms}^{-1}$, of vertical mode 2, and of frequency $\omega_1 = 1.48 \times 10^{-4}\text{s}^{-1}$ at the latitude $15°N$. The newly-generated internal wave has a frequency $\omega_2 = 2.94 \times 10^{-4}\text{s}^{-1}$, of mode 1. Water depth is 4000 m for the average depth of the Pacific Ocean. Stratification is 5% between the densities of water on the free surface and the sea bottom.

To see the efficiency of this mechanism in converting tidal energy to internal gravity waves, we calculate the energy flux of the tidal energy flowing into internal gravity waves, for a case matching figure 5.1 (a), (c), with typical physical parameters in the Pacific Ocean. Specifically, a M2 barotropic tidal current is considered with a periods of about 12 hours and amplitude of $D = 0.2\text{ms}^{-1}$ (which falls in the typical range of speed of barotropic currents (Garrett and Kunze, 2007)). The water depth of the ocean is 4000 and the stratification is 5% between the densities of water on ocean surface and in the bottom. We consider an

ambient internal wave of amplitude $A_1(t=0) = 0.1\text{ms}^{-1}$, of vertical mode 2, and of frequency $\omega_1 = 1.48 \times 10^{-4}\text{s}^{-1}$ at the latitude $15°N$. The resonated new wave then has a frequency $\omega_1 + f = 2.94 \times 10^{-4}\text{s}^{-1}$, of mode 1. We are interested in the change of the system's energy flux formulated in (5.5)

$$E_f = \sum_{i=1}^{2} [e_i(t) - e_i(0)] C_{gi} \tag{5.20a}$$

where $e_i(t)$ is the energy density of the ith plane internal gravity wave and

$$e_i(t) = \frac{\rho_0 A_i^2}{8m_i} \Big[\frac{2m_i hga}{\omega_i^2} + (\frac{ga}{\omega_i^2} - 2) \sin 2m_i h \Big],$$

C_{gi} is the group velocity of the plane wave in the horizontal direction.
The dimensionless time we consider $t = 150$ is equivalent to ~ 35 days. It can be seen from figure 5.2, as time increases, the energy flux from tidal current to internal waves keeps increasing. If we assume the internal wave survives about 35 days in the ocean, the energy flux reaches 1 MWm^{-1}. It should be noted that depending on the the amplitude of the internal waves, the tidal current, water depth, ocean stratification, their wave lengths and frequencies, the latitude, and the length of survival of the internal waves, the energy flux varies. If we assume 10% of the 1TW total energy loss in the deep open ocean is attributed to this mechanism, it requires 1×10^5m long wavefront for the plane internal gravity waves.

5.3 Conclusion

To summarize, we presented a mechanism for converting barotropic tidal energy to internal gravity waves through resonance. The ambient internal wave and the newly-generated one continuously extract energy from the barotropic tidal current. For a typical case in the real ocean scenario, we estimate that the energy flux through this mechanism can reach 1MWm^{-1}. This mechanism provides a new way for converting tidal energy through generation of internal gravity waves, the further breaking of which increases ocean turbulent mixing.

Chapter 6

Cascading of Internal Waves Energy to Large Wavenumbers by Seabed Corrugations

Motivated by several observations of enhanced (by orders of magnitude) and intense mixing over rough topographies of the oceans and the claimed attribution of this observation to internal wave breaking (e.g. Ledwell et al., 2000; Garabato et al., 2004), as well as reports of strong internal wave generation over undular seabed (e.g. Kranenburg et al., 1991), this study investigates and elaborates on details of Bragg resonance of internal waves in a continuously stratified fluid. From the governing equations we show that if two internal waves with wavenumbers and frequencies $(\mathbf{k}_{i1}, \omega_{i1})$ and $(\mathbf{k}_{i2}, \omega_{i2})$ with seabed corrugations of wavenumber $\mathbf{k}_b$ satisfy the Bragg condition, i.e.,

$$\mathbf{k}_{i1} \pm \mathbf{k}_{i2} \pm \mathbf{k_b} = 0$$
$$\omega_{i1} = \omega_{i2}$$

then the two waves are in resonance through the seabed component. This is expected and similar to Bragg resonance in homogeneous (Liu and Yue, 1998) and two-layer density stratified fluids (Alam et al., 2009b). However, contrary to Bragg resonance in a homogeneous and two-layer model (with rigid lid), in which seabed undulations can only reflect incoming waves, in continuously stratified waters a single harmonic of the seabed corrugations may simultaneously satisfy Bragg resonance between several internal wave modes. As a result, through just a single component of the seabed undulations and under Bragg condition, energy flows from an initial internal wave to a number of shorter internal waves, and then the energy of those short waves to even shorter waves and so on. Here we provide the analytical solution via multiple-scale analysis for the evolution of amplitudes of internal waves under Bragg resonance, and show that our theoretical predictions compare well with results from direct simulation of the full Euler's equation.

Resonant transfer of energy to short internal waves through the seabed irregularities may play an important role in the energy balance of internal wave spectrum, particularly in shallower waters of continental shelves (c.f. Olbers, 1976). The sequence of chain interactions that

passes the energy to shorter waves is a one way no-return journey for the energy of internal waves: an internal wave that falls under such condition is fated to permanently lose its energy to shorter waves and eventually to viscous dissipation (c.f. Staquet and Sommeria, 2002; Garrett and Munk, 1972a,b).

6.1 Governing Equations

Consider the propagation of waves in an inviscid, incompressible, adiabatic and stably stratified fluid of density $\rho(x,y,z,t)$, bounded by a free surface on the top and a rigid seafloor with a mean depth h at the bottom. We consider a Cartesian coordinate system with x,y-axes on the mean free surface and z-axis positive upward. Equations governing the evolution of the velocity vector $\mathbf{u}=\{u,v,w\}$, density ρ, pressure p and surface elevation η under Boussinesq approximation read

$$\rho_0\frac{D\mathbf{u}}{Dt}=-\nabla p-\rho g\nabla z,\quad -h+b<z<\eta \tag{6.1a}$$

$$\frac{D\rho}{Dt}=0,\quad -h+b<z<\eta \tag{6.1b}$$

$$\nabla\cdot\mathbf{u}=0,\quad -h+b<z<\eta \tag{6.1c}$$

$$\eta_t=\mathbf{u}\cdot\nabla(z-\eta),\quad z=\eta \tag{6.1d}$$

$$\frac{Dp}{Dt}=0,\quad z=\eta \tag{6.1e}$$

$$\mathbf{u}\cdot\nabla(z-b)=0,\quad z=-h+b \tag{6.1f}$$

where $b(x,y)$ represents small seabed irregularities superposed on the mean seabed such that the seafloor is given by $z=-h+b(x,y)$, g is the gravitational acceleration, and $\rho_0=\bar{\rho}(z=0)$ is the mean density on the free surface with $\bar{\rho}(z)$ the background (unperturbed) density such that $\rho=\bar{\rho}(z)+\rho'(x,y,z,t)$. Equation (6.1a) is the momentum equating (Euler's equations), (6.1b) comes from conservation of energy, and (6.1c) is continuity equation that together form five equations for five unknown variables of the problem (thee components of velocity $\mathbf{u}$, pressure p and density ρ). Equations (6.1d)-(6.1f) are boundary conditions on the free surface and the bottom.

Similar to the density perturbation ρ', we define a pressure perturbation p' via $p=\bar{p}(z)+p'(x,y,z,t)$ such that $d\bar{p}(z)/dz=-\bar{\rho}(z)g$. For the linear terms of the governing equation (6.1a) to be only in terms of w we calculate $\partial/\partial z[\nabla\cdot(6.1\text{a})]-\nabla^2(6.1\text{a})_3$, where $(6.1\text{a})_3$ denotes the z component of (6.1a)(likewise, 1,2 for x,y will be used later). We obtain

$$\frac{\partial}{\partial t}\nabla^2 w-\frac{\partial^2}{\partial x\partial z}\mathbf{u}\cdot\nabla u-\frac{\partial^2}{\partial y\partial z}\mathbf{u}\cdot\nabla v+\nabla_H^2(\mathbf{u}\cdot\nabla w)+\frac{g}{\rho_0}\nabla_H^2\ \rho'=0. \tag{6.2}$$

where $\nabla_H^2=\partial^2/\partial x^2+\partial^2/\partial y^2$ is the horizontal Laplacian. Taking the time derivative of (6.2) and substituting ρ' from the expansion of (6.1b), i.e.,

$$\frac{\partial\rho'}{\partial t}+\mathbf{u}\cdot\nabla\rho'+w\frac{d\bar{\rho}(z)}{dz}=0. \tag{6.3}$$

and denoting $N^2 = -g/\rho_0 \mathrm{d}\bar{\rho}(z)/\mathrm{d}z$ as the Brunt-Väisälä frequency, we obtain

$$\frac{\partial^2}{\partial t^2}\nabla^2 w + N^2\nabla_H^2 w = \frac{\partial^3}{\partial x \partial z \partial t}\mathbf{u}\cdot\nabla u + \frac{\partial^3}{\partial y \partial z \partial t}\mathbf{u}\cdot\nabla v - \nabla_H^2\frac{\partial}{\partial t}(\mathbf{u}\cdot\nabla w) + \frac{g}{\rho_0}\nabla_H^2(\mathbf{u}\cdot\nabla\rho'). \quad (6.4)$$

To perform a weakly nonlinear analysis, we assume that internal waves in the system described above are small perturbations from the mean state of water at rest, i.e. $\mathbf{u}, \rho', p' \sim \mathscr{O}(\varepsilon)$, where ε is a measure of the wave steepness. Expanding the surface kinematic boundary condition (6.1e) and keeping terms up to the second order we obtain

$$\frac{\partial p'}{\partial t} = w\rho_0 g - \mathbf{u}\cdot\nabla p' - \frac{\partial^2 p'}{\partial z \partial t}\eta + \rho_0 g \eta \frac{\partial w}{\partial z}, \quad z = 0. \quad (6.5)$$

Here p' can be substituted from an expression obtained from taking the x derivative of $(6.1\mathrm{a})_1$ added to the y derivative of $(6.1\mathrm{a})_2$:

$$-\frac{\partial^3 w}{\partial z \partial t^2} + \frac{1}{\rho_0}\nabla_H^2\frac{\partial p'}{\partial t} + \frac{\partial^2}{\partial x \partial t}\mathbf{u}\cdot\nabla u + \frac{\partial^2}{\partial y \partial t}\mathbf{u}\cdot\nabla v = 0. \quad (6.6)$$

Substituting $\partial p'/\partial t$ from (6.6) in (6.5) we obtain

$$\frac{\partial^3 w}{\partial z \partial t^2} - g\nabla_H^2 w = \frac{\partial^2}{\partial x \partial t}\mathbf{u}\cdot\nabla u + \frac{\partial^2}{\partial y \partial t}\mathbf{u}\cdot\nabla v + g\nabla_H^2\left(\frac{dw}{dz}\eta\right) - \frac{1}{\rho_0}\nabla_H^2\left(\mathbf{u}\cdot\nabla p' + \frac{\partial^2 p'}{\partial z \partial t}\eta\right). \quad (6.7)$$

We also assume that the steepness of seabed corrugations is small and comparable with that of internal waves, i.e. $\mathscr{O}(\varepsilon)$. Expanding the bottom boundary condition to the second order gives

$$w = u\frac{db}{dx} + v\frac{db}{dy} - b\frac{dw}{dz}, \quad z = -h. \quad (6.8)$$

Now let's consider the linearized form of the governing equation (6.4) and boundary conditions (6.7) on the free surface and (6.8) on the seabed. We look for a progressive wave solution of the form $w = W(z)\sin(\mathbf{k}\cdot\mathbf{x} - \omega t)$ where $\mathbf{k} = \{k_x, k_y, 0\}$ is the wave number, ω is the frequency and $W(z)$ represents the vertical structure of waves. Upon substitution of this form into the linearized equations we obtain (e.g. Thorpe, 1966)

$$\frac{d^2 W(z)}{dz^2} + |\mathbf{k}|^2\frac{N^2(z) - \omega^2}{\omega^2}W(z) = 0, \quad (6.9\mathrm{a})$$

$$\frac{dW(z)}{dz} - g\frac{|\mathbf{k}|^2}{\omega^2}W(z) = 0, \quad z = 0, \quad (6.9\mathrm{b})$$

$$W(z) = 0, \quad z = -h. \quad (6.9\mathrm{c})$$

Equation (6.9) is a general Sturm-Louisville eigenvalue problem. Depending on $N(z)$ it can be solved analytically in terms of elementary (e.g. trigonometric, hyperbolic) or special functions (e.g. Airy, Bessel), or numerically as a general boundary value problem.

We focus our attention here on the two-dimensional problem with a linear mean density profile, i.e. $\bar{\rho}(z) = \rho_0(1 - az)$ (c.f. e.g. Martin et al., 1972) which gives a constant Brunt-Väisälä frequency $N = \sqrt{ga}$ and the following dispersion relation

$$\omega^2 = \frac{gk}{\sqrt{1 - ga/\omega^2}} \tanh\left(kh\sqrt{1 - ga/\omega^2}\right), \quad \omega > N = \sqrt{ga} \tag{6.10a}$$

$$\omega^2 = \frac{gk}{\sqrt{ga/\omega^2 - 1}} \tan\left(kh\sqrt{ga/\omega^2 - 1}\right), \quad \omega < N = \sqrt{ga}. \tag{6.10b}$$

The behavior of dimensionless frequency $\omega/\sqrt{ga}$ as a function of dimensionless wavenumber kh is shown in fig 6.1. A cut-off frequency $\omega/\sqrt{ga}$=1 sets an upper frequency limit for internal waves which corresponds to the Brunt-Väisälä frequency. For $\omega > \sqrt{ga}$ only one solution exists in the first quadrant (with its mirrors in the other quadrants). This solution corresponds to a wave whose associated fluid particle motion is maximum near the free surface and decreases as the depth increases. Therefore this is basically a surface wave which is a little perturbed because of stratification. For $\omega < \sqrt{ga}$ there is an infinite number of solutions to (6.10b). The first member of this set, is the continuation of the surface wave branch (shown with a green color in fig. 6.1), but the rest identify waves with associated fluid particle activities that are minimum near the free surface and the seabed, but gain one (or more) maximum/maxima somewhere in the middle of the fluid domain. Therefore these branches show internal waves.

The condition for Bragg resonance is also shown in fig 6.1: if an internal wave of frequency ω and wavenumber k_i propagates over seabed undulations of wavenumber k_b such that $k_r = k_i + k_b$ is a wavenumber of another internal wave, i.e. the pair $(\omega, k_i + k_b)$ falls on any of branches of the dispersion relation, then waves k_i, k_r are in resonance. Interestingly, if ah is small (which is in fact the case in real oceans) then $k_{r2} = k_i + 2k_b$ is another resonant wave and likewise $k_{rn} = k_i + nk_b$ as is seen in fig 6.1. This chain of resonancs happens because wavenumbers of different internal wave modes that are associated with a specific frequency are (almost) equally spaced (they are perfectly equally spaced under rigid lid assumption, and to the leading order under free surface assumption employed here). Therefore a single component of the seabed can engage a single internal wave in an infinite number of Bragg resonances. In the next section we discuss the implications of this unique property of internal waves.

6.2 Perturbation Analysis

Here we present, via multiple-scale analysis, the analytical solution which is uniformly valid in time to (6.4) with boundary conditions (6.7), (6.8) in two spatial dimensions and under Bragg resonance condition. We assume that all variables of the problem $\mathbf{u}, p', \rho'$ are functions of x, z, t and the slow time $t_1 = \varepsilon t$. The slow time independent variable t_1 is introduced so that we can take slow variations of the variables into account, hence making the leading order solution

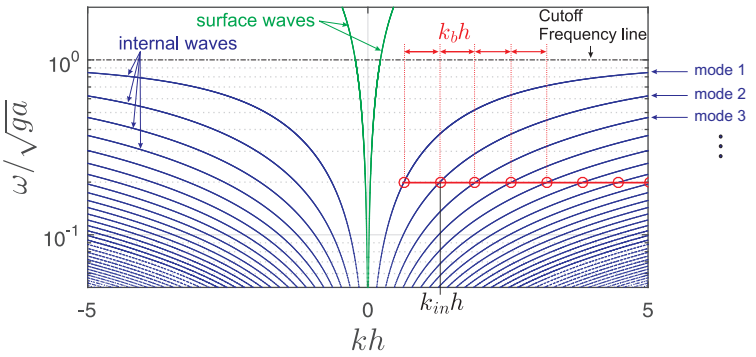


Figure 6.1: Dimensionless frequency versus dimensionless wavenumber of free waves in a fluid of linearly stratified density $\rho(z) = \rho_0(1 - az)$, with $ah = 0.05$ (c.f. (6.10)). Associated with each wavenumber there is a single surface wave (green branch) and an infinite number of internal wave modes (blue branches). Frequency of internal waves cannot exceed the Brunt-Väisälä frequency (dash-dotted line). The figure also shows Bragg resonance condition: if an internal wave of wavenumber k_{in} arrives at the seabed corrugations of wavenumber k_b, a new (resonant) internal wave of wavenumber $k_r = k_{in} + k_b$ is excited. This new wave k_r with the same topography k_b satisfies (nearly) another Bragg condition with another resonant wave $k_{r2} = k_{in} + 2k_b$, and so on. Therefore energy of the initial wave k_{in} is gradually transferred to shorter waves.

valid for longer times. We also assume that the solution to (6.4) can be expressed in terms of a convergent perturbation expansion. This means that, for example, the vertical velocity $w = w(x,z,t,t_1)$ can be obtained in the form of a convergent series $w = w^{(1)} + w^{(2)} + ... + w^{(m)}$ in which $w^{(m)} \sim \mathscr{O}(\varepsilon^m)$ with $\varepsilon \ll 1$ being a measure of wave steepness. We consider a single component of the seabed corrugations as $b(x) = f_b \sin k_b x$ where $f_b = \mathscr{O}(\varepsilon)$ and k_b is its wavenumber. At the leading order ε^1, we obtain the linear equations

$$\frac{\partial^2}{\partial t^2}\nabla^2 w^{(1)} + N^2 \nabla_H^2 w^{(1)} = 0, \tag{6.11a}$$

$$\frac{\partial^3 w^{(1)}}{\partial z \partial t^2} - g\nabla_H^2 w^{(1)} = 0, \quad z = 0, \tag{6.11b}$$

$$w^{(1)} = 0, \quad z = -h, \tag{6.11c}$$

whose solution is a superposition of internal modes, i.e. $w^{(1)} = \sum_{i=1}^{\infty} w_i^{(1)}$, where

$$w_i = A_i(t_1) \sin K_i(z+h) \sin(k_i x - \omega t), \; K_i = k_i \beta = k_i \sqrt{ga/\omega^2 - 1}. \tag{6.12a}$$

At the second order $\mathscr{O}(\varepsilon^2)$, dropping non-resonant terms (i.e. nonlinear wave-wave interac-

tion), we have

$$\frac{\partial^2}{\partial t^2}\nabla^2 w^{(2)} + N^2\nabla_H^2 w^{(2)} + 2\varepsilon\frac{\partial^2}{\partial t\partial t_1}\nabla^2 w^{(1)} = 0 \tag{6.13a}$$

$$\frac{\partial^3 w^{(2)}}{\partial z\partial t^2} - g\nabla_H^2 w^{(2)} + 2\varepsilon\frac{\partial^3 w^{(1)}}{\partial z\partial t\partial t_1} = 0, \quad z = 0 \tag{6.13b}$$

$$w^{(2)} = u^{(1)}\frac{\partial b}{\partial x} - \frac{\partial w^{(1)}}{\partial z}b, \quad z = -h. \tag{6.13c}$$

As we will show, a periodic solution to (6.13) can only exist if A_i satisfies the so-called compatibility condition (see e.g. Mei, 1985). To see this, let us assume that $w^{(2)} = \sum_{i=1}^{\infty} w_i^{(2)}$ where

$$w_i^{(2)} = g_{1i}(z,t_1)\sin(k_i x - \omega t) + g_{2i}(z,t_1)\cos(k_i x - \omega t). \tag{6.14}$$

Then, substituting (6.14) into (6.13), we find that $g_{1i}(z,t_1)$ satisfies the leading order problem, i.e. $g_{1i} = G_{1i}(t_1)\sin K_i(z+h)$ (c.f. (6.9)), and we obtain for g_{2i} the ordinary differential equation

$$-\frac{d^2 g_{2i}}{dz^2}\omega^2 + g_{2i}k_i^2(\omega^2 - ga) + 2\varepsilon\omega(k_i^2 + K_i^2)\frac{dA_i(t_1)}{dt_1}\sin K_i(z+h) = 0. \tag{6.15}$$

The solution g_{2i} of (6.15) subject to the boundary condition (6.13b) becomes

$$g_{2i} = \varepsilon\frac{dA_i(t_1)}{dt_1}\left[-\frac{k_i^2 + K_i^2}{K_i\omega}z + \frac{\omega(-k_i^2 + K_i^2)\cos K_i h}{K_i(K_i\omega^2\sin K_i h + gk_i^2\cos K_i h)}\right]\cos K_i(z+h), \tag{6.16}$$

while (6.13c), enforced at $z = -h$, requires

$$g_{2i}(-h) = 1/2\ \beta f_b k_i(A_{i-1} - A_{i+1}). \tag{6.17}$$

In (6.17), $k_{i-1} = k_i - k_b$ and $k_{i+1} = k_i + k_b$, although we shall recall that these conditions are true only to the leading order (in small parameter ah), or under the rigid lid assumption. Clearly, g_{2i} satisfies (6.16) and (6.17) if and only if A_i satisfies the compatibility condition:

$$\frac{dA_i}{dt} = S_i\ (A_{i-1} - A_{i+1}), \tag{6.18}$$

where the energy transfer frequency S_i is given by

$$\frac{S_i}{\omega} = \frac{f_b}{h}\frac{\beta^3 k_i h}{2\beta k_i h(1+\beta^2) + (\beta^2 - 1)\sin 2\beta k_i h}. \tag{6.19}$$

The set of equations (6.18) is a telescoping series. Dividing both sides by S_i, multiplying by A_i, and adding all the equations we obtain

$$\frac{d}{dt}\sum_{i=1}^{\infty}\frac{A_i^2}{S_i} = 0, \tag{6.20}$$

which can be shown to correspond to the conservation of energy equation (including potential energy, kinetic energy, and free-surface energy). For a single internal mode, the kinetic, potential, and free-surface energy is

$$E_{KE} = \int_0^{\lambda_i} dx \int_{-h}^{0} dz \frac{\rho_0}{2}(u_i^2 + w_i^2), \tag{6.21}$$

$$E_{PE} = \int_0^{\lambda_i} dx \int_{-h}^{0} dz \frac{\rho_i'^2 g^2}{2\rho_0 N^2}, \tag{6.22}$$

$$E_{FS} = \int_0^{\lambda_i} dx \int_0^{\eta_i} dz \rho_0 g z. \tag{6.23}$$

We then use the continuity and energy equation to express u_i and ρ_i' in terms of $w_i = A_i \sin K_i(z+h)\sin(k_i x - \omega t)$ such that

$$E_{KE} + E_{PE} + E_{FS} = \frac{\rho_0 A_i^2}{8K_i}\left[2K_i h g a/\omega^2 + (ga/\omega^2 - 2)\sin 2K_i h\right] = \frac{A_i^2}{S_i}\frac{\rho_0 \omega f_b (ga/\omega^2 - 1)}{8}. \tag{6.24}$$

6.3 Results and Discussions

Equation (6.18) shows that the rate of growth of the amplitude of mode i is a function of amplitudes of adjacent modes, i.e. A_{i-1} and A_{i+1}. But since (6.18) is valid for every i, then the rate of growth of A_{i-1} and A_{i+1} is clearly a function of A_i (as well as A_{i-2} and A_{i+2} respectively). Therefore, if initially only an internal wave of mode i with an initial amplitude A_i is present in the water, then its energy will first gradually flow to A_{i-1} and A_{i+1}; and then at a later time these flow to A_{i-2} and A_{i+2} and the spread continues over time. Therefore, for an accurate prediction of evolution of different wave amplitudes, a correct number of modes n must be taken into account. Choosing n=6 modes, for instance, we find that the governing equation for A_1 reads

$$\begin{aligned} &A_{1tttttt} + (S_1S_2 + S_2S_3 + S_3S_4 + S_4S_5 + S_5S_6)A_{1tttt} + (S_1S_2S_3S_4 + S_1S_2S_4S_5 \\ &+ S_2S_3S_4S_5 + S_1S_2S_5S_6 + S_2S_3S_5S_6 + S_3S_4S_5S_6)A_{1tt} + S_1S_2S_3S_4S_5S_6A_1 = 0. \end{aligned} \tag{6.25}$$

Note that for $\mathrm{d}A_1/\mathrm{d}t$ equation we must set $A_0 = 0$ unless k_b is such that a surface wave or a reflected internal wave is excited. Expressions similar to (6.25) obtain for other amplitudes $A_{2,\ldots,6}$. The six constants necessary to determine A_1 from (6.25) are obtained from the initial conditions of A_i (note that six equations obtained are dependent).

Prediction of energy exchange due to Bragg interaction between an internal wave and only its "immediate" adjacent waves is only valid for a finite initial time. For longer times, higher modes must be taken into account as is seen in the case study shown in fig 6.1. Here, to show the general behavior of such resonance, we consider that the initial wave is a mode 2 internal wave, with a normalized frequency $\omega/\sqrt{ga} = 0.2$ (corresponds to normalized wavenumber

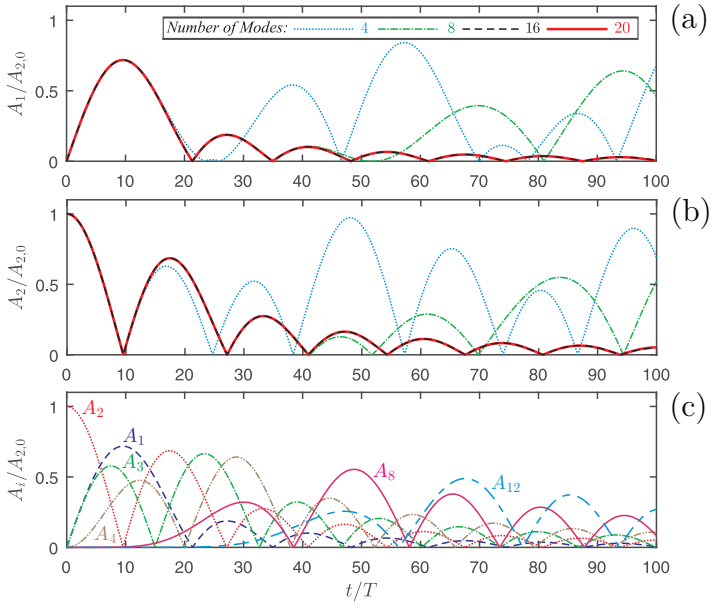


Figure 6.1: (a,b) Time evolution of amplitude of a resonant wave A_1 and initial wave A_2 when different number of wave modes n are taken into account in the governing equation (6.18). For longer time interactions higher number of modes come into the play and hence must be taken into account. (c) Time evolution of amplitudes of the initial wave A_2 and a select of resonant waves $A_{1,3,4,8,12}$. Over time energy flows from lower wave number modes to higher ones. At later times new waves such as A_8 emerge, but they too give up their energy to even higher wave number modes (e.g. A_{12}). A single seabed component via Bragg resonance shifts the initial wave energy, one wave by one wave, to shorter and shorter waves.

$k_2h = 1.28$) in a linearly stratified fluid of $ah = 0.05$ and with a steepness of $kA_{2,0} = 0.002$ over topography undulations of steepness $k_bf_b = 0.026$ that satisfies Bragg resonance with modes 1 and 3 internal waves (c.f. fig 6.1). Figure 6.1a,b show the time evolution of amplitudes of the resonant wave A_1 and the initial wave A_2 when different number of modes are taken into account in (6.18) ($T = 2\pi/\omega$ is the period of the initial wave). Results with n=4,8,16 and 20 are shown. For the initial time of t/T <20 all predictions agree well: A_1 initially increases at the expense of a decrease in A_2 until reaching a maximum beyond which the direction of energy flow reverses. This modulation is in agreement with classical (Bragg or wave-wave) triad resonance (e.g. Mei, 1985; Liu and Yue, 1998; Alam, 2012b). However, while n=4 model predicts a full recurrence over a longer time, taking into account a higher number of modes shows a continuous energy drainage from both A_2 and A_1. Specifically note the converged results for n=16, 20 which are hardly distinguishable graphically for the time-span plotted ($0< t/T <100$).

We show in fig 6.1c a more holistic view of how energy is exchanged between different modes. Presented results are calculated for $n = 20$ for which all curves are converged. As discussed

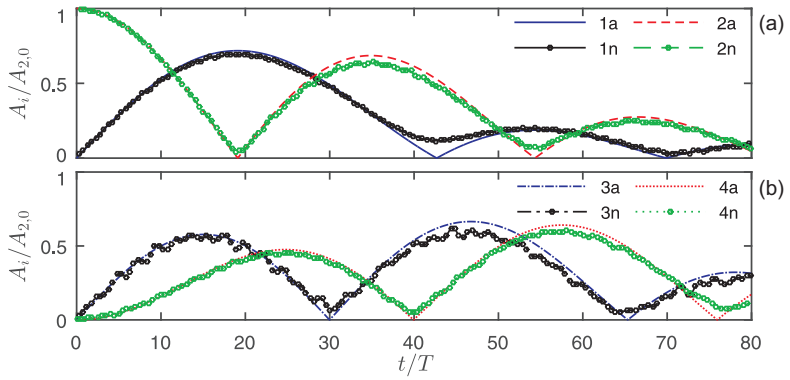


Figure 6.1: Time evolution of the first four mode internal waves engaged in a Bragg resonance as calculated by our multiple-scale analysis (6.18) (legend 'a'), and direct simulation of full Euler's equation via MITgcm (legend 'n'). Both analytical and numerical results show the flow of energy from initial wave A_2 to eventually shorter waves. Chosen parameters are $ah = 0.05$, $\omega/\sqrt{ga} = 0.2$, $f_b/h = 0.02$, $k_b h = 0.64$, $A_{20} = 0.0015$m, $A_{i,0} = 0$ for $i \neq 2$, and n=20.

before, initially A_2 loses energy to its immediate neighboring waves A_1,A_3. While A_1 has no alternative but to send the energy back to A_2, once A_3 has enough energy a new avenue opens up for energy to go to A_4 that will subsequently send energy to A_5 (not shown) and so on. The amplitude of initial wave A_2 decreases over time. The amplitude of other waves has a rise period during which they gain energy, and a fall period during which they lose energy to shorter waves. This trend is best seen in the behavior of A_8 in fig 6.1c: for t/T <10 this wave practically does not exist ($A_8 \sim 0$); for 10< t/T <50 it gains energy and after t/T ∼50 it loses energy. Similar trends are seen for all other waves, e.g. c.f. A_{12} in fig 6.1c. We would like to stress that, as is seen in this example, if initial internal wave is of a mode greater than one (e.g. in the above example is mode 2) then energy initially flows to longer internal waves (e.g. in the above example to mode 1), but in all cases eventaully energy goes to high wavenumber waves.

We finally compare our predictions to the direct simulation of full Euler's equation under Boussinesq approximation. To do so, we employ MITgcm (Marshall et al., 1997), an open source non-hydrostatic hydrodynamic solver (finite volume), which is widely used for modeling waves in stratified fluids (e.g. Engqvist and Hogg, 2004; Klymak et al., 2010; Lim et al., 2010; Churaev et al., 2015; Alford et al., 2015b). In the numerical setup, we use periodic left and right boundaries, a free surface and a free-slip bottom. Viscosity is turned off in the simulation. Figure 6.1 shows the evolution of the first four modes, as predicted by our theoretical analysis and as computed by the direct simulation of Euler's equation. Direct simulation results match very well with the analytical results, endorsing the discussed trend of energy flowing to shorter waves.

It should be noted that the presented mulitple scale analysis takes into account only Bragg

interactions, while the direct simulation is fully nonlinear and takes into account all leading and higher order wave-wave and wave-bottom interactions. Also, as mentioned before, for a free-surface top boundary condition Bragg resonance is satisfied to the leading order and not perfectly (if $ah \ll 1$ the error barely touches 1%). These factors contribute to the small yet visible discrepancy in fig 6.1.

Dispersion relation curves for a fluid with a general density profile, for which $N = N(z)$, usually follow a similar qualitative pattern as in fig 6.1. While a component of the seabed may not necessarily result in a Bragg resonance between adjacent wave modes (as we saw here for $N =$ constant), still a cascade of resonance and near resonance interactions between different modes is expected to obtain, and to carry energy to higher wavenumber waves. For instance, for an exponential density profile, the distance between wave modes are nearly equal and very similar to the case studied here. Nevertheless, for a general $N = N(z)$, a closed-form analytical solution to the resonance equation does not exist and we need to resort to numerical solutions. We would like to note that the qualitative behavior of internal waves reported here is not sensitive to small bottom slope and small wavenumber detunings. Both effects can be easily worked out through the extension of the theory presented here (c.f. e.g. Mei, 1985).

6.4 Conclusion

Here we showed that in a continuously stratified fluid of linear density profile, Bragg resonance can transfer the energy of an internal wave to an infinite number of higher wavenumber internal waves. We presented analytical expressions for the evolution of the wave amplitudes under such resonance interaction, and obtained a very good agreement with the direct simulation of full Euler's equation.

Bragg resonance of internal waves in a continuously stratified fluid may significantly affect the energy balance of internal wave spectrum, offer an alternative mechanism for the generation of short internal waves, and help better understand observations of strong internal wave activity and enhanced mixing over rough topographies. Targeted field observations and high-fidelity direct simulations (that include viscous effect, turbulence and breaking) needs to be performed to evaluate the extent of importance of Bragg resonance in the evolution and fate of oceanic internal waves, based on which, potential incorporation in large-scale models may be sought.

Bibliography

B. Bourget, T. Dauxois, S. Joubaud, and P. Odier. Experimental study of parametric subharmonic instability for internal plane waves. Journal of Fluid Mechanics, 723:1–20, 2013.

C. Garrett. Internal tides and ocean mixing. Science, 301(5641):1858–9, 2003a.

P. W. Boyd. Biogeochemistry: Iron findings. Nature, 446(7139):989–991, 2007.

G. P. Harris. Phytoplankton ecology: Structure, function and fluctuation. Chapman and Hall, 1986. ISBN 9780412306907.

W. H. Munk. Abyssal recipes. Deep Sea Research and Oceanographic Abstracts, 13:707–730, 1966.

W. Munk and C. Wunsch. Abyssal recipes II: energetics of tidal and wind mixing. Deep Sea Research Part I: Oceanographic Research Papers, 45(12):1977–2010, dec 1998.

M. H. Alford, T. Peacock, J. A. MacKinnon, J. D. Nash, M. C. Buijsman, L. R. Centuroni, S.-Y. Chao, M.-H. Chang, D. M. Farmer, O. B. Fringer, et al. The formation and fate of internal waves in the south china sea. Nature, 521(7550):65–69, 2015a.

O. Bühler and M. Holmes-Cerfon. Decay of an internal tide due to random topography in the ocean. Journal of Fluid Mechanics, 678:271–293, 2011.

R. E. Davis and A. Acrivos. The stability of oscillatory internal waves. Journal of Fluid Mechanics, 30(4):723–736, 1967.

K. Hasselmann. A criterion for nonlinear wave stability. Journal of Fluid Mechanics, 30(04): 737, 1967.

J. L. Hammack and D. M. Henderson. Resonant interactions among surface water waves. Annual Review of Fluid Mechanics, 25:55–97, 1993.

A. D. D. Craik. Wave interactions and fluid flows. Cambridge University Press, 1986. ISBN 9780511569548.

O. M. Phillips. On the dynamics of unsteady gravity waves of finite amplitude. Journal of Fluid Mechanics, 9:193–217, 1960.

M. S. Longuet-Higgins and N. D. Smith. An experiment on third-order wave interactions. Journal of Fluid Mechanics, 25:417–435, 1966.

F. K. Ball. Energy transfer between external and internal gravity waves. Journal of Fluid Mechanics, 19(03):465–478, 1964.

S. A. Thorpe. On wave interactions in a stratified fluid. Journal of Fluid Mechanics, 24: 737–751, 1966.

K. M. Case and S. C. Chiu. Three wave resonant interactions of gravity capillary waves. Physics of Fluids, 20(5):742–745, 1977.

A. C. Newell. Rossby wave packet interactions. Journal of Fluid Mechanics, 35:255–271, 1969.

P. N. Lombard and J. J. Riley. Instability and breakdown of internal gravity waves. I. Linear stability analysis. Physics of Fluids, 8:3271–3287, 1996.

C. R. Koudella and C. Staquet. Instability mechanisms of a two-dimensional progressive internal gravity wave. Journal of Fluid Mechanics, 548:165, 2006.

H. H. Karimi and T. R. Akylas. Parametric subharmonic instability of internal waves: locally confined beams versus monochromatic wavetrains. Journal of Fluid Mechanics, 757:381–402, 2014.

A. G. Davies. The reflection of wave energy by undulations on the seabed. Dynamics of Atmospheres and Oceans, 6:207–232, 1982.

A. G. Davies and A. D. Heathershaw. Surface-wave propagation over sinusoidally varying topography. Journal of Fluid Mechanics, 144:419–443, April 1984.

C. C. Mei. Resonant reflection of surface water waves by periodic sandbars. J. Fluid Mech., 152:315–335, April 1985.

R. A. Dalrymple and J. T. Kirby. Water waves over ripples. Journal of Waterway, Port, Coastal, and Ocean Engineering, 112(2):309–319, 1986.

R. B. Elandt, M. Shakeri, and M.-R. Alam. Surface gravity-wave lensing. Physical Review E, 89:1–6, 2014.

T. Dauxois, A. Didier, and E. Falcon. Observation of near-critical reflection of internal waves in a stably stratified fluid. Physics of Fluids, 16:1396, 2004.

J. R. Ledwell, E. T. Montgomery, K. L. Polzin, L. C. St. Laurent, R. W. Schmitt, and J. M. Toole. Evidence for enhanced mixing over rough topography in the abyssal ocean. Nature, 403:179–182, 2000.

J. D. Nash, E. Kunze, J. M. Toole, and R. W. Schmitt. Internal Tide Reflection and Turbulent Mixing on the Continental Slope. Journal of Physical Oceanography, 34:1117–1134, 2004.

Y. Liang, Ahmad Zareei, and M. R. Alam. Inherently Unstable Internal Gravity Waves due to Resonant Harmonic Generation. Journal of Fluid Mechanics, 811:400–420, 2017.

K. G. Lamb. Internal Wave Breaking and Dissipation Mechanisms on the Continental Slope/Shelf. Annual Review of Fluid Mechanics, 46:231–54, 2014.

S. Sarkar and A. Scotti. From topographic internal gravity waves to turbulence. Annual Review of Fluid Mechanics, 49(1):195–220, 2017.

L. Zhang and H. L. Swinney. Virtual seafloor reduces internal wave generation by tidal flow. Physical Review Letters, 112:104502, 2014.

H. Scolan, E. Ermanyuk, and T. Dauxois. Nonlinear fate of internal wave attractors. Physical Review Letters, 110:234501, 2013.

Thierry Dauxois, Sylvain Joubaud, Philippe Odier, and Antoine Venaille. Instabilities of Internal Gravity Wave Beams. Annual Review of Fluid Mechanics, 50:1–28, 2018.

O. M. Phillips. Wave interactions - the evolution of an idea. Journal of Fluid Mechanics, 106:215–227, 1981.

C.-H. Jiang and P. S. Marcus. Selection rules for the nonlinear interaction of internal gravity waves. Physical Review Letters, 102:124502, 2009.

M. H. Alford. Observations of parametric subharmonic instability of the diurnal internal tide in the South China Sea. Geophysical Research Letters, 35(15):2–6, 2008.

B. S. Chinn, J. B. Girton, and M. H. Alford. Observations of internal waves and parametric subharmonic instability in the Philippines archipelago. Journal of Geophysical Research: Oceans, 117(5):1–12, 2012.

S. Martin, W. Simmons, and C. Wunsch. The excitation of resonant triads by single internal waves. Journal Fluid Mechanics, 53:17–44, 1972.

A. D. McEwan. Degeneration of resonantly-excited standing internal gravity waves. Journal of Fluid Mechanics, 50(03):431–448, 1971.

D. Benielli and J. Sommeria. Excitation and breaking of internal gravity waves by parametric instability. Journal of Fluid Mechanics, 374:117–144, 1998.

C. Staquet and J. Sommeria. Internal gravity waves : from instabilities to turbulence. Annual Review of Fluid Mechanics, 34:559–593, 2002.

D. Olbers, J. Willebrand, and C. Eden. Ocean Dynamics. Springer-Verlag Berlin Heidelberg, 2012. ISBN 978-3-642-23449-1.

W. G. Zhang and T. F. Duda. Intrinsic Nonlinearity and Spectral Structure of Internal Tides at an Idealized Mid-Atlantic Bight Shelf Break. Journal of Physical Oceanography, 43:2641–2660, 2013.

B. Gayen and S. Sarkar. Degradation of an internal wave beam by parametric subharmonic instability in an upper ocean pycnocline. Journal of Geophysical Research: Oceans, 118 (9):4689–4698, 2013.

S. Joubaud, J. Munroe, P. Odier, and T. Dauxois. Experimental parametric subharmonic instability in stratified fluids. Physics of Fluids, 24(24):41703–23116, 2012.

A. S. Korobov and K. G. Lamb. Interharmonics in internal gravity waves generated by tide-topography interaction. Journal of Fluid Mechanics, 611:61–95, 2008.

R. L. Zalkan. High frequency internal waves in the Pacific Ocean. Deep-Sea Research, 17: 91–108, 1970.

L. Boegman, J. Imberger, G. N. Ivey, and J. P. Antenucci. High-frequency internal waves in large stratified lakes. Limnology and Oceanography, 48(2):895–919, 2003.

D. L. Rudnick, T. M. S. Johnston, and J. T. Sherman. High-frequency internal waves near the Luzon Strait observed by underwater gliders. Journal of Geophysical Research: Oceans, 118(2):774–784, 2013.

A. D. Mcewan, D. W. Mander, and R. K. Smith. Forced resonant second-order interaction between damped internal waves. Journal of Fluid Mechanics, 55(04):589, 1972.

J. Marshall, A. Adcroft, C. Hill, L. Perelman, and C. Heisey. A finite-volume, incompressible Navier Stokes model for studies of the ocean on parallel computers. Journal of Geophysical Research, 102:5753–5766, 1997.

A. Engqvist and A.M. Hogg. Unidirectional stratified flow through a non-rectangular channel. Journal Fluid Mechanics, 509:83–92, 2004.

J. M. Klymak, S. M. Legg, and R. Pinkel. High-mode stationary waves in stratified flow over large obstacles. Journal of Fluid Mechanics, 644:321–336, 2010.

K. Lim, G. N. Ivey, and N. L. Jones. Experiments on the generation of internal waves over continental shelf topography. Journal of Fluid Mechanics, 663:385–400, 2010.

E. N. Churaev, S. V. Semin, and Y. A. Stepanyants. Transformation of internal waves passing over a bottom step. Journal of Fluid Mechanics, 768:1–11, 2015.

M. H. Alford, T. Peacock, J. A. MacKinnon, J. D. Nash, M. C. Buijsman, L. R. Centuroni, S.-Y. Chao, M.-H. Chang, D. M. Farmer, O. B. Fringer, K.-H. Fu, P. C. Gallacher, H. C. Graber, K. R. Helfrich, S. M. Jachec, C. R. Jackson, J. M. Klymak, D. S. Ko, S. Jan, T. M. S. Johnston, S. Legg, I.-H. Lee, R.-C. Lien, M. J. Mercier, J. N. Moum, R. Musgrave, J.-H. Park, A. I. Pickering, R. Pinkel, L. Rainville, S. R. Ramp, D. L. Rudnick, S. Sarkar, A. Scotti, H. L. Simmons, L. C. St Laurent, S. K. Venayagamoorthy, Y.-H. Wang, J. Wang, Y. J. Yang, T. Paluszkiewicz, and T.-Y. Tang. The formation and fate of internal waves in the South China Sea. Nature, 521(7550):65–69, 2015b.

J. A. MacKinnon, M. H. Alford, O. Sun, R. Pinkel, Z. Zhao, and J. Klymak. Parametric subharmonic instability of the internal tide at 29n. Journal of Physical Oceanography, 43 (1):17–28, 2013.

O. Richet, C. Muller, and J.-M. Chomaz. Impact of a Mean Current on the Internal Tide Energy Dissipation at the Critical Latitude. Journal of Physical Oceanography, 47(6): 1457–1472, 2017.

X. H. Xie, X. D. Shang, H. Van Haren, G. Y. Chen, and Y. Z. Zhang. Observations of parametric subharmonic instability-induced near-inertial waves equatorward of the critical diurnal latitude. Geophysical Research Letters, 38(5):1–7, 2011.

O. M. Sun and R. Pinkel. Subharmonic energy transfer from the semidiurnal internal tide to near-diurnal motions over Kaena Ridge, Hawaii. Journal of Physical Oceanography, 43 (4):766–789, 2012.

V. K. Chalamalla and S. Sarkar. PSI in the case of internal wave beam reflection at a uniform slope. Journal of Fluid Mechanics, 789:347–367, 2016.

M.-R. Alam, Y. Liu, and D. K. P. Yue. Bragg resonance of waves in a two-layer fluid propagating over bottom ripples. part ii. numerical simulation. Journal of Fluid Mechanics, 624:225–253, 2009a.

C. H. McComas and F. P. Bretherton. Resonant interaction of oceanic internal waves. Journal of Geophysical Research, 82(9):1397–1412, 1977.

C. Garrett. Oceanography: Mixing with latitude. Nature, 422(6931):477–477, 2003b.

F. Karimpour, A. Zareei, and M.-R. Alam. Sensitivity of internal wave energy distribution over seabed corrugations to adjacent seabed features. Journal of Fluid Mechanics, pages 74–96, 2017.

L.-A. Couston, Y. Liang, and M.-R. Alam. Oblique chain resonance of internal waves by three-dimensional seabed corrugations. Journal of Fluid Mechanics, 833:538–562, 2017.

A. Tabaei, T. R. Akylas, and K. G. Lamb. Nonlinear effects in reflecting and colliding internal wave beams. Journal of Fluid Mechanics, 526:217–243, 2005.

M.-R. Alam, Y. Liu, and D. K. P. Yue. Bragg resonance of waves in a two-layer fluid propagating over bottom ripples. Part I. Perturbation analysis. Journal of Fluid Mechanics, 624:191–224, 2009b.

M.-R. Alam, Y. Liu, and D. K. P. Yue. Oblique sub-and super-harmonic bragg resonance of surface waves by bottom ripples. Journal of Fluid Mechanics, 643:437–447, 2010.

M.-R. Alam. A new triad resonance between co-propagating surface and interfacial waves. Journal of Fluid Mechanics, 691:267–278, 2012a.

M.-R. Alam and C. C. Mei. Attenuation of long interfacial waves over a randomly rough seabed. Journal of Fluid Mechanics, 587:73–96, 2007.

O. B. Fringer, M. Gerritsen, and R. L. Street. An unstructured-grid, finite-volume, nonhydrostatic, parallel coastal ocean simulator. Ocean Modelling, 14(3-4):139–173, 2006.

Z. Zhang, O. B. Fringer, and S. R. Ramp. Three-dimensional , nonhydrostatic numerical simulation of nonlinear internal wave generation and propagation in the South China Sea. Journal of Geophysical Research, 116(C05022):1–26, 2011.

D. Kang and O. Fringer. On the Calculation of Available Potential Energy in Internal Wave Fields. Journal of Physical Oceanography, 40(11):2539–2545, 2010.

B. Wang, S. N. Giddings, O. B. Fringer, E. S. Gross, D. A. Fong, and S. G. Monismith. Modeling and understanding turbulent mixing in a macrotidal salt wedge estuary. Journal of Geophysical Research, 116(C02036):1–23, 2011.

D. Kang and O. Fringer. Energetics of Barotropic and Baroclinic Tides in the Monterey Bay Area. Journal of Physical Oceanography, 42(2):272–290, 2012.

R. K. Walter, C. B. Woodson, R. S. Arthur, O. B. Fringer, and S. G. Monismith. Nearshore internal bores and turbulent mixing in southern Monterey Bay. Journal of Geophysical Research, 117(C07017):1–13, 2012.

T. Gerkema, C. Staquet, and P. Bouruet-Aubertot. Decay of semi-diurnal internal-tide beams due to subharmonic resonance. Geophysical Research Letters, 33(8):L08604, 2006.

J. A. MacKinnon and K. B. Winters. Subtropical catastrophe: Significant loss of low-mode tidal energy at 28.9°. Geophysical Research Letters, 32(15):L15605, 2005.

P. Muller. Nonlinear Interactions Among Internal Gravity Waves. Reviews of Geophysics, 24(3):493–536, 1986.

B. R. Sutherland. Excitation of superharmonics by internal modes in non-uniformly stratified fluid. Journal of Fluid Mechanics, 793:335–352, 2016.

P. A. Franken, A. E. Hill, C. W. Peters, and G. Weinreich. Generation of optical harmonics. Physical Review Letters, 7:118–119, 1961.

F. P. Bretherton. Resonant interactions between waves. The case of discrete oscillations. 20 (3):457–479, 2018.

K. Lambeck. The Earth's Variable Rotation: Geophysical Causes and Consequences. Cambridge University Press, Cambridge, 1980.

G. D. Egbert and R. D. Ray. Estimates of M2 tidal energy dissipation from TOPEX/Poseidon altimeter data. Journal of Geophyical Research, 106502(15):475–22, 2001.

G. D. Egbert and R. D. Ray. Significant Dissipation of Tidal Energy in the Deep Ocean Inferred from Satellite Altimeter Data. Nature, 405(1993):775–778, 2000.

M. H. Alford. Redistribution of energy available for ocean mixing by long-range propagation of internal waves. Nature, 423(6936):159–162, 2003.

C. Garrett and E. Kunze. Internal Tide Generation in the Deep Ocean. Annual Review of Fluid Mechanics, 39(1):57–87, 2007.

K. Kundu. Fluid Mechanics. Academic Press, 1990. ISBN 978-0-12-382100-3.

A. C. N. Garabato, K. L. Polzin, B. A. King, K. J. Heywood, and M. Visbeck. Widespread intense turbulent mixing in the southern ocean. Science, 303:210–213, 2004.

C. Kranenburg, J. D. Pietrzak, and G. Abraham. Trapped internal waves over undular topography. Journal of Fluid Mechanics, 226:205–217, 1991.

Y. Liu and D. K.P. Yue. On generalized Bragg scattering of surface waves by bottom ripples. Journal of Fluid Mechanics, 356:297–326, 1998.

D. J. Olbers. Nonlinear energy transfer and the energy balance of the internal wave field in the deep ocean. Journal of Fluid Mechanics, 74:375–399, 1976.

C. Garrett and W. Munk. Oceanic mixing by breaking internal waves. Deep Sea Research and Oceanographic Abstracts, 19(12):823–832, 1972a.

C. Garrett and W. Munk. Space-Time scales of internal waves. Geophysical Fluid Dynamics, 3:225–264, 1972b.

M.-R. Alam. A new triad resonance between co-propagating surface and interfacial waves. Journal of Fluid Mechanics, 691:267–278, 2012b.